ESCOLA SUPERIOR
POLITÉCNICO SETÚBAL

ANA LUÍSA DA SILVA MENDONÇA FERRAMACHO

QUALITY STUDY OF PARTS FOR AERONAUTIC SECTOR PRODUCED BY L-PBF: FROM FEEDSTOCK TO FINAL PRODUCT

Internship Report for the Master's Degree in Production Engineering

SUPERVISOR

PhD. Célio Gabriel Figueiredo Pina

CO-SUPERVISOR

MSc Paulo Jorge Bilro Machado

December 2025

ANA LUÍSA DA SILVA MENDONÇA FERRAMACHO

QUALITY STUDY OF PARTS FOR AERONAUTIC SECTOR PRODUCED BY L-PBF: FROM FEEDSTOCK TO FINAL PRODUCT

JURY

Chairperson: PhD. Pedro Filipe do Carmo Cunha, IPS
Supervisor: PhD. Célio Gabriel Figueiredo Pina, IPS
Examiner: PhD. Maria João Pedroso Carmezim, IPS

December 2025

“Live as if you were to die tomorrow. Learn as if you were to live forever.”

Mahatma Gandhi

Acknowledgements

First and foremost, I would like to express my sincere gratitude to my supervisor, Professor Célio Pina, for his availability, for sharing knowledge and ideas, for the stimulating discussions, and for the genuine interest he demonstrated throughout this work. I am deeply thankful for his positive attitude, his encouragement during moments of discouragement, and his unwavering dedication.

I would also like to express my gratitude to Professor Paulo Machado for his valuable assistance in facilitating the thermal treatments, providing internal documents, and offering guidance regarding the qualification process.

Furthermore, I am deeply appreciative of Innovative Manufacturing team at LAUAK for their welcome and willingness to exchange ideas, especially to Yves Marcel and André Abreu. I am also grateful to António Garcês for his willingness to explain how the printing machine works, his work in printing the parts and removing the powder for sampling, as well as the teachings and healthy discussions that took place throughout this work and the good working environment provided.

I am also indebted to the entire team at the Materials and Biotechnology laboratories of the Mechanical Engineering Department at *Escola Superior de Tecnologia de Setúbal* (Laboratories E122 and E224) who kindly assisted with the tensile tests, using the disc saw and other equipment, and also provided suggestions and camaraderie. To Professor José Simões and his team, for machining the tensile tests specimens. I would also like to thank the institution for providing the equipment used.

Two special thanks: one to the ISQ team, especially Professor Rodolfo Batalha for analysing the powders, other to Alex Garcia from Renishaw for his valuable explanations on how the machine works and for helping to understand some phenomena that occur during the additive manufacturing process.

I must also thank the Portuguese State and the European Union for funding the AeroNext ProAero 3D project, of which this work is part.

Finally, I would like to express my gratitude to my family for their unwavering support and understanding throughout this process, and especially to my husband, Luís Valério Ferramacho, for his patience during my absence.

Abstract

This work aimed to assess the quality of parts produced in AlSi10Mg by additive manufacturing using Laser Powder Bed Fusion, at LAUAK Grândola, under production conditions. The quality of the feedstock was evaluated, including particle size distribution, chemical composition, morphology, and powder flowability. Additionally, relative density, tensile strength, hardness along the specimen, and microstructure were studied for specimens in the as-built condition and after heat treatment. It was concluded that substrate temperature is a critical parameter for the final quality of the produced parts, as well as the layer time.

Keywords: Additive Manufacturing, L-PBF, Parts Quality, Powder Quality, Mechanical Properties, AlSi10Mg.

Resumo

Com este trabalho pretendeu-se averiguar acerca da qualidade de peças produzidas em AlSi10Mg por fabrico aditivo de fusão seletiva de pó por laser, na LAUAK Grândola, em contexto de produção. Avaliou-se a qualidade da matéria-prima, nomeadamente: a distribuição do tamanho de partícula, a composição química, a morfologia e a escoabilidade do pó. Estudou-se, também, a densidade relativa, resistência à tração, dureza ao longo do provete e microestrutura dos provetes tal como fabricados e após tratamento térmico. Concluiu-se que a temperatura do substrato é um parâmetro bastante importante na qualidade final das peças produzidas, assim como o tempo por camada.

Palavras-chave: Fabrico Aditivo, L-PBF, Qualidade das Peças, Qualidade do Pó, Propriedades Mecânicas, AlSi10Mg.

Contents

Acknowledgements i
Abstract ii
Resumo iii
Contents iv
List of Figures vii
List of Tabels xi
List of Abbreviations xii
List of Symbols xiv
Chapter 1 1
Introduction 1
1.1. Goal 3
1.2. Additive Manufacturing Regulatory Framework 3
Chapter 2 5
Literature review 5
2.1. Laser Powder Bed Fusion 6
2.2. Powder Quality 12
2.2.1. Particle Size Distribution 12
2.2.2. Chemical Composition 13
2.2.3. Powder Morphology 13
2.2.4. Flowability 14
2.3. AlSi10Mg 15
2.4. Compilation of Standards for Process Qualification 18
2.4.1. Requirements for Purchased AM Parts – ISO/ASTM 52901:2016 19
2.4.2. Requirements for feedstock materials – Methods to characterize metallic powders – ISO/ASTM 52907:2019 19
2.4.3. Additive Manufacturing – Process Characteristics and Performance: Practice for Metal Powder Bed Fusion Process to Meet Critical Applications – ISO/ASTM 52904:2019 19
2.4.4. Additive Manufacturing - Finished part properties – Specification for AlSi10Mg with Powder Bed Fusion – Laser Beam – ASTM F3318-18 20

Chapter 3 22
Methods 22
3.1. RenAM 500Q Ultra 23
3.2. Powder Flow 26
3.3. Specimens' Production and Powder Sampling 27
3.4. Powder Characterisation 31
3.4.1. Particle Size Distribution *31*
3.4.2. Chemical Composition *31*
3.4.3. Morphology *31*
3.4.4. Flowability *32*
3.5. Specimens Characterisation 32
3.5.1. Relative Density *32*
3.5.2. Tensile Test *33*
3.5.4. Hardness *34*
3.5.5. Microstructure *36*
Chapter 4 37
Results 37
4.1. Powder Characterisation 38
4.1.1. Particle Size Distribution *38*
4.1.2. Chemical Composition *43*
4.1.3. Morphology *47*
4.1.4. Flowability *49*
4.2. Specimens Characterisation 50
4.2.1. Relative Density *50*
4.2.2. Tensile Test *51*
4.2.3. Hardness *53*
4.2.4. Microstructure *56*
Chapter 5 61
Discussion 61
Chapter 6 74
Conclusions and Future Developments 74
References 78
Appendices A.1
Appendix 1 – Purchase Order A.1

Appendix 2 – Powder Sampling from Hopper A.4
Appendix 3 – Methods used for particle size analysis..... A.5

List of Figures

Figure 2.1 – Timeline of the additive manufacturing process.. 6
Figure 2.2 – Illustration of the powder bed process with the powder supply on the left-hand side and the powder bed on the right-hand side. 7
Figure 2.3 – Schematic representation of the interaction between the laser beam source and the powder bed during the L-PBF process highlighting the overlap area between two adjacent laser scan tracks where the principal dimensions are labelled 8
Figure 2.4 – Schematic representation of L-PBF process by-products formation and its influence of clustered particles..... 8
Figure 2.5 – Denudation and spatter particles in L-PBF process a) Scheme, and b) Top view picture 9
Figure 2.6 – Critical process parameters for additive manufacturing. 10
Figure 2.7 – Laser strategy. a) Meander, b) Striped, c) Chessboard, d) Remelting – Opposite direction, and e) Remelting – Same direction 10
Figure 2.8 – Porosity, Crack and Surface defects observed in the L-PBF processed parts of aluminium alloys 12
Figure 2.9 – High packing density is associated with the production of high quality, minimally flawed components and can be achieved using a powder with a relatively broad particle size distribution 12
Figure 2.10 – Correspondence between area from a non-spherical particle and a spherical particle and x_{area} representation 13
Figure 2.11 – Powder morphology 14
Figure 2.12 – The best scenario for: a) the highest powder packability, and b) powder flowability..... 14
Figure 2.13 – Al-Si phase diagram 15
Figure 2.14 – Optical Microscopy micrographs of the as-built AlSi10Mg

samples along the xy (a and b) and xz (c and d) planes. Panels (a and c) are related to the single laser machine set-up and (b and d) to the multi laser. The green arrow indicates the build direction 16
Figure 2.15 – Microstructure of the as-built AlSi10Mg alloy captured at a) transverse and b) longitudinal sections 16
Figure 2.16 – SEM micrographs tracking microstructure evolution in AlSi10Mg at different build temperatures. All the scale bars in the micrographs represent 5 µm 17
Figure 2.17 – Solidification map obtained by the G/R and G×R factor 18
Figure 3.1 – RenAM 500Q Ultra at LAUAK Grândola Additive Manufacturing workplace. 23
Figure 3.2 – Lasers firing as the recoater deposits a new layer of powder 23
Figure 3.3 – RenAM front view 24
Figure 3.4 – RenAM front view with powder fill and large SafeChange filter door open 25
Figure 3.5 – a) Four PRISM lasers with laser output and cooling connections, b) Lens protection window, c) Build chamber viewing window, and d) Gas circuit 26
Figure 3.6 – Flow of powder during AM process. 27
Figure 3.7 – a) and b) new powder (powder 1); c) hopper (powder 2); d) and e) chamber (powder 2); f) cyclone; g) cyclone flask (powder 3); h) powder recovery system (powder 4). 27
Figure 3.8 – Specimen technical draw. 29
Figure 3.9 – a) Analytical balance with the density determination kit, and b) side view confirming total immersion of the test piece without touching the bottom or sides of the container 33
Figure 3.10 – Specimen a) as-built, and b) machined. 34
Figure 3.11 – Specimen with the clip gauge for the tensile test. 34
Figure 3.12 – a) Specimen placed in a tailored PLA container filled with resin, and b) Specimen cut lengthwise 35
Figure 3.13 – Scheme of the specimen marked every 10 mm. 35
Figure 3.14 – a) Falcon 450 Hardness Tester, and b) Vickers Hardness

measurement. 36

Figure 4.1 – x_{area} distribution of particles size from powders 1 38

Figure 4.2 – Cumulative x_{area} distribution for powder 1 39

Figure 4.3 – Comparison in between powder 2 from consecutive builds, 45A, 45B, and 46. 40

Figure 4.4 – Comparison between powder 2 from builds 47, 48 and 51 .. 40

Figure 4.5 – Cumulative x_{area} distribution for powder 2. 41

Figure 4.6 – Comparison between powder 1, 3 and 4..... 42

Figure 4.7 – Cumulative particle percentage of x_{area} distribution for powder 1, 3 and 4. 42

Figure 4.8 – SEM Images 2000x magnification from powder 1 S1 Lot C. a) SE, b) BSE, c) Al, d) Si; e) Mg, f) Fe, g) Cu, h) Mn, i) Ti, j) Zn, k) Sn, l) Pb, m) O, n) N and o) C 44

Figure 4.9 – SEM Image 500x magnification from powder 1 S1 Lot C whit the selected regions for X-ray fluorescence analysis 44

Figure 4.10 – SEM images 200x magnification of AlSi10Mg powder 1: S1 Lot B, S1 Lot C, S2 Lot B, S3 Lot A, and S3 Lot B; powder 2: 45A, 45B, 46, 47,and 51, powder 3, and powder 4 48

Figure 4.11 – Flowability from powder 1 samples 49

Figure 4.12 – Flow rate from powder 2 samples in comparison to a reference sample, powder 1 from supplier 1 50

Figure 4.13 – Tensile curves for each sample of as-built 57, 58, and 80 builds..... 51

Figure 4.14 – UTS, and elongation results as-built (NHT) and after SR1 heat treatment for the studied specimens in comparison with ASTM 3318 values..... 52

Figure 4.15 – Yield strength, and elongation results as-built (NHT) and after SR1 heat treatment for studied specimens in comparison with ASTM 3318 values..... 53

Figure 4.16 – HV1 results from bottom to top specimen. The error bars represent the standard deviation of the measured values.... 54

Figure 4.17 – Comparison between the hardness of samples 35 and 41, as-built and with heat treatment (SR1). 55

Figure 4.18 – HV1 dispersion per build. 55
Figure 4.19 – Optical Microscopy images 50x magnification of top region from 45, 46, 47P, 48P, 51, and 57 specimens. 56
Figure 4.20 – Optical Microscopy images 50x magnification of bottom region from 45, 46, 47P, 48P, 51, and 57 specimens. 56
Figure 4.21 – Optical micrograph 50x magnification from a specimen etched with Keller's reagent for 30 seconds. 57
Figure 4.22 – SEM micrographs from sample 41 as-built: zone C a) 2000x, b) 10000x, c) 3000x, and d) 10000x; zone E e) 10000x and f) 20000x; zone H g) 10000x and h) 20000x. 58
Figure 4.23 – SEM micrographs from sample 41 heat-treated: zone C - a) 2000x, b) 10000x; zone E - c) 10000x and d) 20000x; zone H - e) 2000x and f) 10000x. 59
Figure 4.24 – a) Positioning of the analysed areas taking into account the hardness results. b) and c) SEM images from sample 58, 10000x magnification at positions C and H, respectively 60
Figure 5.1 – Hardness and Layer Time relations with Build Height..... 69
Figure 5.2 – HV1 vs Layer Time Correlation for builds with a height lower than the specimen..... 70
Figure 5.3 – HV1 vs Layer Time Correlation for build higher than specimen 70
Figure 5.4 – SEM micrographs from sample a) 58 as-built in zone H: low HV1; and b) 41 after SR1 heat-treatment..... 71

List of Tabels

Table 2.1 – Defects present into L-PBFed samples: Cause, remedy and effects. 11
Table 2.2 – Chemical composition of parts made by AlSi10Mg alloy. 20
Table 2.3 – Minimum Tensile Properties 21
Table 3.1 – Parameters of the studied builds 28
Table 3.2 – Samples from powder 1 29
Table 3.3 – Sample ID and Number of builds without adding new powder relationship 30
Table 4.1 – D10, D50, and D90 for the different powders 1 39
Table 4.2 – D10, D50, and D90 for the different powders 2 41
Table 4.3 – D10, D50, and D90 for the powders 1 (S1 Lot A), 3 and 4. ... 43
Table 4.4 – Chemical composition of powder 1 from different suppliers and ASTM F3318 recommended values for the final part.. 45
Table 4.5 – Chemical composition % (w/w) of powder 2 from samples 45A, 45B, 46, 47, 48, 51, and 57, and comparison with ASTM F3318 recommended values for the final part 46
Table 4.6 – Chemical composition % (w/w) of powder 1, 3 and 4, and comparison with ASTM F3318-18 values for the final part.. 47
Table 4.7 – Specimens Relative Density Values (%). 51
Table 5.1 – Parameters and Properties for each studied build 64
Table 5 2 – Build Ranking by Relative Density. 65
Table 5.3 – Build Ranking by UTS (NHT). 66
Table 5.4 – Build Ranking by HV1 mean values. 67
Table 5.5 – Printed Area per Layer and Layer Time for build 51. 68
Table 5.6 – Comparison in between parameters for crankcase builds. 72
Table 5.7 – Comparison in between ranking properties of relative density, UTS, and HV1 for eligible builds at faster production conditions, regarding set up temperature (set up T). 73

List of Abbreviations

3D	Three-dimensional
AM	Additive Manufacturing
ASTM	American Society for Testing and Materials
BP	Build Platform
BSE	Back-Scattering Electrons
CAD	Computer Aided Design
CAM	Computer Aided Manufacturing
CNC	Computer Numerical Control
ED	Energy Density
EDS	Energy-Dispersive Spectroscopy
HAZ	Heat-Affected Zone
HT	Heat Treatment
IPS	*Instituto Politécnico de Setúbal* - Setúbal Polytechnic Institute
IQR	Iinterquartile Range
ISO	International Organization for Standardization
ISQ	*Instituto de Soldadura e Qualidade* - Welding and Quality Institute
L-PBF	Laser Powder Bed Fusion
MP	Molten Pool
MSFC-STD	Marshall Space Flight Center - STANDARD
Nadcap	National Aerospace and Defense Contractors Accreditation Program

NASA	National Aeronautics and Space Administration
P	Power
PLA	Polylactic Acid
PRS	Powder Recovery System
PSD	Particle Size Distribution
R&D	Research and Development
RP	Rapid Prototyping
SAE	Society of Automotive Engineers
SE	Secondary Electrons
SEM	Scanning Electron Microscope
SLM	Selective Laser Melting
SR1	Stress Relief 1
UTS	Ultimate Tensile Strength
XRF	X-ray Fluorescence
WANP	Without the Addition of New Powder
YAG	Yttrium Aluminium Garnet

List of Symbols

ρ density of weighed sample

ρ_F density of test liquid

m_1 mass of the sample weighed in air (kg)

m_2 mass of the sample reduced by the mass of displacement liquid (weighing the sample in the liquid) (kg),

Chapter 1

Introduction

This chapter introduces the research context and objectives, focusing on the quality assessment of AlSi10Mg components produced by Laser Powder Bed Fusion (L-PBF), for the highly regulated aerospace industry.

This is an internship report for obtaining a Master's degree in Production Engineering. The six-month internship was carried out at LAUAK's facilities in Grândola, where a metal powder additive manufacturing system is installed. The machine, a RenAM 500Q Ultra by Renishaw, was already operating under the parameters provided by the supplier. The internship took place in a production environment, meaning that the machine continued its regular operations throughout the study; consequently, the research activities had to adapt to the production cadence, minimizing any interference.

Founded in 1975 under the name ESKULANAK by its current co-manager, Jean-Marc Charritton, the LAUAK Group supplied boilers parts to Dassault Aviation. Today, the LAUAK Group is one of the leading subcontractors for the manufacture of primary parts, sub-assemblies and assemblies for the aerospace industry. Originally based in Hasparren, the LAUAK Group has grown over the years through various acquisitions and the creation of new factories. Today, the LAUAK Group has ten international locations in France, Portugal, Canada, Mexico and India.

Participation in the Pro Aero 3D program, part of the AeroNext agenda under the Portuguese Recovery and Resilience Plan and funded by the European Union, enabled LAUAK Grândola to acquire a metal additive manufacturing printer. This program aims to strengthen national capabilities in the application of additive manufacturing technology for the production of certifiable components for the aerospace industry, which constitutes the core business of the LAUAK Group. Since the installation of the printer in December 2024, efforts have been directed toward the certification of personnel, equipment, and processes. Personnel certification was completed in December 2024 through appropriate team training. Machine certification occurred during the course of this study, in June 2025, while process certification is still ongoing. Renishaw, the machine supplier, has provided guidance throughout the entire certification process.

The aviation industry is a booming sector because it is leveraged by increasing passenger traffic. Passenger traffic projections show that the aviation industry will continuously expand. Naturally, this expansion will attract many companies into the aviation industry and therefore attraction will conclude a fiercer competition environment in the aviation industry. As a result, the companies in the aviation industry will look for implementation of novel technologies since they will not want to fall behind their competitors. On the other hand, the aviation authorities always keep their decision and regulation maker position while the companies are the followers. It can be put forward that the most difficult side of the implementation of novel technologies into aviation industry is to get along with the strict rules and regulations which are put by international and national aviation authorities. Due to these requirements, the aviation has been forced to be a pioneer for implementation of novel manufacturing techniques such as Computer Aided Design (CAD), Computer Aided Manufacturing (CAM) and newly-developed materials such as carbon fibre composites. These technologies and materials were firstly adopted by the aviation industry. Many processes and materials were used by other sectors such as automotive, or ship construction, for example, after the aviation industry used those as regular ones (Saracyakupoglu, 2019).

Additive Manufacturing (AM) appears perfectly suited to the aviation industry, allowing lighter parts to be produced with lower cost in less operational time with the same mechanical features as the legacy manufacturing techniques. AM is a disruptive technical innovation whose history goes back nearly three decades. It is rapidly entering the aviation manufacturing sector. On the other hand, conventional *chip removal techniques* have been used in the aerospace industry almost a century and the manufacturing genome of aerospace is still under the domination of legacy manufacturing technologies. The traditional machining processes such as milling and turning are still used in the aerospace industry because voluminous metal parts are designed for Computer Numerical Control (CNC) machining operations. The aerospace materials are manufactured with highly engineered techniques hence these materials are generally not cheap. So, the wastage and scrap is very important. The lowest wastage is the best. But the traditional CNC machining processes are subtractive techniques, and the material wastage could be as high as 98%. Since the aerospace materials are expensive, the companies in the aircraft industry are under constant pressure to reduce wastage and develop manufacturing techniques for producing parts in near net shape (Saracyakupoglu, 2019).

1.1. Goal

One of the objectives of this work is to compile international standards that enable the qualification of the manufacturing process of AlSi10Mg alloy components produced by Laser Powder Bed Fusion (L-PBF) for aeronautical applications.

First, it is essential to assess the quality of the powders employed during additive manufacturing, including evaluating the feasibility of powder recycling to minimize costs and material waste while preserving manufacturing integrity.

Another critical aspect is the evaluation of the quality of the produced parts. The goal is to determine the optimal process parameters that ensure the components meet the client's required specifications.

Dimensional control and surface treatment are beyond the scope of this study.

1.2. Additive Manufacturing Regulatory Framework

Additive manufacturing (AM) is revolutionizing the traditional aerospace part design and manufacturing paradigm. For existing designs, additive manufacturing offers the ability to reduce cost, especially for one-of-a-kind or limited production run quantities. For new designs, high cost and long lead times associated with the production of complex hardware by conventional manufacturing routes have convinced manufacturers to rely on meticulous analyses to mitigate or eliminate the chance of failure. With the advent of additive manufacturing, prototype hardware designs can be iterated early in the design cycle with minimal cost and impact to schedule,

restoring the role of incremental testing and iterative redesign (Froes & Boyer, 2019).

However, while AM is experiencing rapid successful adoption in the aerospace, automotive, and medical fields, AM is still considered a developing technology. Regarding the lack of established associated standards and certification for AM-produced components, the majority of current AM usage has been restricted to non-mission critical applications within the aerospace industry. To address these issues, manufacturers and regulatory aviation bodies are increasingly working towards the development of new standards to meet the current capabilities of AM. Moreover, it should be noted that both academic institutions and commercial companies have established their own classifications of AM technologies due to the lack of such unified standards, which has often resulted in confusing and contradictory categorization of AM processes and nomenclatures. So far, a number of standards regarding metal AM in general have been developed; standards include the ISO/ASTM52900-15 regarding standard AM terminology, the ASTM F3122-14 regarding the evaluation of mechanical properties of metal AM parts, and the ASTM F3049-14 regarding the characterisation of metal powders used for AM processes. However, only a few standards and qualifications have been established in the context of the application of metal AM within the aerospace industry; examples include the MSFC-STD-3716 regarding spaceflight hardware fabricated by laser powder bed fusion (L-PBF) metal AM processes and SAE AS9100 regarding the requirements for quality management systems in aviation, space, and defence organizations. Significant efforts are therefore still required to fully integrate the standards for metal AM and specifically to meet the requirements of aerospace applications, which are currently pioneered by the National Aeronautics and Space Administration (NASA). Nevertheless, these established standards are particularly useful to policy makers and to the AM community in general and have become fundamental guidelines in developing further standards and qualifications that focus on the aerospace industry (Yusuf et al., 2019).

Chapter 2

Literature review

This chapter contains an up-to-date review of the literature on Laser Powder Bed Fusion, including critical process parameters, and defects present in this technology; powder parameters influence, such as particle size distribution, chemical composition, morphology, and flowability; AlSi10Mg, and in the quality of parts, focusing on the regulation of additive manufacturing of parts for the aviation sector.

2.1. Laser Powder Bed Fusion

Today's concept of additive manufacturing technologies emerged from the term "rapid prototyping" (RP) that was widely used for reduction of process time to facilitate rapid creation of parts which were to be subsequently fabricated and commercialized (Srivastava et al., 2020).

Development of AM technologies was gradual over the first decade of its advent. However, recently owing to advancements in manufacturing, associated technologies, customer expectations and global markets, the development rates have witnessed a huge upsurge. The first AM patent was filed in 1980 in Japan by Dr. Kodama (Srivastava et al., 2020).

The twenty-first century saw a shift in the AM applications paradigm from R&D and prototyping to industrial and functional part fabrication. The term RP has gradually been replaced by AM, which includes both direct and indirect AM and involves a variety of aspects of prototyping, tooling and manufacturing. Emergence of technologies like selective laser melting (SLM) (2000), Envision Tec (2002), EBW/Exone (2005) was witnessed over time (Srivastava et al., 2020).

There are many different varieties of additive manufacturing technologies available which all aim to form prototypes or fully functional parts. A trait which all technologies have in common is the depositing of material and building of layers to form parts. The actual step of manufacturing using additive technology presents only a small step when considering the entire additive manufacturing timeline. Figure 2.1 shows this timeline beginning with the identification of suitable parts, moving over to the question if a business case exists, on to the actual design of the part. The generation of data for the build is followed by the actual step using additive technologies. After the building process further stages include the post-processing of the part and the separation from the base or building platform. The methods of additive manufacturing differ in the materials used and their method of operation. Possible materials include but are not limited to metals, polymers, ceramics or composites. Each method of operation works either on the principle of depositing layers by melting material or by curing material (Müller & Westkämper, 2018).

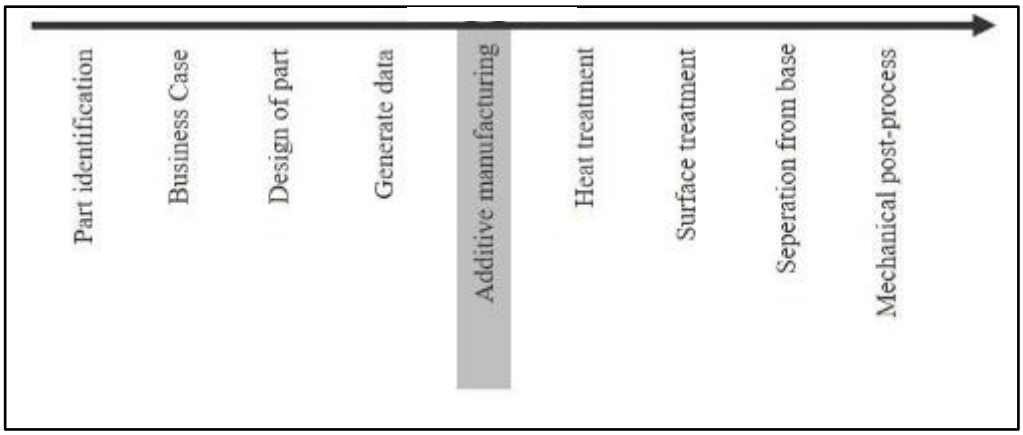

Figure 2.1 – Timeline of the additive manufacturing process. (Adapted from Müller & Westkämper, 2018).

Limbasiya et al., 2022) refers that ISO/ASTM 529000-15 established the general principles and terminology of the L-PBF for a method originally referred to as SLM, that is still used today.

The L-PBF AM process (Figure 2.2), a technology where the powder bed, deposited on the build platform (BP) by a recoater roller or blade, is scanned and melted through a laser beam characterized by a laser power (P) [W], and generated by one of the following energy sources: Yb:YAG fiber, Nd:YAG, CO_2 laser, infrared, etc (Ghio & Cerri, 2022). The moving mirror, controlled by a computer system, deflects the laser source according to the 3D project. Only when a layer is totally scanned and melted, the BP lowers by a quantity equal to the layer thickness (t, [mm]) and the recoater roller or blade spreads a new powder layer. This procedure is repeated until the complete 3D physical object is manufactured (Ghio & Cerri, 2022).

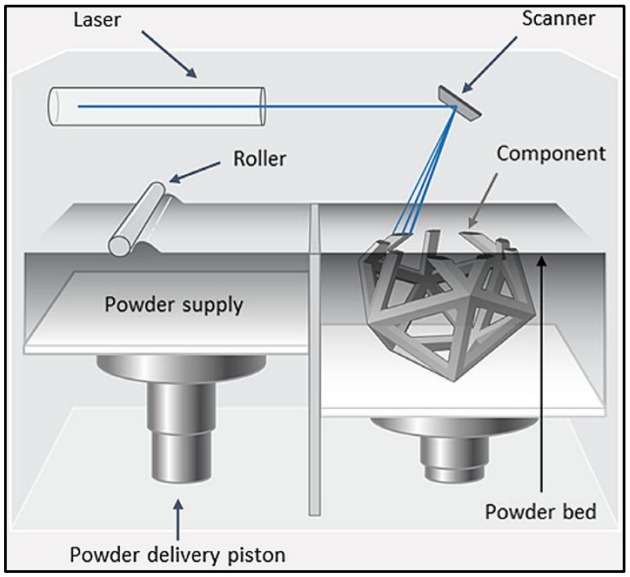

Figure 2.2 – Illustration of the powder bed process with the powder supply on the left-hand side and the powder bed on the right-hand side. (O'Brien, 2019)

During the L-PBF process, the laser beam transmits enough energy to melt the entire layer depth and a portion of the previously solidified layer, guaranteeing the adhesion between them. The molten pool (MP) depth is key to obtaining this adhesion and the absence of defects. Tang et al., (2017) illustrated the following criterion to have a full melting:

$$\left(\frac{h}{W}\right)^2 + \left(\frac{t}{D}\right)^2 \leq 1 \qquad (2.1)$$

where:

h - hatch spacing (mm), which is the distance between the centre of one laser scan track and the consecutive one (Figure 2.3), W – MP width (mm), D – total depth of the MP (mm), and t – layer thickness (mm). The full melting is obtained only if equation (2.1) is satisfied.

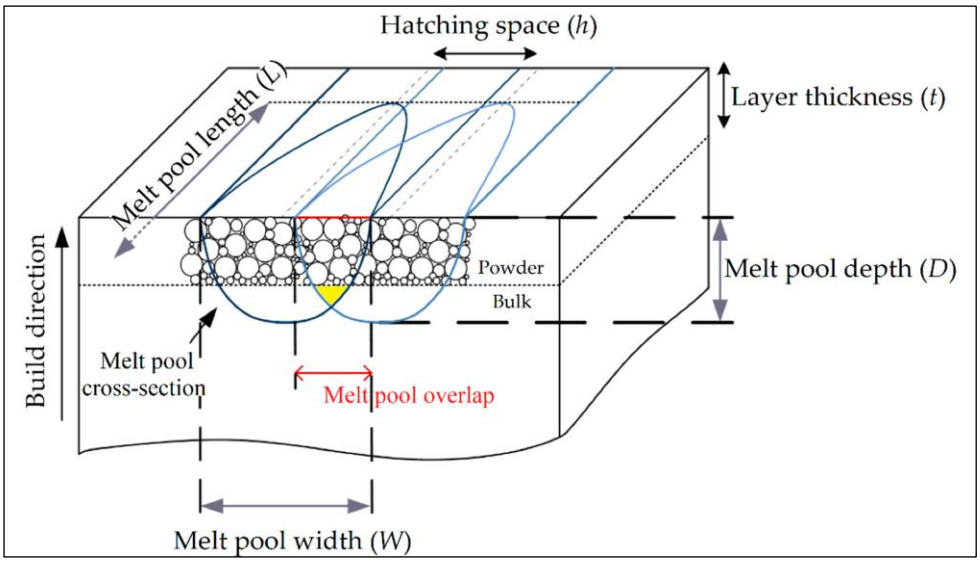

Figure 2.3 – Schematic representation of the interaction between the laser beam source and the powder bed during the L-PBF process highlighting the overlap area between two adjacent laser scan tracks where the principal dimensions are labelled (Ghio & Cerri, 2022).

Typically, when laser and powder particles come in contact during a laser powder bed fusion process, several phenomena can occur at the same time (Figure 2.4) and can be further classified as denudation and generation of the heat-affected powder (spatter and condensate), (Santecchia et al., 2020).

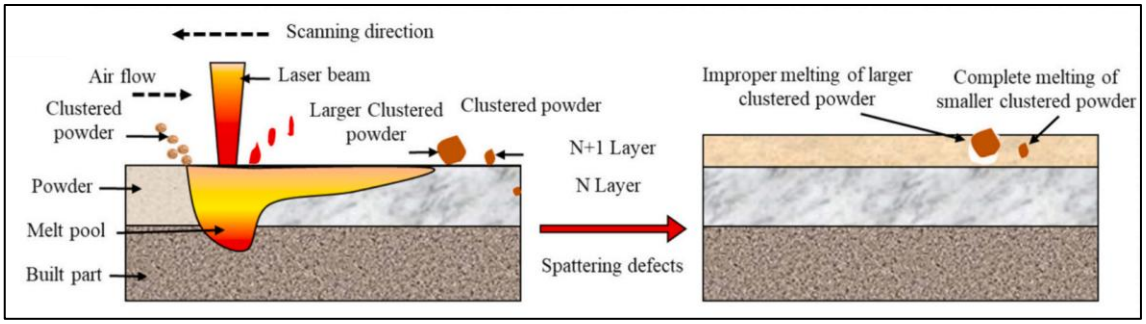

Figure 2.4 – Schematic representation of L-PBF process by-products formation and its influence of clustered particles (Kumar et al., 2026).

In the schematic shown in Figure 2.4, the various phenomena occurring during the passage of the laser over the powder in the L-PBF process, as well as their influence on subsequent layers, are illustrated. In Figure 2.5, panel (a) presents a schematic representation, while panel (b) shows a photograph depicting the denudation process and the generation of spattered particles.

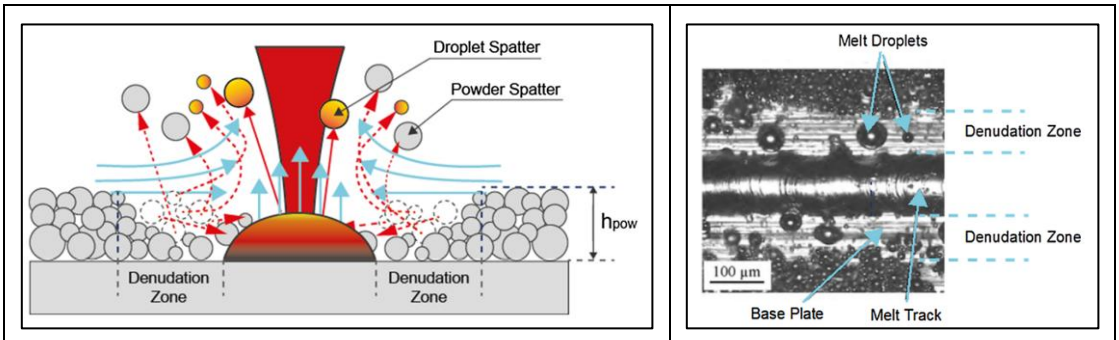

Figure 2.5 – Denudation and spatter particles in L-PBF process a) Scheme (Wischeropp et al., 2019), and b) Top view picture (Adapted from Yadroitsev et al., 2010).

Denudation is a term which defines the formation of apparent clearing zones around a single laser track (Santecchia et al., 2020).

In high power laser processes the gas directly above the interaction zone becomes ionised and a plasma plume is established. However, there is not only plasma in the welding plume. Due to the high energy density of the focused laser beam the melt pool reaches the evaporation point of certain alloying elements in the centre of the laser spot. As a consequence, vaporized metal is ruptured out of the melt pool. The vaporized metal is cooled down very quickly and condensates, forming particles with diameters between 10 nm and 150 nm. These particles can agglomerate and aggregate to different orders of magnitude depending on the duration of the condensation process (Ladewig et al., 2016).

According to Ion (2005) the term spatter describes liquid particles which are expelled during welding. Reason for the formation of spatter can be volatile alloying elements or instabilities in the keyhole during welding. Ladewig et al. (2016) reports that Meiners and Simonelli et al. have analysed the spatter formation during selective laser melting and found that spatter is noticeably bigger in size than the used powder, has a spherical form and is chemically identical to the raw material.

The SLM process is governed by the collection of process parameters presented in Figure 2.6 (ISO/ASTM 52930, 2021). The factors that received the most academical attention were laser power, scan speed, hatch space, layer thickness, and scan strategy (Figure 2.7). The laser power manages the quantity of energy supplied to the substrate. Depending on the material, sufficient laser power is used for the complete melting of the powder particles as partial melting leads to defects upon solidification due to insufficient filling of the melt pool space. Equivalently, scanning speed regulates the solidification and melting rates. The hatch space determines the overlapping of adjacent tracks in a layer which allows them to bond together by metallurgical bonding. Layer thickness defines the thickness of powder distributed in a single layer. Larger layer thickness leads to incomplete melting and defects, such as balling. To determine the combined impact of these variables, a parameter defined as volumetric energy density (J/mm^3), the most often form of energy density used by the researchers, is expressed as:

$$E = \frac{P}{v \times h \times t} \tag{2.2}$$

Where: P - laser power (W), v - scanning speed (mm/s), h - hatch space (mm), and t - layer thickness (mm) (Limbasiya et al., 2022).

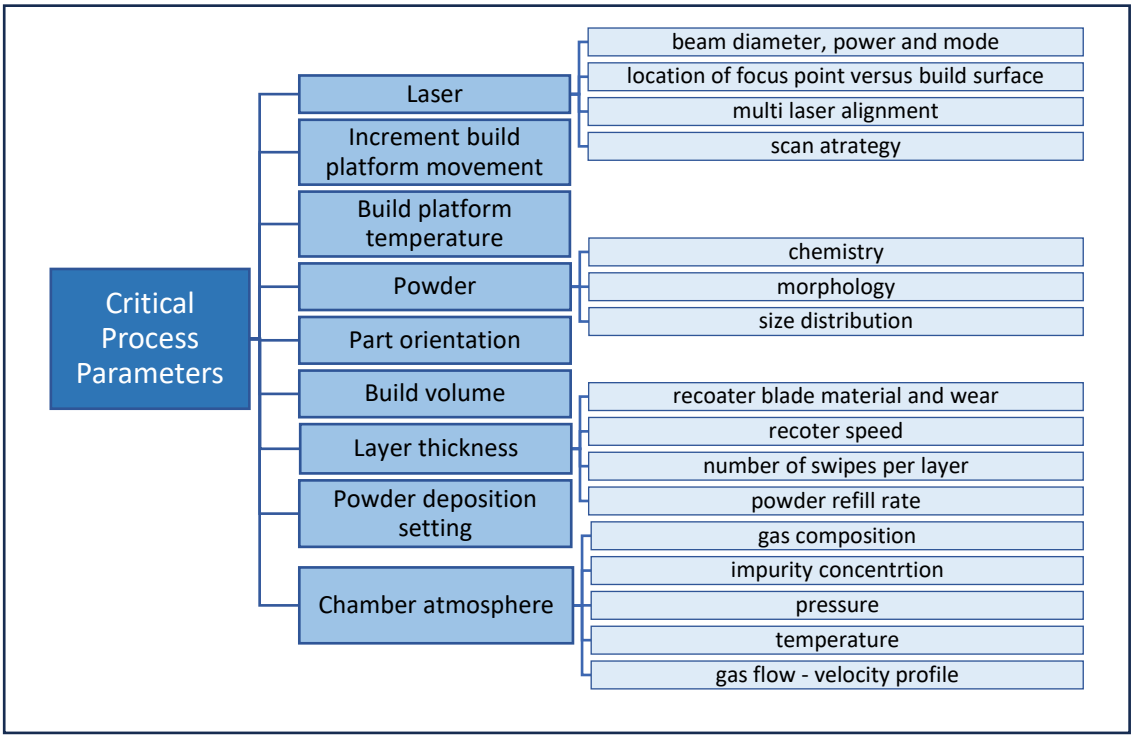

Figure 2.6 – Critical process parameters for additive manufacturing.

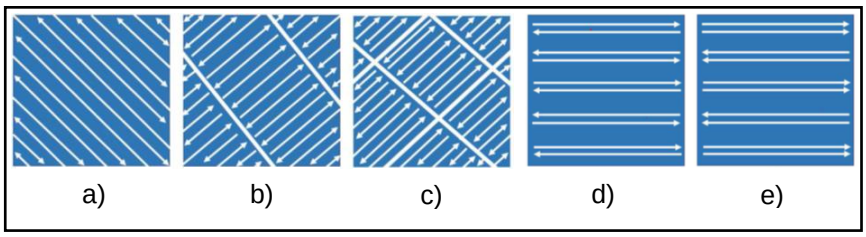

Figure 2.7 – Laser strategy. a) Meander, b) Striped, c) Chessboard, d) Remelting – Opposite direction, and e) Remelting – Same direction. Adapted from (Limbasiya et al., 2022).

For manufacturing processes, statistical techniques such as design of experiments, control charts and capability studies can be used to optimize the process, its capability and stability. Optimized process parameters that lead to acceptable quality levels and process capability (for manufacturing processes) or acceptable accuracy, precision, and sensitivity should be recorded as “baseline settings” and establish build parameters for subsequent builds, once the qualification builds have been validated (ISO/ASTM 52930:2021). Such settings can include but are not limited to the ones presented in Figure 2.6.

Concerning to the defects occurring in L-PBF, Ghio & Cerri, (2022) summarize in a table the types of defects, their causes, possible remedies, and their effects, Table 2.1.

Table 2.1 – Defects present into L-PBFed samples: Cause, remedy and effects.

Cause	Remedy	Effects
Lack-of-fusion (LOF)		
Inhomogeneous distribution of the powder bed	Reduction in the layer thickness and increase of energy penetration.	Decrease in mechanical properties and fatigue resistance.
Non-optimization of the ED function		
Lack of material or low energy including no complete adherence of the melt to the surrounding material		
Keyhole pore		
MP instability	Increase in energy depth penetration and laser power.	Decrease in mechanical properties and fatigue resistance
Non-optimised process parameters		
Gas pore		
Gas dissolution within the melt material	Reduction in the layer thickness, and the pressure into the chamber. Reduction in the O_2. Re-melting.	Loss density, decrease in tensile strength and fatigue resistance. Gas pores are less critical in crack propagation than LOF.
Gas wrapped into the gas atomized particles		
Entrapment of the gas present into the build chamber		
Gas flow within the build chamber		
Anisotropy		
Build orientation	HTs	Tensile properties correlated to the orientations.
Preferential evaporation		
Temperature-dependent vapor pressure	Reduction in linear energy rather than the hatch spacing	Alloying elements loss and pore's formation.
Residual stress and distortion		
High thermal gradient during the L-PBF process	Pre-heated BP. Post-Process HTs. Opportune scan strategy and re-melting. Sacrificial material and support structures.	Sample distortion if residual stress is higher than the YS. Alloying elements loss and pore's formation. Loss of tolerance requirement. Reduction in fatigue resistance and tensile properties.
Balling		
Low viscosity of melt material	Reduction in ED value	Porosity
Excess of melt material		Stress Concentration Point
MP instability: capillarity, Marangoni's effect		Surface quality and roughness
Splashing of MP due to its high surface temperature		Intralayer connection

Martucci et al. (2023) report four main types of defects observed in the PBF-LB/M processed parts of aluminium alloys: porosity, cracking, low surface quality and anisotropy, Figure 2.8.

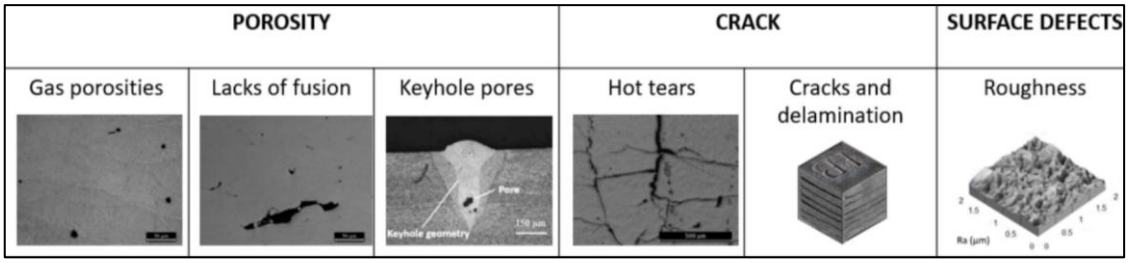

Figure 2.8 – Porosity, Crack and Surface defects observed in the L-PBF processed parts of aluminium alloys (Adapted from Martucci et al. (2023).

2.2. Powder Quality

2.2.1. Particle Size Distribution

Huck-Jones & Langley, (2017) refers that most feedstocks used in AM consist of fine powders with median particle sizes, typically in the range of 20-60 µm. This is essential to meet the requirement to form, for example, a powder bed just tens of microns thick. Fine particles can also be advantageous in terms of packing behaviour, especially in a powder with a relatively broad particle size distribution, Figure 2.9.

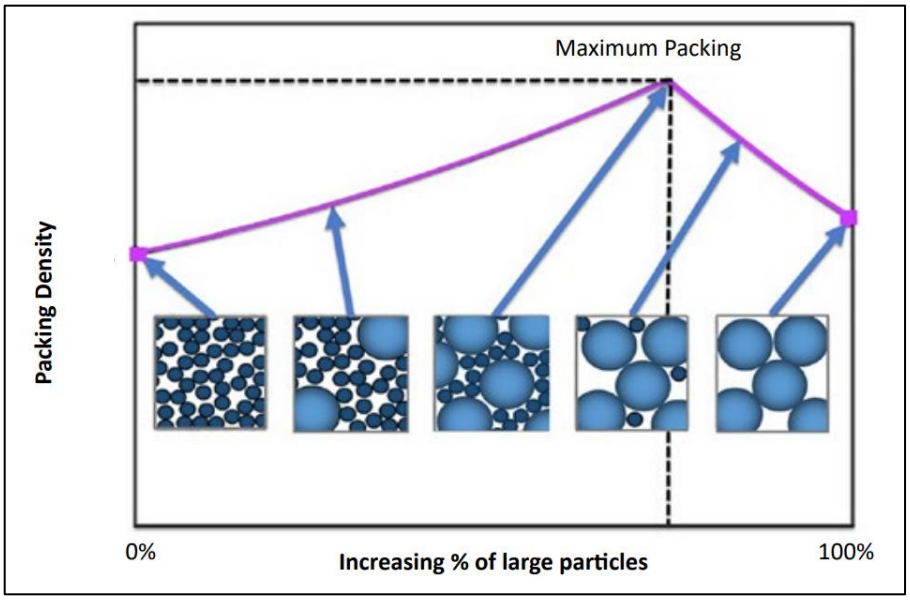

Figure 2.9 - High packing density is associated with the production of high quality, minimally flawed components and can be achieved using a powder with a relatively broad particle size distribution (Huck-Jones & Langley, 2017).

Such powders deliver the high bulk density associated with consistently high quality, minimally flawed finished components (Huck-Jones & Langley, 2017).

Particle size characteristic x_{area} represents the diameter of a spherical particle with the same area as the real particle even if it is not spherical, as shown in Figure 2.10

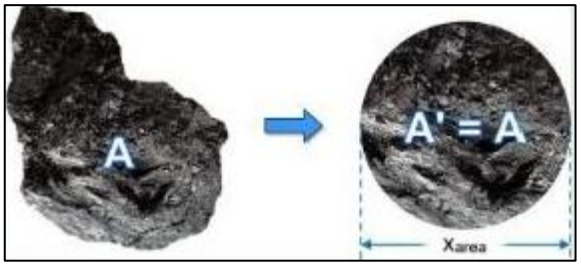

Figure 2.10 - Correspondence between area from a non-spherical particle and a spherical particle and x_{area} representation.

2.2.2. Chemical Composition

Chemical analyses are carried out on the powder used in the additive manufacturing process in order to assess its quality. The chemical composition of the metallic shall be determined by suitable testing procedure, e. g. wet chemical process, atomic absorption spectrometry, flame emission spectroscopy, or X-ray fluorescence analysis (ISO/ASTM 52907:2019, 2019).

Pavlinskii & Vladimirova, (2009) warns that X-ray fluorescence cannot detect the very lightest elements on the periodic table, with atomic number under ten. This includes hydrogen (H), helium (He), lithium (Li), beryllium (Be), boron (B), carbon (C), nitrogen (N), oxygen (O), and fluorine (F). This is a direct consequence of the fundamental physics governing these low-atomic-number elements. For very light elements, another physical process called the Auger Effect becomes more probable than X-ray fluorescence. Instead of the atom emitting a fluorescent X-ray, the energy from the electron transition is used to eject a different electron from the atom. This process competes directly with fluorescence, decreasing the signal that an XRF detector is designed to measure.

2.2.3. Powder Morphology

While smooth, spherical powders may be preferable for many AM applications, they can be difficult to manufacture. The majority of metal powders for AM are produced using gas atomisation processes and the resulting product tends to be relatively spherical. However, particle shape can be influenced by the thermal conductivity of the molten metal, which affects the speed of cooling during particle formation and the associated solidification process. In addition, collisions and subsequent fusion between molten/semi-molten particles can form irregularly-shaped particles (Huck-Jones & Langley, 2017).

In reality, gas atomised metal powders may contain particles exhibiting any of the features

illustrated in Figure 2.11.

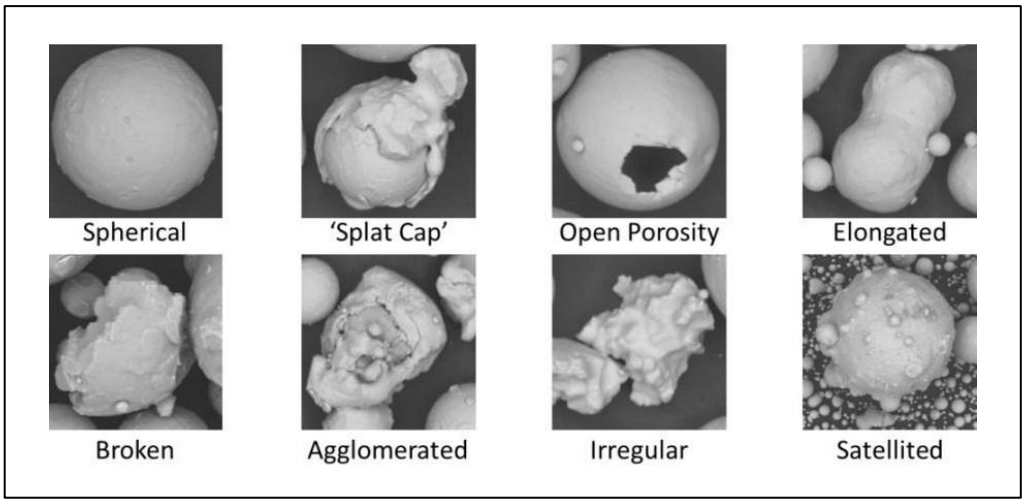

Figure 2.11 – Powder morphology (Huck-Jones & Langley, 2017).

2.2.4. Flowability

Flowability is a criterion of the free-flow ability of a powder without creating aggregations or clusters. Flowability is measured as the time required for a certain volume of powder to pass through a rotary cylinder (Sefat et al., 2023). Density, electric charge, size, shape of dry particles (Sefat et al., 2023), porosity, and surface texture, (Huck-Jones & Langley, 2017) are the main effective parameters on flowability.

Due to the increase in interparticle attractive forces as particle size decreases, finer particles generally exhibit reduced flowability (Huck-Jones & Langley, 2017). Martucci et al. (2023) show (Figure 2.12) the best scenario for the highest powder packability a), and the best scenario for powder flowability b).

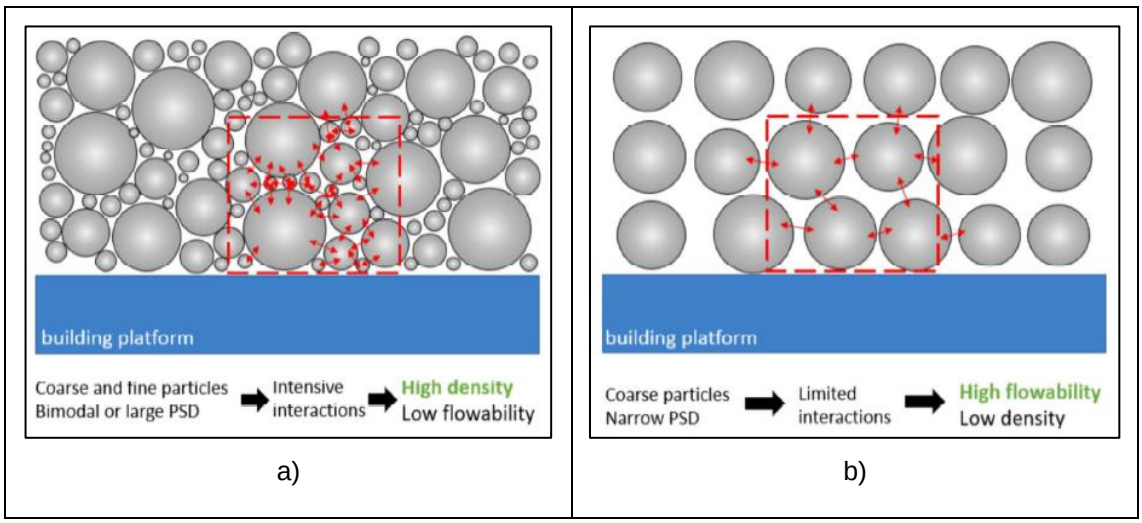

Figure 2.12 – The best scenario for: a) the highest powder packability, and b) powder flowability. (Adapted from Martucci et al., (2023)).

2.3. AlSi10Mg

AlSi10Mg is an age-hardening alloy based on the Al-Si-Mg ternary system and is characterized by low density (2.67 g/cm^3), good mechanical properties, excellent castability and capability of being heat-treated (Ghio & Cerri, 2022). During the SLM forming process, the AlSi10Mg alloy forms a unique microstructure due to the rapid cooling rate and highly localized heat input, which is mainly composed of the α-Al matrix and the Si phase network distributed inside. This microstructure gives the material high strength and hardness, but also leads to high residual stress and brittleness (Wang et al., 2025).

The Al-Si phase diagram, shown in Figure 2.13, highlights the fact that AlSi10Mg presents a short solidification range (ΔT ~ 40 ºC), making it the most common aluminium alloy used in additive manufacturing (AM) (Ghio & Cerri, 2022).

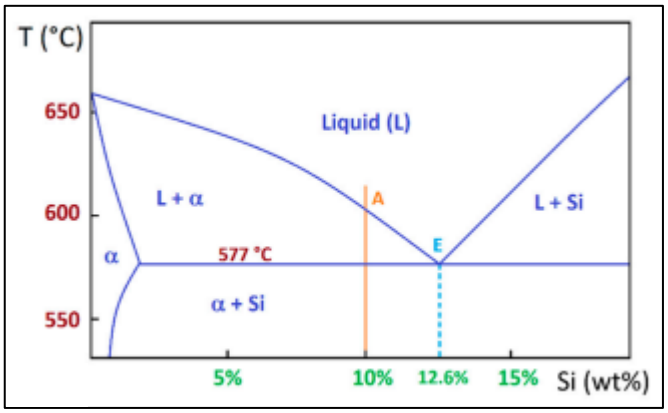

Figure 2.13 – Al-Si phase diagram. (Ghio & Cerri, 2022)

The as-built microstructure of the hypoeutectic AlSi10Mg alloy L-PBF-ed is shown in Figure 2.14 where two different machine setups are compared. Figure 2.14 a) and c) illustrate the sample manufactured with a single laser, while Figure 2.14 b) and d) those with multi-laser (4 x 400 W). Figure 2.14 a) and b), both optical micrographs performed along the xy plane show the laser scan tracks sections that are placed according to the scan strategy. At the same time, it is possible to highlight the typical semi-ellipsoidal shape of the molten pool. The microstructure along the built direction (Figure 2.14 c) and d)) presents a typical fish-scale morphology due to the overlapping of the laser scan tracks, (Ghio & Cerri, 2022) as shown in Figure 2.14.

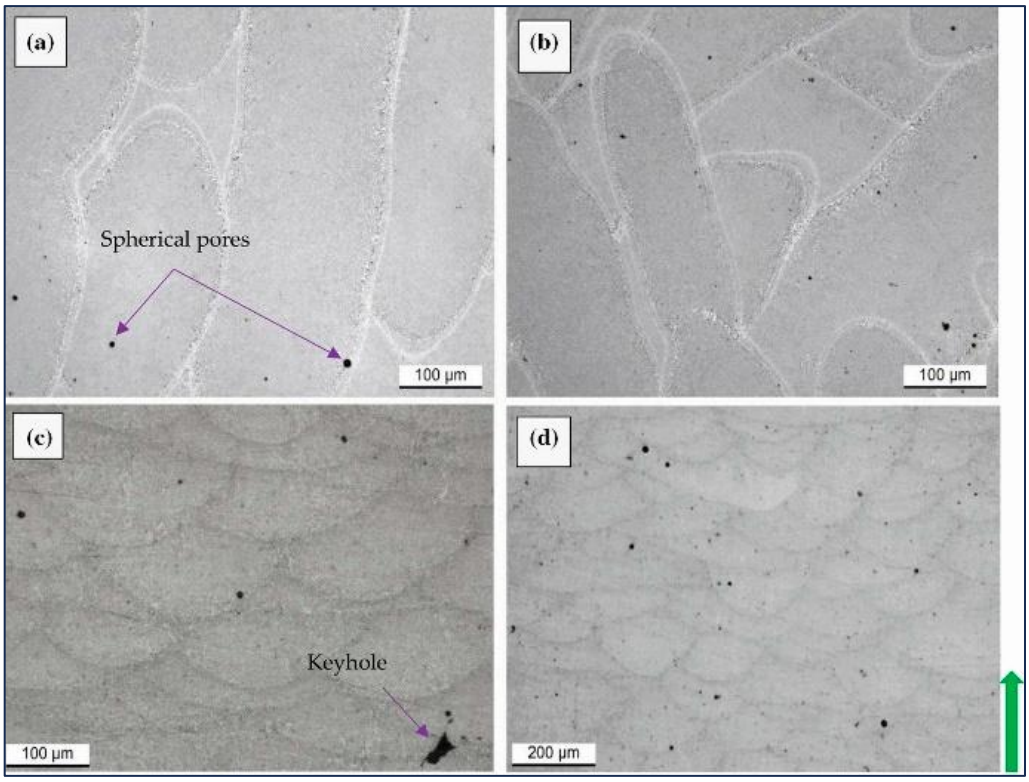

Figure 2.14 – Optical Microscopy micrographs of the as-built AlSi10Mg samples along the xy (a and b) and xz (c and d) planes. Panels (a and c) are related to the single laser machine set-up and (b and d) to the multi laser. The green arrow indicates the build direction (Ghio & Cerri, 2022).

Some defects can also be observed in the optical microscopy micrographs shown in Figure 2.14. In a) shows spherical pores, also referred in literature to as gas pores, are indicated, while in c) the keyhole defect is displayed.

Syrlybayev et al. (2024) and Song et al. (2024), among others show in a closer look to as-printed melt pools a fibrous heterogenous cellular-dendritic microstructure consisting of a fine eutectic Si network surrounding the α-Al cells of gradient size, as shown in Figure 2.15.

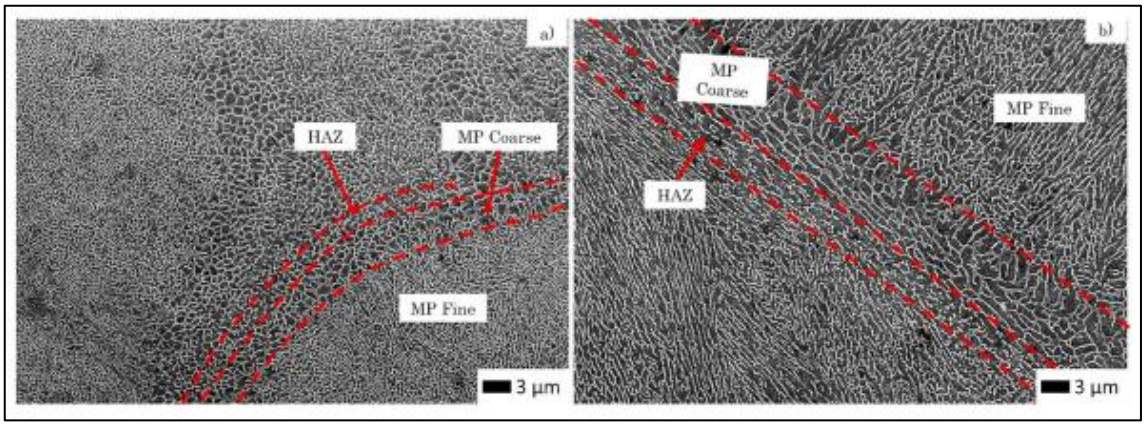

Figure 2.15 – Microstructure of the as-built AlSi10Mg alloy captured at a) transverse and b) longitudinal sections. (Syrlybayev et al., 2024)

At melt pool boundaries, Figure 2.15, the cells form a coarse zone indicated as MP Coarse, in which the cells are larger than inside the melt pool (MP Fine zone). The heat-affected zone (HAZ) forms outside the melt pool boundary, where the network is partially broken (Syrlybayev et al., 2024).

Phutela et al. (2023) and Bosio et al. (2023) also show SEM micrographs tracking microstructure evolution and variation of Si distribution in AlSi10Mg at different build platform temperatures, Figure 2.16.

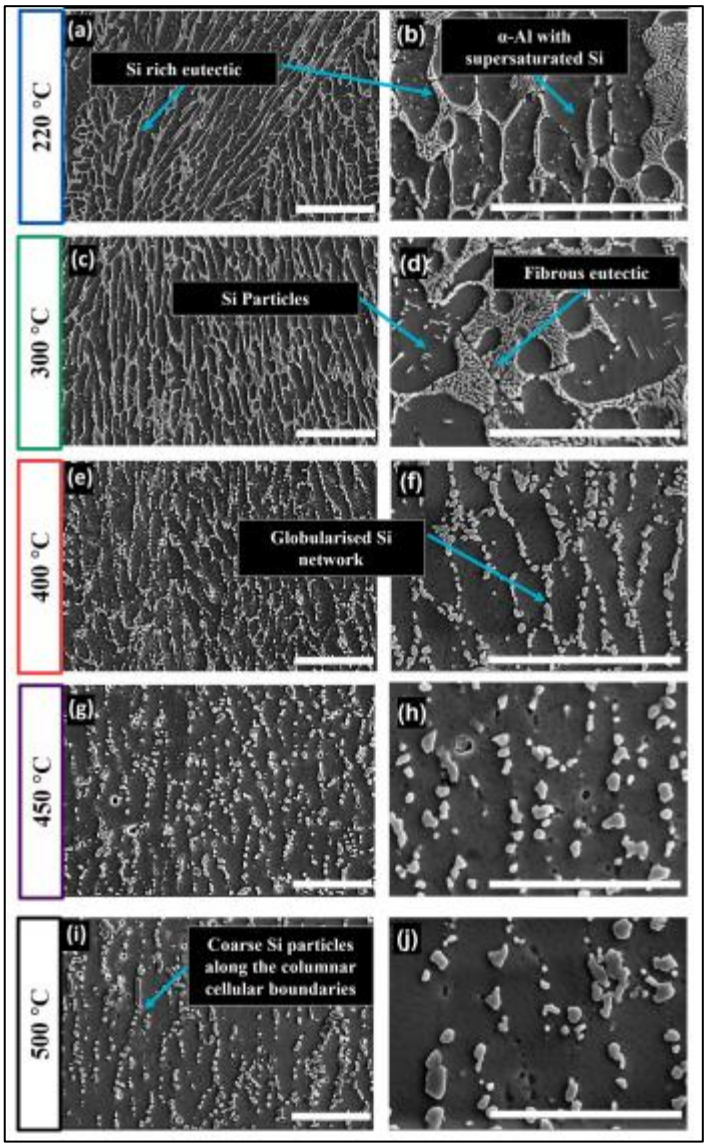

Figure 2.16 – SEM micrographs tracking microstructure evolution in AlSi10Mg at different build temperatures. All the scale bars in the micrographs represent 5 µm (Phutela et al., 2023).

The ratio between the thermal gradient (G) and the solidification rate (R) determines the microstructures' morphology obtained after the solidification process and, while G x R determines the grain size. In the first case, the relationships between G and R allow for obtaining a

solidification map as show in Figure 2.17 (Ghio & Cerri, 2022).

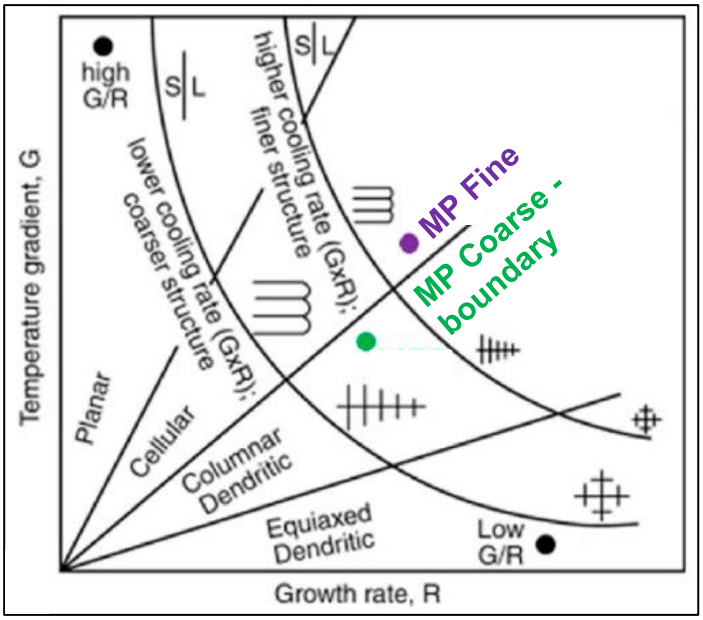

Figure 2.17 - Solidification map obtained by the G/R and G×R factor. Adapted from (Ghio & Cerri, 2022).

2.4. Compilation of Standards for Process Qualification

The entire process begins with a purchase order request from the client, whether internal or external. The client specifies the requirements, providing the design and detailed specifications regarding dimensions and tolerances. The technical team positions the 3D model of the part on the build platform and generates support structures as indicated by the software. The part orientation should aim to minimize residual stress concentration and the amount of generated support structures, while maximizing the number of parts placed on the build platform to ensure cost-effective utilization of the build. At this stage, test specimens are digitally integrated into the build platform layout. Once the build program is finalized, it is uploaded to the machine, which then initiates the production process.

There are already international standards that regulate additive manufacturing, the ASTM 52900 series. ISO/ASTM 52901:2016, (2016) standard regulates the purchase of these additively manufactured parts.

The feedstock, in this case the AlSi10Mg alloy powder, is regulated by the ISO/ASTM 52907:2019 standard.

Once the parts have been manufactured using the L-PBF process, it may undergo heat treatments and/or surface treatments, and potentially mechanical post-processing, as illustrated in Figure 2.1, depending on the customer's requirements.

The following sub-sections outline specific requirements and characteristics of the standards involved throughout the entire process.

2.4.1. Requirements for Purchased AM Parts – ISO/ASTM 52901:2016

The following elements:

- Part ordering information (Table A1.1 – Appendix 1);
- Definition of the part to be manufactured (Table A1.2 – Appendix 1);
- Part characteristics, functionality and performance (Table A1.3 – Appendix 1);
- Acceptance (Table A1.4 – Appendix 1)

shall be included in the purchase order subject to agreement between the customer and the part provider (ISO/ASTM 52901:2016, 2016). The information contained in Tables A1.2 and A1.3 of Annex 1 is essential for the manufacturing order.

2.4.2. Requirements for feedstock materials – Methods to characterize metallic powders – ISO/ASTM 52907:2019

ISO/ASTM 52907:2019 provides technical specifications for metallic powders intended to be used in additive manufacturing and covers the following aspects: documentation and traceability; sampling; particle size distribution; chemical composition; characteristic densities; morphology; flowability; contamination and packaging.

ISO/ASTM 52907:2019, (2019) refers that the supplier and customer shall choose the test methods appropriate to the customer's requirements. To ensure traceability, statements of conformity and inspection documents shall specify the following: a unique document reference, the name and the address of the supplier, the reference of powder lot, the product description, including chemical composition, standard and/or trace/common name, the nature of powder production process, the packaging description, including the packaging, the nature of the shielding gas and the desiccant bag, if relevant, the date of analysis, storage and preservation instructions, and all of the information to ensure the traceability. Samples shall be representative of the powder lot, ensuring homogeneity when split.

2.4.3. Additive Manufacturing – Process Characteristics and Performance: Practice for Metal Powder Bed Fusion Process to Meet Critical Applications – ISO/ASTM 52904:2019

This practice describes the operation and production control of metal powder bed fusion machines and processes to meet critical applications such as commercial aerospace components and medical implants. The requirements contained herein are applicable for production components and mechanical test specimens using powder bed fusion with both laser and electron beams (ISO/ASTM 52904:2019, 2019).

2.4.4. Additive Manufacturing - Finished part properties – Specification for AlSi10Mg with Powder Bed Fusion – Laser Beam – ASTM F3318-18

ASTM F3318 regulates terminology, material condition, ordering information, manufacturing plan, feedstock, process, Post build chemical composition, requirements, microstructure, mechanical properties, thermal processing, dimensions and permissible variations, retests, inspection, rejection, certification, product marking and packaging, quality program requirements, and significance of numerical limits for additively manufactured AlSi10Mg parts.

The metal powder shall be free from detrimental amounts of inclusions and impurities, and its chemical composition shall be adequate to yield, after processing, the final chemical composition listed in Table 2.2 (ASTM International F3318-18, 2018).

Table 2.2 - Chemical composition of parts made by AlSi10Mg alloy.

Element	Chemical composition % (w/w)
Al	Balance
Cu	≤ 0.05
Fe	≤ 0.55
Mg	[0.20; 0.45]
Mn	≤ 0.45
Ni	≤ 0.05
Pb	≤ 0.05
Si	[9; 11]
Sn	≤ 0.05
Ti	≤ 0.15
Zn	≤ 0.10
Other (each)	≤ 0.05
Other (total)	≤ 0.15

The microstructural requirements and frequency shall be mutually agreed upon by the part supplier and purchaser. Specimen preparation shall be in accordance with Guide E3 and Practice E407. Tension test specimens shall be prepared in accordance with Test Method E8/E8M either before or after thermal processing as agreed upon by the supplier and purchaser. In accordance with ISO/ASTM 52921:2013, (2013), specimens used for tension testing shall be machined from bulk deposition, or taken from near net shape specimens. Table 2.3 shows the minimum tensile properties established by ASTM F3318 standard.

Table 2.3 - Minimum Tensile Properties (ASTM International F3318-18, 2018).

Material Condition	Tensile Strength (MPa)	Yield Strength at 0.2% offset (MPa)	Elongation %
SR1	241	138	10
SR2	345	207	4
T6	345	207	5
HIP + T6	276	207	10
NHT	413	220	4

SR1 – 285 ºC (± 14 ºC), held for 120 min (± 15 min) and cooled at a rate equal to air cooling or faster.

SR2 – 190 ºC (± 14 ºC), held for 120 min (± 15 min) and cooled at a rate equal to air cooling or faster.

T6 – 530 ºC (± 6 ºC), held for 360 min quenched in water or glycol and aged at 160 ºC (± 6 ºC) for 360 min minimum.

HIP + T6 – under an inert atmosphere at 100 MPa minimum within the range 510 ºC to 520 ºC, held at the selected temperature within ± 14 ºC for 180 min ± 60 min and cooled under inert atmosphere to below 93 ºC, followed by T6 processing (ASTM International F3318-18, 2018).

Chapter 3

Methods

A brief introduction will present the equipment used in the production process at LAUAK Grândola. The powder flow will be described to clarify the types of powder studied. The process of specimen production, powder sampling, and sample characterization will also be explained.

Powder characterization included analysis of particle size distribution, chemical composition, and flowability. Specimens were characterized by measuring relative density, tensile strength, hardness along the specimen, and performing microstructural analysis.

3.1. RenAM 500Q Ultra

The RenAM 500Q Ultra (Figure 3.1) belongs to the RenAM 500 Ultra series, which offers three versions: S, D, and Q, corresponding to Single, Dual, and Quad lasers, respectively. These models come with on-board powder filtration and recirculation systems. They also feature advanced TEMPUS™ technology and have LaserVIEW™ and MeltVIEW™ hardware installed as standard, enhancing the precision and efficiency of the manufacturing process (Renishaw, 2024).

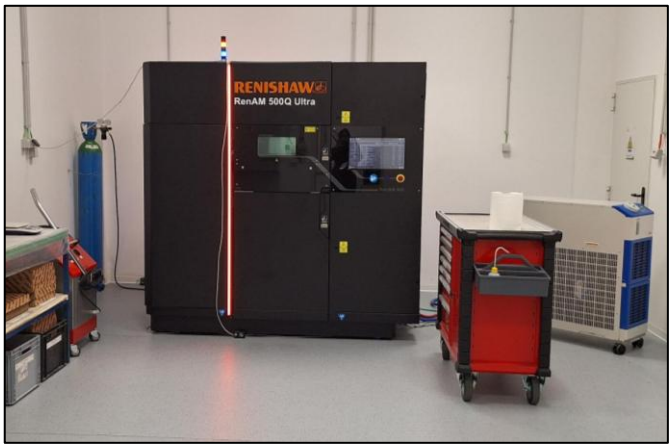

Figure 3.1 – RenAM 500Q Ultra at LAUAK Grândola Additive Manufacturing workplace.

TEMPUS technology is an upgrade package for the RenAM 500 series that can deliver up to a 50% reduction in build times (depending on part geometry) without compromising on part quality. TEMPUS technology synchronises the control of the lasers and recoater assembly so that the lasers can fire onto the powder bed whilst the recoater is moving across it. This means that the machine no longer has to wait for the recoater to finish spreading a new layer of powder before starting the next layer. Instead, the lasers can immediately start melting the next layer by strategically moving around the recoater as it deposits fresh powder Figure 3.2 (Renishaw, 2024).

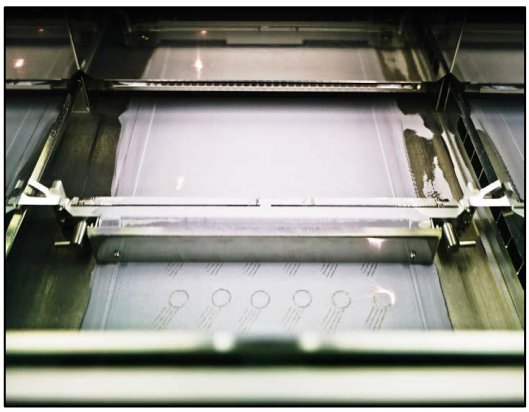

Figure 3.2 – Lasers firing as the recoater deposits a new layer of powder (Renishaw, 2024).

Unfortunately, the software that enables access to the data collected by LaserVIEW™ and MeltVIEW™ has not been operational to date, which hinders the development of the process.

Figure 3.3 shows a schematic front view from RenAM 500 series, and Figure 3.4 the same front view with powder fill and large SafeChange filter door open, where load hopper filling point (9), load hopper (6), load hopper level load cells (5), powder return pipe (7), and ultrasonic sieve system (2) are shown.

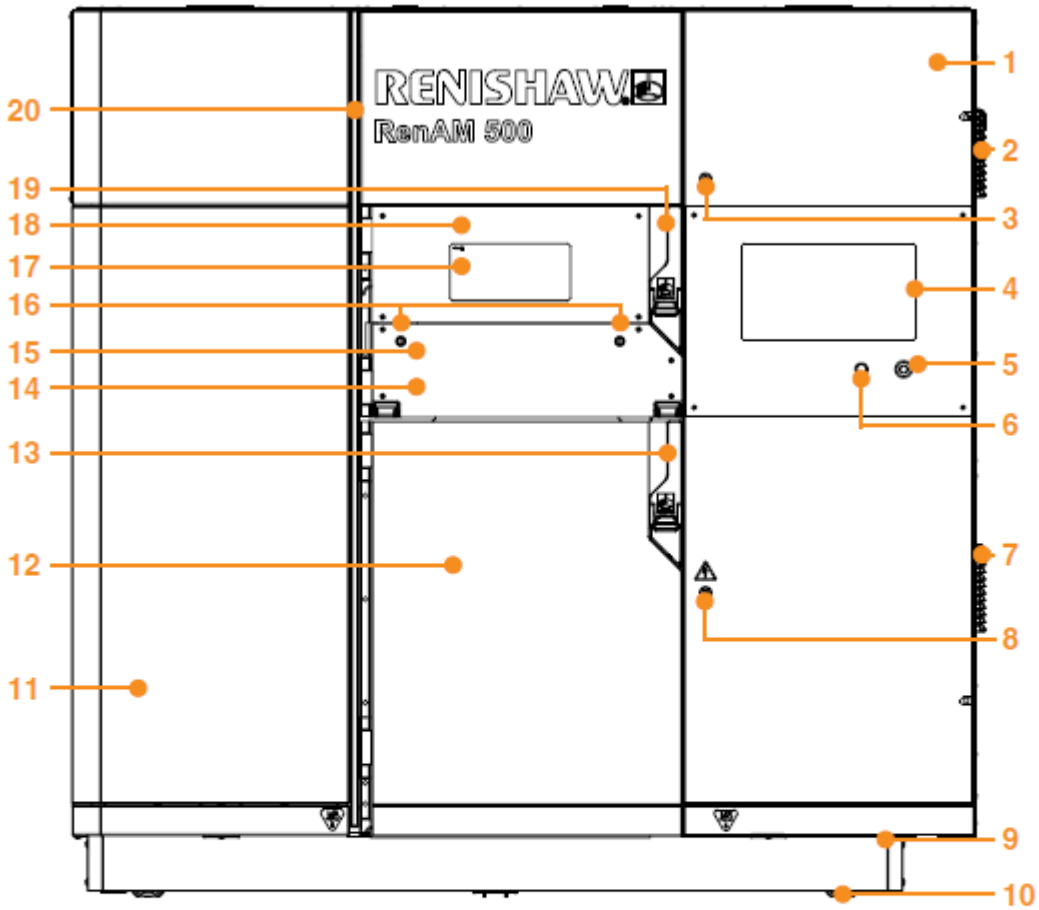

1	Front right-hand electrical cupboard door	11	Front left cupboard door – powder fill/overflow and large SafeChange filter change
2	Air vent	12	Bottom door
3	Security lock	13	Bottom door handle with interlock
4	Operator touch screen control panel	14	Glovebox lockable door with interlock
5	"Emergency Stop" button	15	Build chamber access gloves (behind door)
6	"Reset" button	16	Glovebox door locks
7	Air vent	17	Build chamber viewing window
8	Security lock	18	Top door
9	Plinth (covering combined castor and adjustable jacking feet)	19	Top door handle with interlock
10	Combined castor and adjustable jacking feet (behind plinth) × 5	20	LED strip light

Figure 3.3 – RenAM front view (Renishaw, 2024).

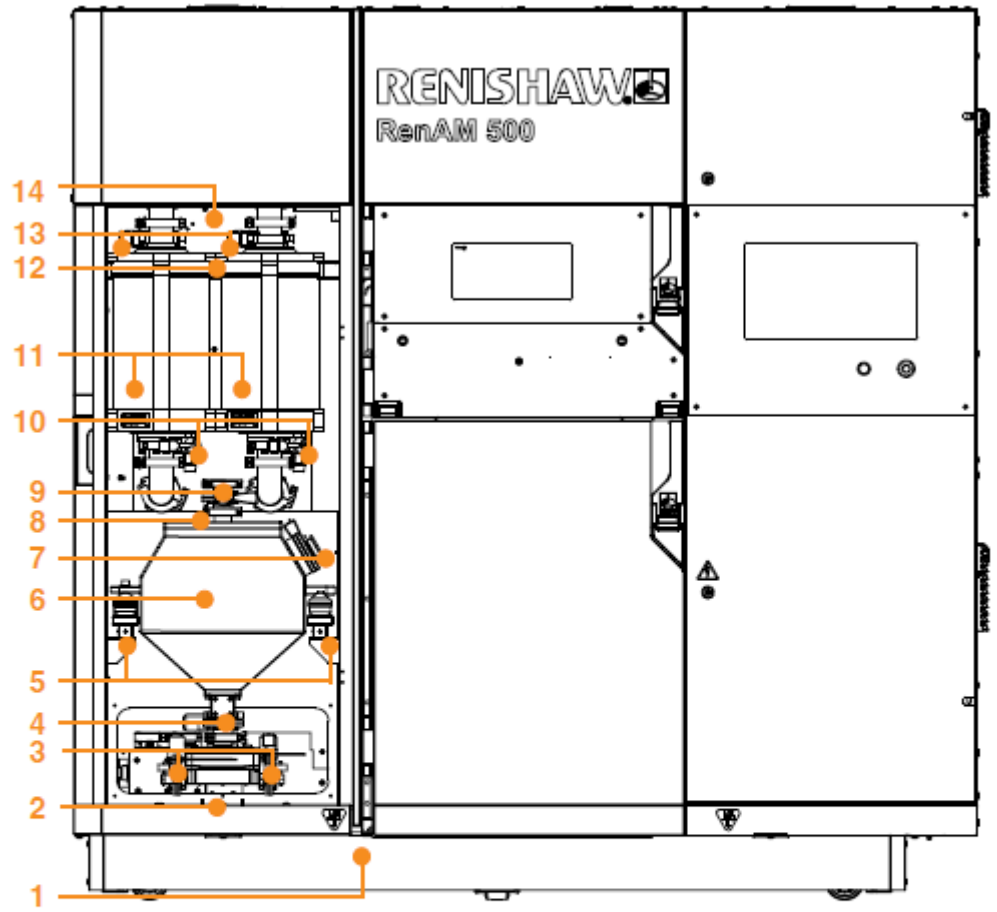

1	Powder fill and large SafeChange filter left-hand door open (shown removed)	8	Load hopper filling point isolation valve (not present on RenAM 500 Flex)
2	Ultrasonic sieve system (not present on RenAM 500 Flex)	9	Load hopper filling point (not present on RenAM 500 Flex)
3	Powder system isolation valves (not present on RenAM 500 Flex)	10	Large SafeChange filter lower isolation valves
4	Powder metering screw feeder (not present on RenAM 500 Flex)	11	Large SafeChange filter number 1 (left- hand) and large SafeChange filter number 2 (right-hand)
5	Load hopper level load cells (not present on RenAM 500 Flex)	12	Large SafeChange filter status indicator
6	Load hopper (not present on RenAM 500 Flex)	13	Large SafeChange filter upper isolation valves
7	Powder return pipe	14	Oversized particle collection point

Figure 3.4 – RenAM front view with powder fill and large SafeChange filter door open (Renishaw, 2024).

The lasers provide the energy source for the additive manufacturing process. The lasers are located in the right-hand rear of the RenAM 500 series cabinet. The laser system includes four 500 W lasers (Figure 3.5 a)) which have been specifically designed and engineered for this application. The lasers are 500 W ytterbium fibre type, with dynamic focusing carried out in the optical module (Renishaw, 2024).

The dynamic focusing lens is located in the optical system and focuses the laser beam on to the metal powder surface on the build platform located in the build chamber. The lens protection window (Figure 3.5 b)) protects the focusing lenses and steering mirrors from contamination (Renishaw, 2024).

The top door of the RenAM 500 series features a viewing window and a protective insert (Figure 3.5 c)). This meets the standard ANSI Z136.1 – 2007 and is specified to protect the user against scattered laser radiation for the wavelength used in the RenAM 500 series. The viewing window is located in the top door and in this application permits a Class 1 laser specification to be achieved (Renishaw, 2024).

Since the process is oxygen sensitive, an inert gas enters the build chamber from the top and lower right-hand sides of the build chamber (Figure 3.5 d)) It creates a flow of gas directed across the build plate from right to left. The finest metal powder and nanoparticles (known as condensate) produced during the build process are collected and directed to a port on the lower left-hand side of the build chamber which is connected via a cyclone separator to the two large SafeChange filters. The two large SafeChange filters are located and accessed through the left-hand door of the system cabinet. The large SafeChange filters are replaced when indicated on the touch screen control panel.

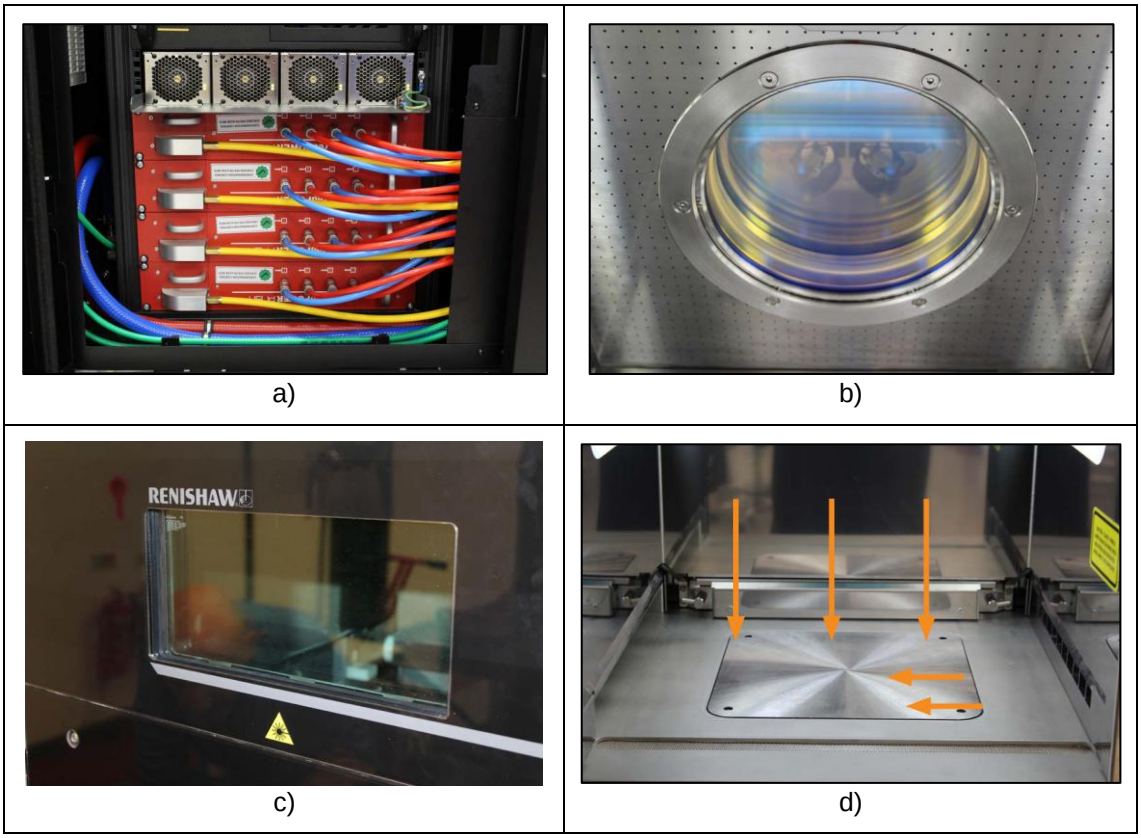

Figure 3.5 – a) Four PRISM lasers with laser output and cooling connections, b) Lens protection window, c) Build chamber viewing window, and d) Gas circuit (Renishaw, 2024).

3.2. Powder Flow

For a clearer understanding of the different types of powder generated during the production process, Figure 3.6 illustrates the powder flow throughout the L-PBF process.

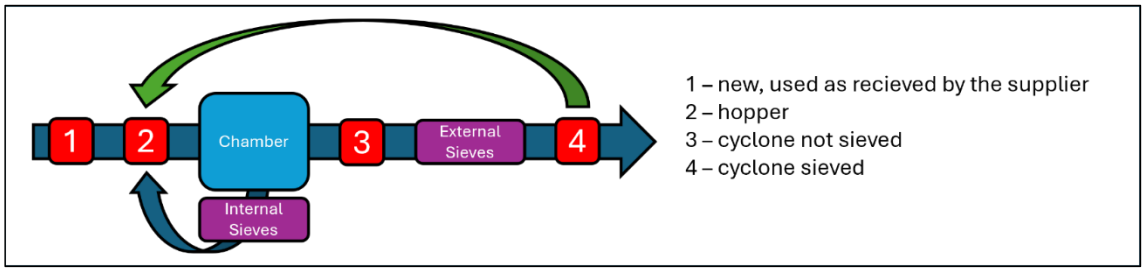

Figure 3.6 – Flow of powder during AM process.

Powder 1 refers to the powder as received by the supplier, Figure 3.7 a). Since day one, the machine has only been fed with new powder (powder 1, Figure 3.7 b)) from supplier 1. This powder is put into the hopper, Figure 3.7 c). Inside the hopper are the leftover powder from previous builds that have passed through the chamber's sieve (95 µm) (powder 2). Figure 3.7 d) and f) show a build inside the chamber with the powder from the bed trapped in the part. The sieved powder goes to the hopper (powder 2) (blue curved arrow in Figure 3.6). The oversized powder goes to a flask. This powder is discharged, since it can't be used, due to its size over 95 µm. During the process the argon flow removes some particles from the powder bed. These particles are taken to a cyclone, Figure 3.7 f) which extracts the powder particles from the argon flow into a flask, Figure 3.7 g) (powder 3). After an external sieving (63 µm) in the powder recovery system, Figure 3.7 h) and further analysis this powder can be utilised (powder 4).

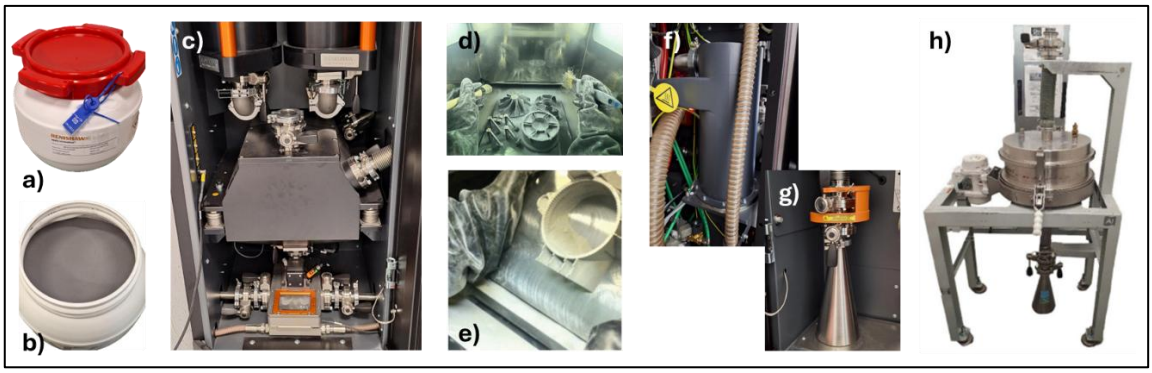

Figure 3.7 – a) powder as received by the supplier b) new powder (powder 1); c) hopper (powder 2); d) build inside the chamber, e) powder trapped inside the part (powder 2); f) cyclone; g) cyclone flask (powder 3); h) powder recovery system (powder 4).

3.3. Specimens' Production and Powder Sampling

In this work same of the production parameters of the builds were studied are given in Table 3.1.

Table 3.1 – Parameters of the studied builds.

Build								
Nr.		35	41	45	46	47	48	51
Picture			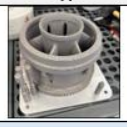					
Parameters								
Laser Strategy		Meander	S&C	Stripe	Stripe	Stripe	Stripe	Stripe
Thickness (µm)		60	30/60	60	60	Sp:60 B:30	60	60
Layer Time (min)	Max	0.507	0.500	0.500	0.615	1.086	0.472	0.649
	Min	0.200	0.176	0.131	0.130	0.400	0.215	0.196
Build T (hh:mm)		20:29	15:54	07:26	07:16	20:00	08:53	12:47
Temp. (ºC)	Max	170	n.a.	170	172	170	178	n.a.
	Min	170	80 set up	170	170	170	170	170 set up
Height (mm)		146.37	146.37	106.98	106.98	146.37	146.37	108.00
Powder addition	kg	8 before	4 during	0	0	4 b + 4 d	4 during	0
	Nr.	0	0	3	4	0	0	1

Build								
Nr.		57	58	68	78	80	81	90
Picture								
Parameters								
Laser Strategy		Stripe	Stripe	Stripe	Stripe	Stripe	Stripe	Stripe
Thickness (µm)		Sp:60 B:30	30	60	60	60	60	60
Layer Time (min)	Max	2.180	0.384	0.550	0.209	0.830	0.374	0.528
	Min	0.126	0.153	0.200	0.156	0.373	0.195	0.116
Build T (hh:mm)		27:14	12:08	10:30	10:03	21:57	17:04	09:29
Temp. (ºC)	Max	170	170	170	95	176	134	144
	Min	170	170	170	95	95	95	95
Height (mm)		106.98	178.83	117.54	109.98	267.78	283.62	222.00
Powder addition	kg	0	12 before	0	0	24 during	8 during	8 before
	Nr.	2	0	1*	4	0	0	0

During each build (Table 3.1), which could have one or more parts, six vertical tensile test specimens were produced. In order to compare the powder quality in between builds, all the specimens were built with the same parameters, unless an oversight occurs: layer thickness: 60 µm, laser strategy: stripe and single laser, as the variable under investigation is the powder. Exceptions occurred in builds 35 and 41, where only four and three tensile test specimens, respectively, were produced using the same parameters as the corresponding part at different build platform temperature, layer thickness or laser strategy in order to understand the influence of such parameters in the part quality. In builds 47 and 48, in addition to the six specimens intended for powder quality assessment, four additional tensile test specimens were manufactured using the specific parameters of each build; these specimens are designated as 47C and 48C, as they follow the parameters applied to the crankcase. Therefore, in these two builds, two types of specimens were produced: 47P and 48P (P for powder), manufactured with standard parameters to evaluate powder quality, and 47C and 48C (C for crankcase), manufactured to assess the influence of the modified parameters in those builds. From build 78 and all subsequent, only five specimens were produced, and the build platform temperature was adjusted to 95 °C to comply with the maximum value recommended by standard ASTM F3318, while maintaining the layer thickness (60 µm) and laser scanning strategy (stripe and single laser). The powder used was from supplier 1, unless when powder 4 (recycled) was introduced for the first time in build 65, and continued to be used in builds 67, 70, 72 and 73. In build 90 two specimen

were produced one on top of the other (90B – bottom and 90T – top).

All specimens were produced according to the technical drawing shown in Figure 3.8.

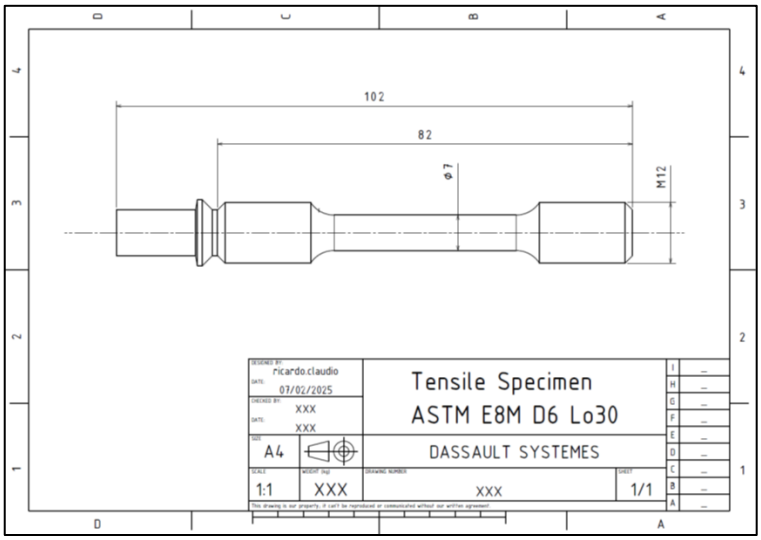

Figure 3.8 – Specimen technical draw.

One specimen from builds 35, 41, 45, 47, and 48, was heat-treated in Ceratherm FM furnace at 280 ºC for 2h at LAUAK Setúbal and cooled in the air. Of builds 68, 78, and 81 two specimen were heat-treated in LAUAK Hasparen, France, with the same procedure. This temperature was was chosen in order to be possible compare results with ASTM F3318 which defines 285 ± 14 ºC for 2 h ± 15 min as SR1 (Stress Relief 1), and the Renishaw procedure, which is 275 ºC, for 2 h.

Regarding powder sampling, samples of powder 1 were collected according to Table 3.2, and samples of powder 2 according to Table 3.3. Powders 3 and 4 (Figure 3.6) were also analysed and identified as powder 3 and powder 4, respectively.

Table 3.2 – Samples from powder 1.

Supplier	Lot	Sample
1	A	S1 Lot A
1	B	S1 Lot B
1	C	S1 Lot C
2	A	S2 Lot A
2	B	S2 Lot B
3	A	S3 Lot A
3	B	S3 Lot B

For this study, it is essential to assess the powder quality considering the number of builds performed since the last addition of fresh powder. This evaluation will determine the extent to which repeated reuse may influence the quality of the hopper powder (powder 2). Accordingly, Table 3.3 records the corresponding number of builds completed without the introduction of new powder.

Table 3.3 – Sample ID and Number of builds without adding new powder relationship.

Build	Sample ID	Powder addition	Number of builds from last powder addition
Before 45	45A	No	2
After 45	45B	No	3
After 46	46	No	4
After 47	47	Yes	0
After 48	48	Yes	0
After 51	51	No	1
After 57	57	No	2

Due to the high production volume of builds the maximum number of consecutive builds performed without powder replenishment was limited to only four.

It is not possible to remove powder directly from hopper, other for the following reasons:

- to open the hopper would expose the inside powder to air,

- the opening has a butterfly valve which prevents the insertion of a spatula or other tool to collect the powder.

So, in order to collect powder from hopper two different ways were used. The first one, used for sample 45A is a time- and argon-consuming method (listed in Appendix 2). After that, the next samples from hopper were taken from the powder remaining from the printing job, i.e. the unmolten powder that remains in the chamber.

To remove the powder from the chamber:

- an open sample vial is placed (with both openings facing upwards) when the powder removal tools are inserted in the chamber,

- purge the chamber with argon,

- raise the build platform to its initial level,

- drag the powder into the sample vial with a spatula,

- close the sample vial,

- remove the sample vial after debuild the part.

From now on the powder 2 (from hopper) will be removed as mentioned above.

The collected powder samples were analysed for particle size distribution, chemical composition, morphology, and flowability. Characteristic density measurements will not be performed due to the lack of opportunity.

3.4. Powder Characterisation

3.4.1. Particle Size Distribution

Particle size is considered to be a useful property for comparing and controlling different lots of powder over time as this characteristic will change with powder use. (ISO/ASTM 52907:2019)

According to ISO/ASTM 52907:2019 particle size and particle size distribution shall be determined in accordance with one or several of the methods and standards listed in Table A3.1 from Appendix 3.

The analyses were carried out by dynamic image analysis in accordance with ISO 13322-2 standard at *Instituto de Soldadura e Qualidade* (ISQ) with a CamSizer X2 MICROTRAC. The technique used was dry, pressurized air dispersion, and for each sample were performed three measurements.

3.4.2. Chemical Composition

Chemical analyses are carried out on the powder used in the additive manufacturing process in order to assess its quality. The chemical composition of the metallic shall be determined by suitable testing procedure, e. g. wet chemical process, atomic absorption spectrometry, flame emission spectroscopy, or X-ray fluorescence analysis (ISO/ASTM 52907:2019, 2019).

In this work the chemical composition is determined using X-ray fluorescence analysis at SEM in a XRF, Hitachi X-MET8000 and local analysis with energy dispersive spectroscopy (EDS, Bruker XFlash 730M) detector in the Scanning Electron Microscope (SEM, Hitachi SU3900).

3.4.3. Morphology

Powder morphology is considered to be a useful property for comparing and controlling different lots of powders over time (ISO/ASTM 52907:2019, 2019).

Powder morphology is strongly linked to the process used to produce the powder; as stated and illustrated in EN 1274. Particle morphology shall be described using the vocabulary defined in ISO 3252 or ASTM B243 (ISO/ASTM 52907:2019, 2019).

The powder samples were analysed in a Scanning Electron Microscope Hitachi SU3900 at ISQ facilities.

3.4.4. Flowability

Powder flowability refers to a powder's ability to move when subjected to force. This force may come from gravity, vibration, air pressure, or mechanical feeding.

Flowability should be determined using one of the methods specified below:

- ISO 4490 or ASTM B213 (results reported in s/50g),
- ASTM B964 using a Carney funnel (results reported in s/150 g or s/200 g),
- ISO 13517 using Gustavsson funnel (results reported in s/50g),
- ISO 4324 (ISO/ASTM 52907:2019, 2019).

The flowability test report shall include the initial powder condition, i. e. stationary or moving powder (ISO/ASTM 52907:2019, 2019).

In this study a Granuflow from Granutools was used at ISQ facilities where the initial powder condition was stationary. This device follows the ISO 4490 and ASTM B213 standards "Flow through an orifice". In this work the considered orifices were 1.0; 1.5; 2.0; 2.5; 3.0; 3.5; and 4.0 mm diameter.

3.5. Specimens Characterisation

3.5.1. Relative Density

EN 6018 (2017) defines the determination of density according to displacement method for metallic materials. According to this European Standard the liquid test could be distilled water or any other suitable liquid which may contain up to 0.1 % wetting agent to prevent the appearance of air bubbles. The balance should have a maximum permissible error of 0.0001 g. Suspended on a thin wire (maximum diameter 0.125 mm), the sample is weighed in air (m_1), immersed into the test liquid and again weighed (m_2), taking care that no air bubbles adhere to the sample.

The specimens were immersed in propanone and subjected to ultrasonic cleaning for approximately 15 minutes to remove any residual powder adhering to their surfaces. They were then dried using a hot air dryer. The specimens were placed on the balance for weighing only after cooling.

At *Instituto Politécnico de Setúbal* (IPS) facilities a Kern ADJ analytical balance was used with the density determination kit, as shown in Figure 3.9. Propan-2-ol was used as test liquid.

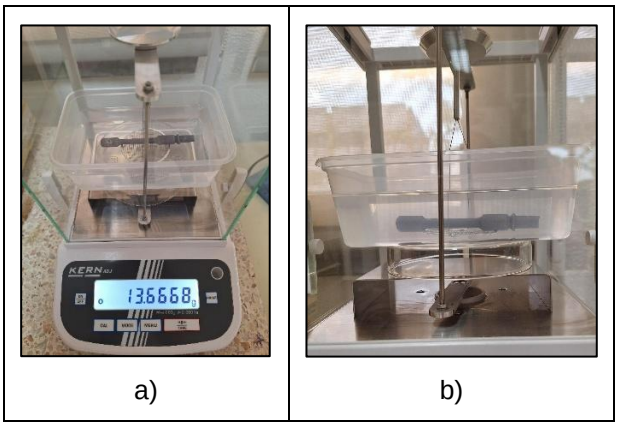

a) b)

Figure 3.9 – a) Analytical balance with the density determination kit, and b) side view confirming total immersion of the test piece without touching the bottom or sides of the container.

The density of the test liquid (ρ_F) is determined by means of the aerometer and is to be checked prior to each measurement. The density (ρ) measured in (kg/dm^3) is calculated according to the following equation:

$$\rho = \frac{m_1 \times \rho_F}{m_1 - m_2} \tag{3.1}$$

where:

m_1 - mass of the sample weighed in air (kg), m_2 - mass of the sample reduced by the mass of displacement liquid (weighing the sample in the liquid) (kg), ρ_F - density of test liquid (kg/dm^3), ρ - density of weighed sample (kg/dm^3).

3.5.2. Tensile Test

The tensile test is used to evaluate the strength and stiffness of metals and alloys among other properties. In this test, a metal sample is pulled to failure in a relatively short time at a constant rate. The force (load) on the specimen being tested is measured by the load cell, while the strain is obtained from the extensometer attached to the specimen, and the data is collected in a computer-controlled software package (Smith et al., 2019).

ASTM International E8/E8M (2022) covers the tension testing of metallic materials in any form at room temperature, specifically, the methods of determination of yield strength, yield point elongation, tensile strength, elongation, and reduction of area.

Before tensile testing the specimens were machined according to (ASTM International E8/E8M, 2022) and (ASTM International F2971, 2013) standards for subsequent tensile testing. Figure 3.10 shows two specimens a) as-built, and b) machined.

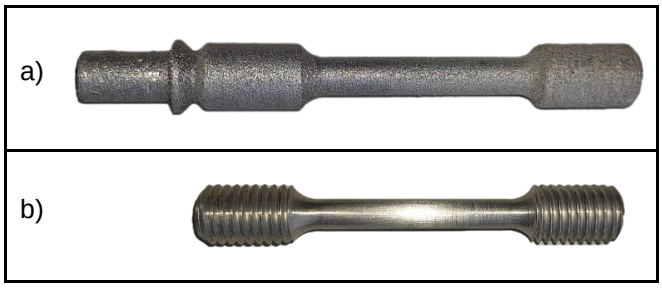

Figure 3.10 – Specimen a) as-built, and b) machined.

The first set of specimens being analysed, were samples corresponding to the builds, 35, 41, 45, 46, 47, 48, and 51. These specimens were machined at LAUAK Setúbal and the tensile test were performed at IPS. The equipment used at IPS facilities to perform the tensile tests was an Instron with a 25-ton load cell, using a 25 mm clip gauge, with 0.009 mm/s traction speed, as shown in Figure 3.11. Before testing, the specimen diameter was measured in five different places along the reduced parallel section. In this set, three as-built specimens for each build, and one heat-treated sample from each builds with exception of builds 46 and 51, were tested.

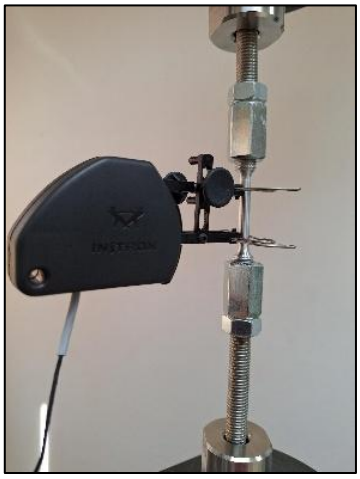
Figure 3.11 – Specimen with the clip gauge for the tensile test.

The second set of specimens (58, 68, 81 and 82) were machined and tested in France. The tests were performed in two as-build and two heat-treated. The tensile testes from this second set were performed at *Laboratoire ECCI*, a Nadcap certified laboratory.

A third set of specimens (57, 58, and 80) was machined and subsequently tested at IPS. The tensile tests were performed using E series equipment.

3.5.4. Hardness

Hardness is a measure of the resistance of a metal to permanent (plastic) deformation. The hardness of a metal is measured by forcing an indenter into its surface. The indenter material,

which is usually a ball, pyramid, or cone, is made of a material much harder than the material being tested. (Smith et al., 2019)

The hardness of a metal depends on the ease with which it plastically deforms. Thus, a relationship between hardness and strength for a particular metal can be determined empirically. The hardness test is much simpler than the tensile test and can be non-destructive (i.e., the small indentation of the indenter may not be detrimental to the use of an object). For these reasons, the hardness test is used extensively in industry for quality control. (Smith et al., 2019)

In order to perform the hardness tests, the specimens were placed in a tailored Polylactic Acid (PLA) container, which was then filled with resin. The resin used was Epoxy Resin Epo Thin® 2 from Buehler mixed with Epoxy Hardener Epo Thin® 2 also from Buehler, in 10:4 (V/V) proportion, respectively. After three days of curing, the specimens were cut lengthwise using a circular saw, see Figure 3.12.

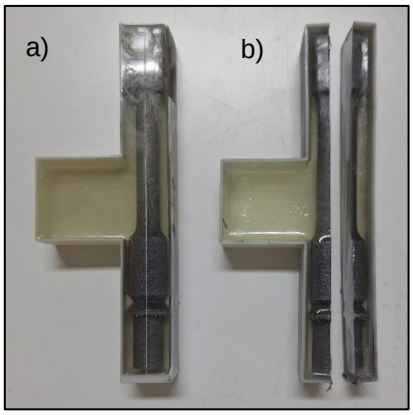

Figure 3.12 – a) Specimen placed in a tailored PLA container filled with resin, and b) Specimen cut lengthwise.

After that, half of the sample was sanded manually, under water, with 600, 800, 1000, 1200 and 2500 grit sandpaper, rotating 90º at each grit size, polished with colloidal silica and lubricant, washed with water and propanone and finally dried.

The polished halves of the various samples were marked every 10 mm, only on the edge of the resin, as shown in the Figure 3.13.

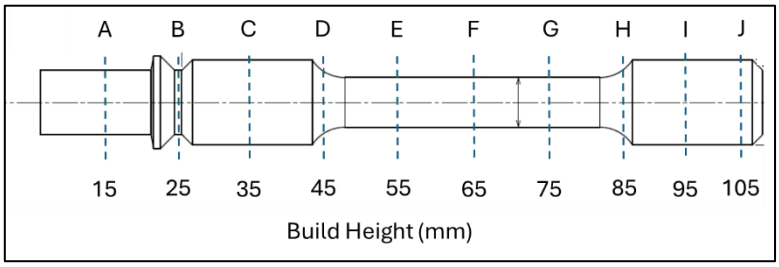

Figure 3.13 – Scheme of the specimen marked every 10 mm.

Three measurements were taken along each mark, corresponding to each build height. 1 kgf was loaded into the sample by a Innovatest Falcon 450 Vickers Hardness Tester from IPS (Figure 3.14).

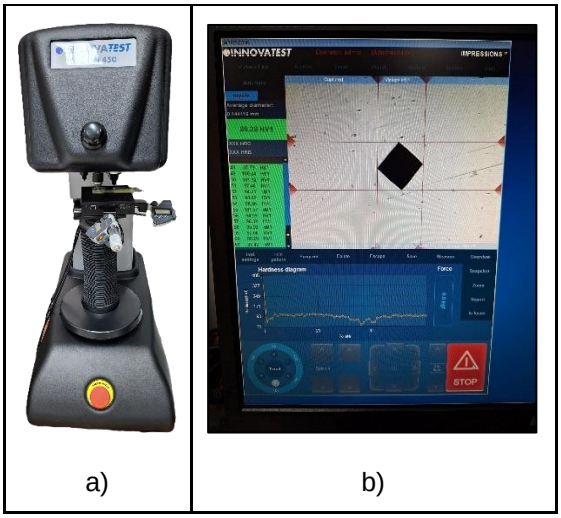

a) b)

Figure 3.14 – a) Falcon 450 Hardness Tester, and b) Vickers Hardness measurement.

3.5.5. Microstructure

Optical microscopy was performed in a Leica equipment at IPS facilities to analyse the defects in the cut specimens studied with a magnification of 50x.

To elucidate the hardness results obtained, the microstructures of selected specimens were examined. Following the hardness testing, the samples were etched using Keller's reagent (2 ml HF : 3 ml HCl : 5 ml HNO_3 in 190 ml distilled H_2O) for 30 seconds to reveal their microstructural features, as described in literature (De Seabra, 1995),(Mertens et al., 2020), (Merino et al., 2021), (Bogdanova et al., 2024). The analysis was conducted with a Phenom Desktop Scanning Electron Microscope (SEM) at IPS.

Chapter 4

Results

This chapter presents the results obtained from various tests, including particle size distribution, chemical composition, morphology, flowability, density, tensile test, hardness, and microstructure.

The quality of the feedstock was analysed, as well as the specimens produced during the manufacture of a part. The results of the various samples are shown below.

4.1. Powder Characterisation

4.1.1. Particle Size Distribution

Regarding the particle size distribution of the different types of powders, the results of x_{area} distribution obtained will be shown below. To ensure clarity and avoid loss of information, the data will not be displaced in a single graph. Figure 4.1 illustrates the comparison among powder 1 samples, which include multiple lots from different suppliers. The samples are identified as reported previously in Table 3.2: supplier 1 (S1), Lot A, B and C; supplier 2 (S2) Lot A and B, and supplier 3 (S3) Lot A and B.

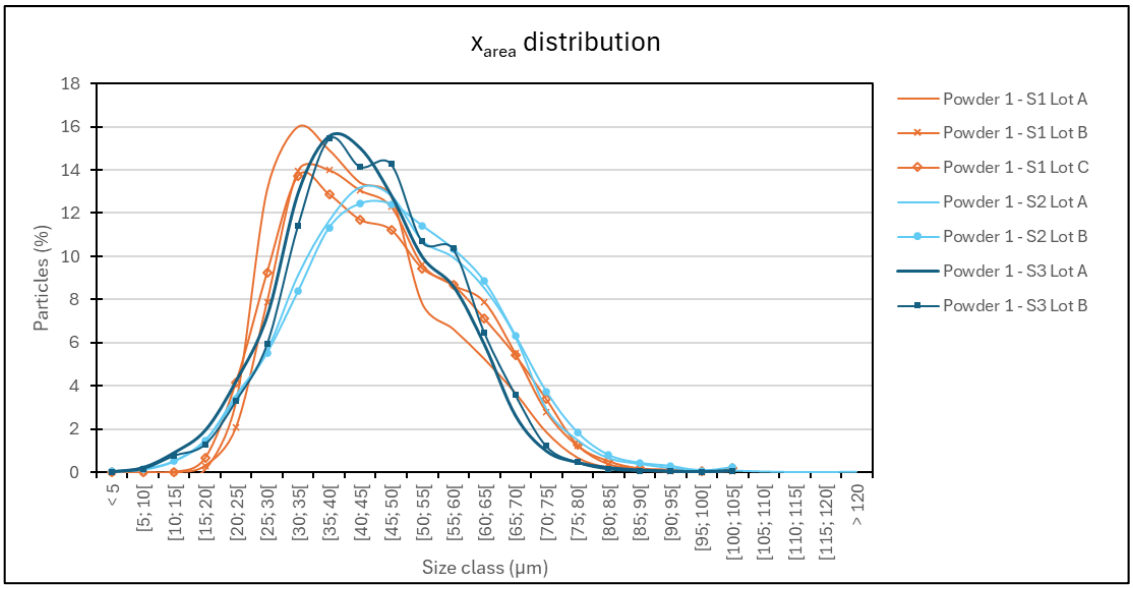

Figure 4.1 – x_{area} distribution of particles size from powders 1.

Figure 4.2 may better illustrate the difference in x_{area} distribution than Figure 4.1.

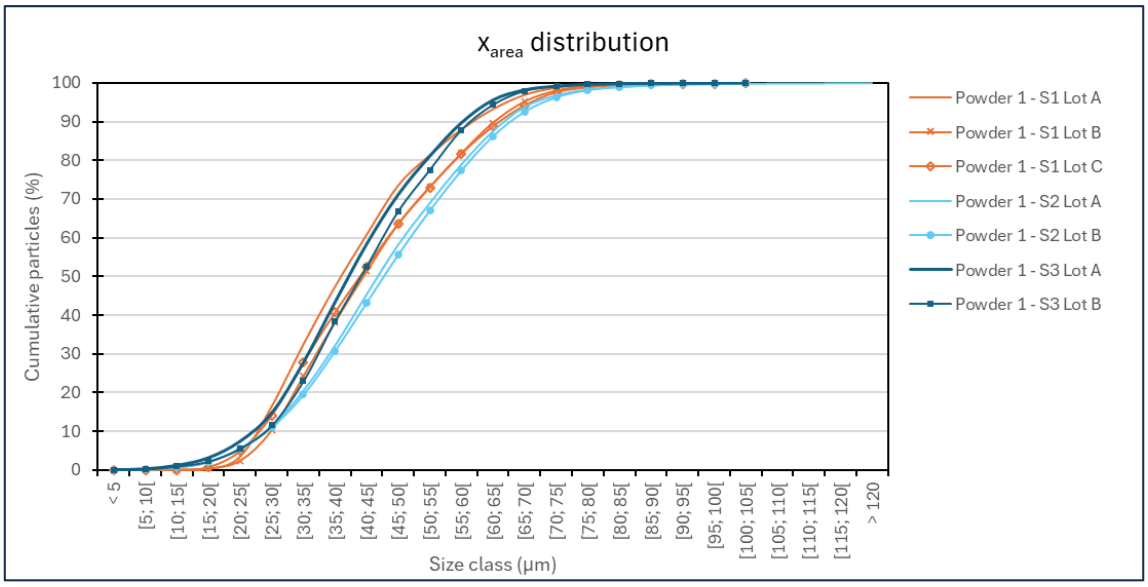

Figure 4.2 – Cumulative x_{area} distribution for powder 1.

D10, D50 and D90 are usually referred to as the maximum size corresponding to 10%, 50% and 90% of the particles, respectively. Table 4.1 shows the D10, D50 and D90 values for the various samples of powder 1 under study.

Table 4.1 – D10, D50, and D90 for the different powders 1.

Powder	D10 (µm)	D50 (µm)	D90 (µm)
S1 Lot A	25	40	60
S1 Lot B	30	45	65
S1 Lot C	30	45	65
S2 Lot A	30	45	70
S2 Lot B	30	50	70
S3 Lot A	25	45	60
S3 Lot B	30	45	60

As can be seen from Figure 4.1, S2 powder has a more homogeneous and consistent particle size distribution. S1 and S3 have a higher percentage of particles smaller than 65 µm, as can be confirmed by the data in Table 4.1, Figure 4.1 and Figure 4.2.

The results for powder 2 are presented next. Figure 4.3 displays a comparison of the powder collected from three consecutive builds, during which no fresh powder was introduced. In this case, the powder only recirculated within the machine.

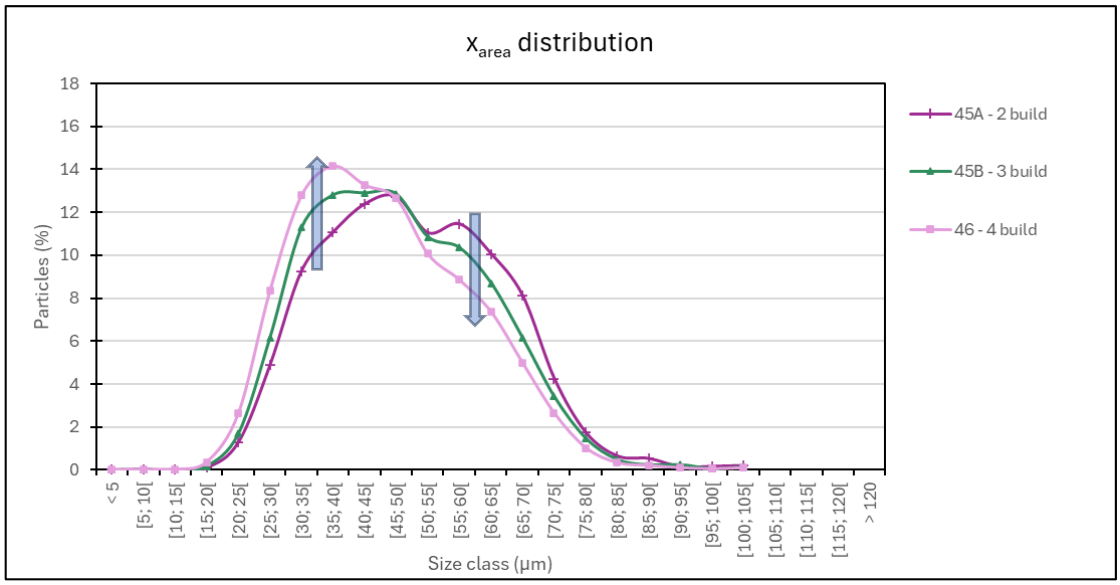

Figure 4.3 – Comparison in between powder 2 from consecutive builds, 45A, 45B, and 46.

Figure 4.3 compares powder samples taken before build 45 (45A), after 45 (45B), and after 46. As explained before in Table 3.3, when sample 45A was collected, there were two builds to which the latest new powder had been added. After build 46, there were four builds without any new powder added.

A decrease in percentage of larger particles leading to an increase in smaller particles can be clearly seen as the powder recirculates in the machine. The same behaviour is shown in Figure 4.4 when powder from builds 47, 48 and 51 are compared.

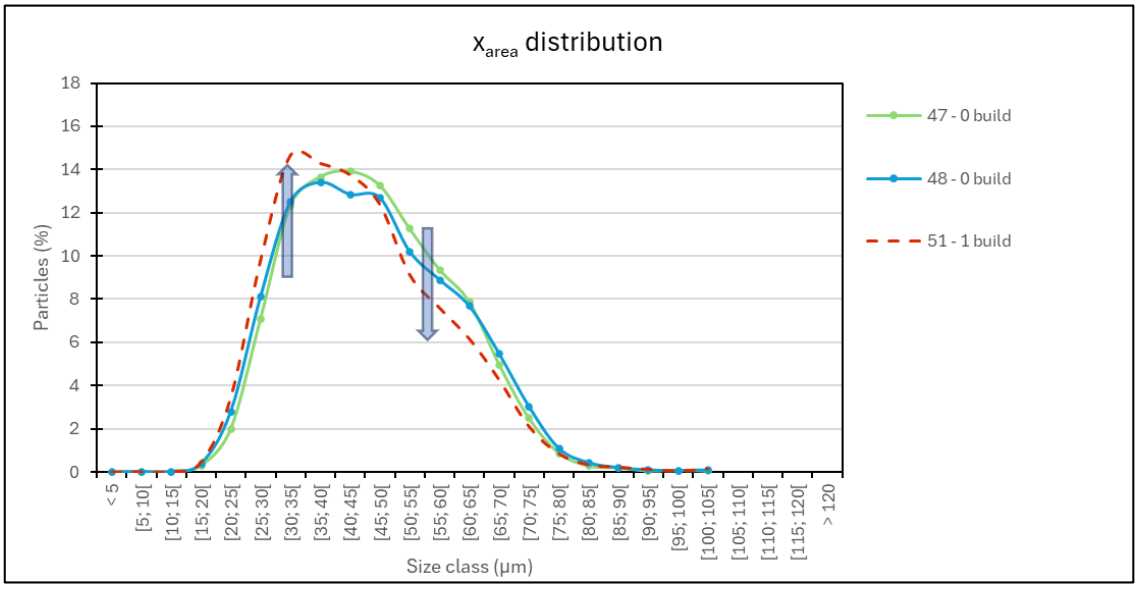

Figure 4.4 – Comparison between powder 2 from builds 47, 48 and 51.

Figure 4.5 shows the cumulative x_{area} distribution for powder 2.

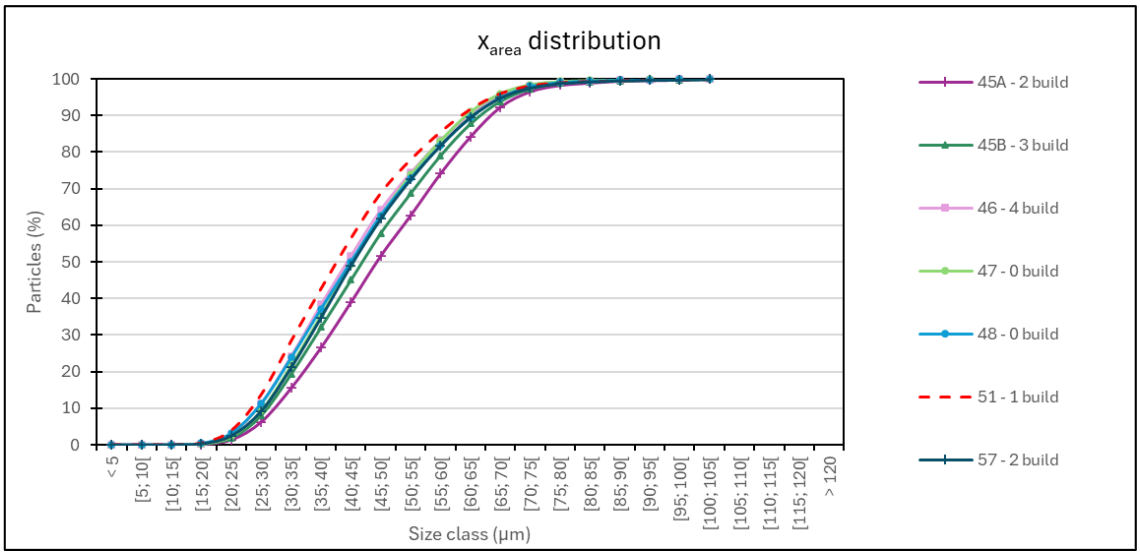

Figure 4.5 - Cumulative x_{area} distribution for powder 2.

Figure 4.5 reveals a leftward shift in the curves corresponding to consecutive builds, indicating a reduction in the particle size of the correspondent powder.

Table 4.2 - D10, D50, and D90 for the different powders 2.

Powder	D10 (µm)	D50 (µm)	D90 (µm)
45A	30	50	70
45B	30	45	65
46	30	45	65
47	30	45	65
48	30	45	65
51	25	40	60
57	30	45	65

Finally, Figure 4.6 compares powders 1, 3 and 4.

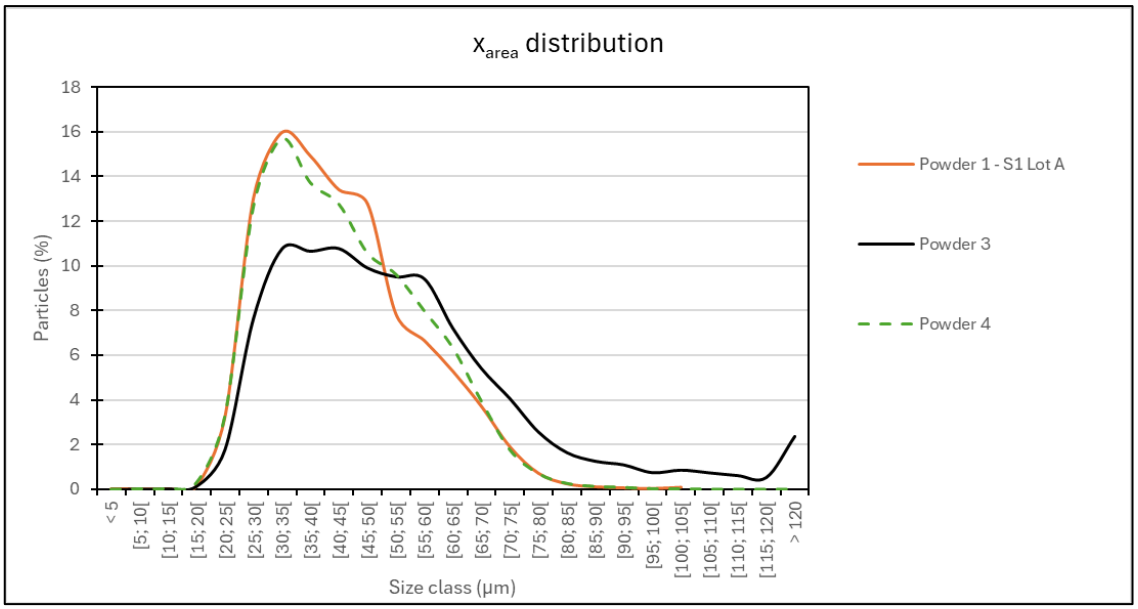

Figure 4.6 – Comparison between powder 1, 3 and 4.

As illustrated in Figure 4.6, powder 3 was sieved efficiently, resulting in powder 4 which exhibits a particle size distribution ranging from 15 µm to 85 µm, similar to that of powder 1. The green (powder 4) and orange (powder 1) curves overlap below 30 µm and above 70 µm. Powder 3 (cyclone not sieved), on the other hand, shows a significant number of particles above 65 µm. As can be seen in Figure 4.7, the percentage of particles above 65 µm is about 20 %.

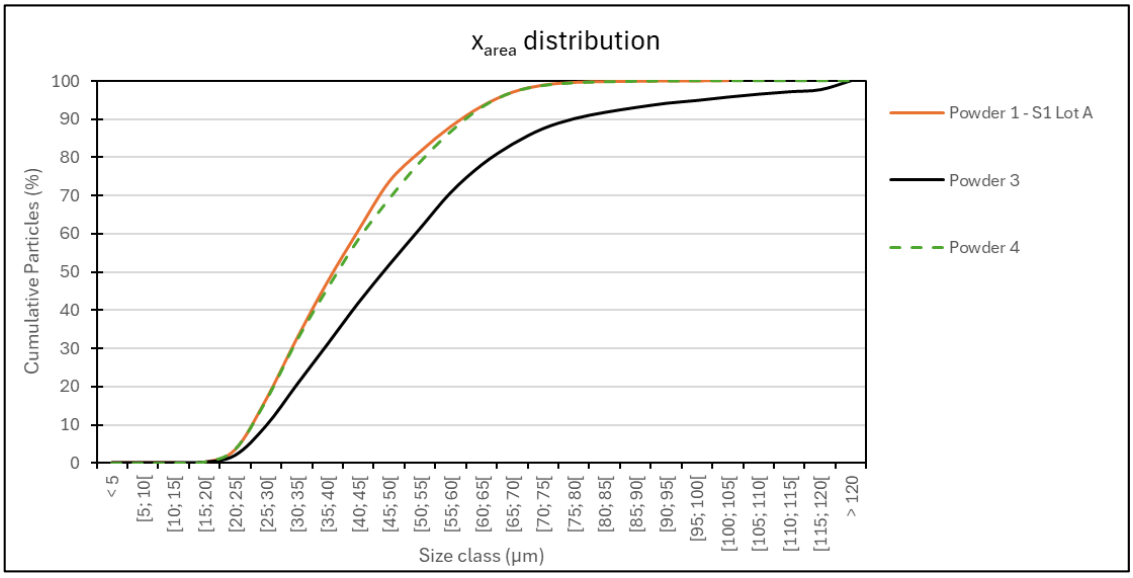

Figure 4.7 – Cumulative particle percentage of x_{area} distribution for powder 1, 3 and 4.

Table 4.3 - D10, D50, and D90 for the powders 1 (S1 Lot A), 3 and 4.

Powder	D10 (µm)	D50 (µm)	D90 (µm)
S1 Lot A	25	40	60
3	30	50	80
4	25	40	60

As previously mentioned, the cyclone powder, once filtered, exhibits the same characteristics in terms of particle size distribution as the new powder.

4.1.2. Chemical Composition

The chemical composition of the powders under study was analysed by X-ray fluorescence. The chemical elements analysed were aluminium (Al), silicon (Si), magnesium (Mg), iron (Fe), copper (Cu), manganese (Mn), titanium (Ti), zinc (Zn), tin (Sn), lead (Pb), oxygen (O), nitrogen (N) and carbon (C). The results obtained for S1 Lot C (powder 1) are shown in Figure 4.8.

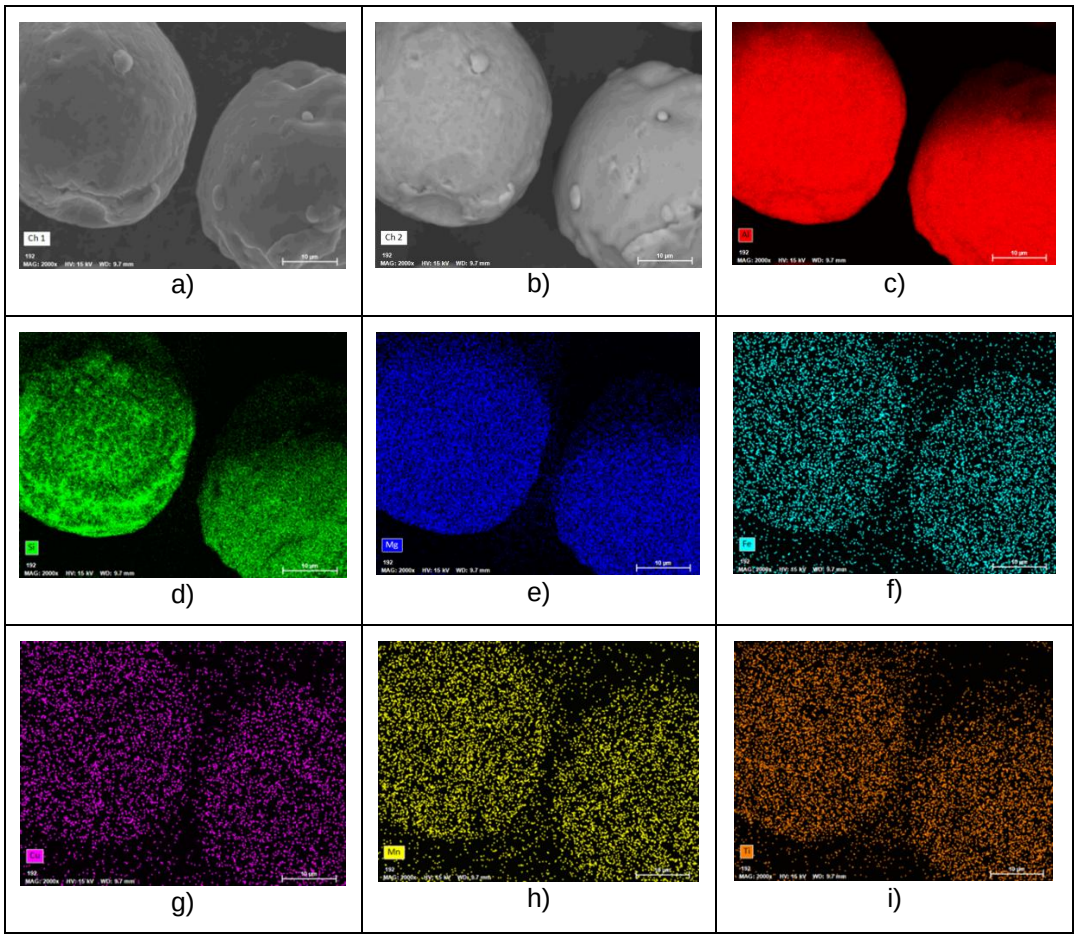

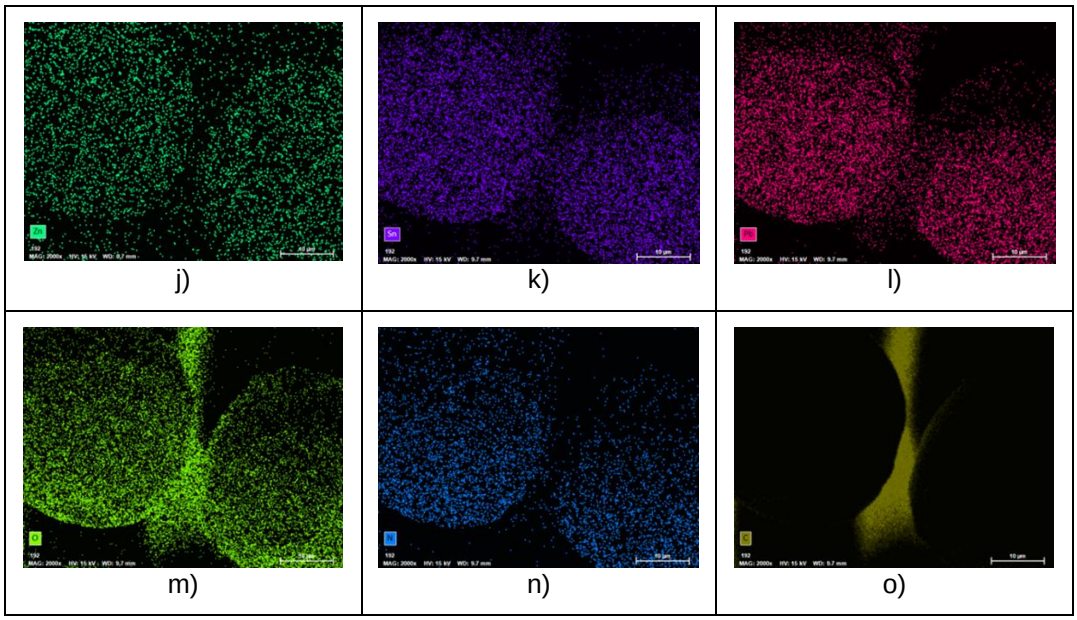

Figure 4.8 – SEM Images 2000x magnification from powder 1 S1 Lot C. a) SE, b) BSE, c) Al, d) Si; e) Mg, f) Fe, g) Cu, h) Mn, i) Ti, j) Zn, k) Sn, l) Pb, m) O, n) N and o) C.

It is perfectly clear from the SEM images on Figure 4.8 that some elements are in such low concentration that noise is noticeable, for example: Fe, Cu, Mn, Ti, or Zn, and that the results obtained for the elements C, N, and O are not reliable. As reported previously in Chapter 2, X-ray fluorescence spectroscopy does not allow for accurate quantification of elements with atomic numbers below ten; therefore, the analysis will not be carried out on these elements. For quantitative analysis, specific regions of the sample are delineated, as illustrated in Figure 4.9.

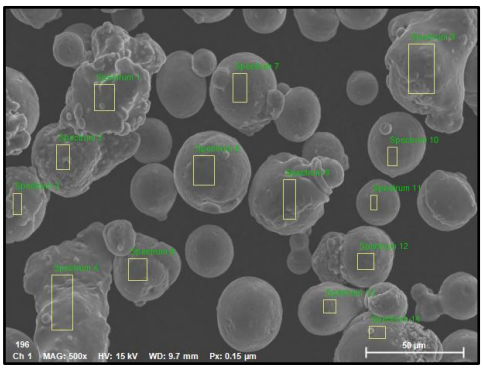

Figure 4.9 – SEM Image 500x magnification from powder 1 S1 Lot C whit the selected regions for X-ray fluorescence analysis.

The results obtained from the regions shown in Figure 4.9 were statistically processed, outliers were eliminated using interquartile range (IQR). The entire process was repeated for different magnifications and samples. The mean values of all regions studied for S1 Lot B, S1 Lot C, S2 Lot B and S3 Lot A (powder 1) samples are presented in Table 4.4 in comparison with

ASTM F3318 recommended values for the final part. Values highlighted in red indicate mean values that fall outside the recommended range, whereas those highlighted in orange may deviate from the expected range depending on the associated standard deviation.

Table 4.4 – Chemical composition of powder 1 from different suppliers and ASTM F3318 recommended values for the final part.

	Chemical Composition % (w/w)				
Element	**ASTM F3318**	**S1 Lot B**	**S1 Lot C**	**S2 Lot B**	**S3 Lot A**
Al	Balance	Balance	Balance	Balance	Balance
Cu	≤ 0.05	**0.06 ± 0.06**	**0.06 ± 0.07**	**0.02 ± 0.04**	**0.03 ± 0.04**
Fe	≤ 0.55	0.20 ± 0.06	0.17 ± 0.05	0.20 ± 0.07	0.18 ± 0.07
Mg	[0.20; 0.45]	**0.47 ± 0.09**	**0.45 ± 0.12**	0.36 ± 0.08	**0.46 ± 0.12**
Mn	≤ 0.45	0.01 ± 0.02	0.02 ± 0.03	0.00 ± 0.01	0.02 ± 0.02
Pb	≤ 0.05	0.01 ± 0.02	**0.03 ± 0.03**	0.02 ± 0.02	**0.03 ± 0.04**
Si	[9; 11]	**11.50 ± 1.65**	**10.66 ± 1.16**	**11.50 ± 1.67**	**11.83 ± 1.27**
Sn	≤ 0.05	**0.03 ± 0.04**	**0.03 ± 0.04**	**0.03 ± 0.03**	0.00 ± 0.01
Ti	≤ 0.15	0.00 ± 0.00	0.02 ± 0.02	0.03 ± 0.03	0.01 ± 0.01
Zn	≤ 0.10	0.04 ± 0.05	0.03 ± 0.05	0.01 ± 0.01	0.01 ± 0.03

According to the results obtained for chemical composition, it appears that suppliers 1 and 3 generally have a magnesium percentage above the recommended level (0.45%), with supplier 2 being the only one within the values specified in the ASTM standard for this element. Silicon percentage is above the ASTM standard for the three suppliers, nevertheless Lot C from supplier 1 is closer within the range. Concerning copper percentage, supplier 1 samples are above the ASTM limit. Lead percentage for supplier 3 and Lot C from supplier 1 could be above the ASTM standard recommendation, the same happens to tin for samples from supplier 1 and 2. All the other elements are in range with ASTM F3318 standard.

The results corresponding to the samples produced with powder 2 are presented in Table 4.5. Values highlighted in red indicate mean values that fall outside the recommended range, whereas those highlighted in orange may deviate from the expected range depending on the associated standard deviation.

Table 4.5 – Chemical composition % (w/w) of powder 2 from samples 45A, 45B, 46, 47, 48, 51, and 57, and comparison with ASTM F3318 recommended values for the final part.

	Chemical Composition % (w/w)							
Element	**ASTM F3318**	**45A**	**45B**	**46**	**47**	**48**	**51**	**57**
Al	Balance	Balance	Balance	Balance	Balance	Balance	Balance	Balance
Cu	≤ 0.05	**0.04 ± 0.04**	0.02 ± 0.02	**0.05 ± 0.05**	0.02 ± 0.03	**0.06 ± 0.07**	**0.05 ± 0.06**	**0.03 ± 0.04**
Fe	≤ 0.55	0.18 ± 0.07	0.17 ± 0.06	0.19 ± 0.08	0.16 ± 0.09	0.18 ± 0.06	0.12 ± 0.07	0.18 ± 0.10
Mg	[0.20; 0.45]	**0.45 ± 0.12**	**0.45 ± 0.12**	**0.49 ± 0.11**	**0.46 ± 0.18**	**0.43 ± 0.11**	**0.52 ± 0.08**	**0.50 ± 0.11**
Mn	≤ 0.45	0.01 ± 0.01	0.02 ± 0.03	0.02 ± 0.03	0.02 ± 0.02	0.02 ± 0.03	0.00 ± 0.00	0.02 ± 0.03
Pb	≤ 0.05	0.01 ± 0.01	0.02 ± 0.03	0.02 ± 0.03	0.03 ± 0.03	0.02 ± 0.02	0.02 ± 0.03	0.02 ± 0.02
Si	[9; 11]	**9,73 ± 1.76**	**11.10 ± 1.86**	**10.81 ± 1.56**	**10.71 ± 2.23**	**10.75 ± 1.56**	**10.73 ± 1.52**	**11.56 ± 2.79**
Sn	≤ 0.05	0.02 ± 0.02	0.01 ± 0.02	0.02 ± 0.02	0.03 ± 0.04	0.01 ± 0.01	0.01 ± 0.01	0.01 ± 0.02
Ti	≤ 0.15	0.01 ± 0.02	0.01 ± 0.01	0.01 ± 0.01	0.01 ± 0.02	0.02 ± 0.02	0.01 ± 0.02	0.02 ± 0.03
Zn	≤ 0.10	0.00 ± 0.01	0.04 ± 0.05	0.03 ± 0.04	0.02 ± 0.04	0.03 ± 0.05	0.04 ± 0.05	0.01 ± 0.02

An analysis of the results presented in Table 4.5 indicates that magnesium is the element with the greatest difficulty in meeting the range established by ASTM F3318. This element may be present in excess in all samples, with its mean value clearly exceeding the recommended limit in samples 46, 47, 51, and 57. Silicon, although potentially outside the recommended range in all samples, may exceed the upper limit in samples 45B, 46, 48, and 51, whereas in the remaining samples it may lie either above or below the specified range, or within the expected interval.

Observing copper, the mean value for sample 48 lies above the limit recommended by the standard; however, considering the measurement's standard deviation, the actual value may fall within the range specified by ASTM F3318. For the remaining samples, their mean values do not exceed the recommended limit, although, given the measurement's standard deviation, the actual value may surpass the specified threshold, with the exception of samples 45B and 47.

Regarding the cyclone powders, not sieved and sieved, corresponding to powders 3 and 4 respectively, the chemical composition values obtained are presented in Table 4.6, where they are compared with powder 1 and with the reference values specified in ASTM F3318. Values highlighted in red indicate mean values that fall outside the recommended range, whereas those highlighted in orange may deviate from the expected range depending on the associated standard deviation.

Table 4.6 – Chemical composition % (w/w) of powder 1, 3 and 4, and comparison with ASTM F3318-18 values for the final part.

	Chemical Composition % (w/w)			
Element	**ASTM F3318**	**S1 Lot C**	**Powder 3**	**Powder 4**
Al	Balance	Balance	Balance	Balance
Cu	≤ 0.05	**0.06 ± 0.07**	**0.11 ± 0.01**	**0.13± 0.02**
Fe	≤ 0.55	0.17 ± 0.05	0.21 ± 0.01	0.17± 0.01
Mg	[0.20; 0.45]	**0.45 ± 0.12**	**0.78 ± 0.01**	**0.68 ± 0.01**
Mn	≤ 0.45	0.02 ± 0.03	-	-
Pb	≤ 0.05	**0.03 ± 0.03**	-	-
Si	[9; 11]	**10.66 ± 1.16**	**8.45 ± 0.05**	**8.13 ± 0.15**
Sn	≤ 0.05	**0.03 ± 0.04**	-	-
Ti	≤ 0.15	0.02 ± 0.02	-	-
Zn	≤ 0.10	0.03 ± 0.05	-	-

As shown in Table 4.6, powders 3 and 4 were not analysed for all the intended elements. Since the results are reported in weight percent, the fewer the elements included in the analysis, the more the reported values of the analysed elements are affected. Based on the obtained results, powders 3 and 4 exhibit a deficit of Si and an excess of Mg and Cu.

4.1.3. Morphology

As previously mentioned, several powder samples were analysed in a Scanning Electron Microscope Hitachi SU3900. In Figure 4.10 are compared 200x magnification images of different powder samples. From a) to e) are shown new powder from different suppliers (powder 1), from f) to j) are shown powder 2 samples, and k) is from powder 3 (cyclone not sieved), and l) powder 4 (cyclone sieved), as illustrated in Figure 3.6 in Chapter 3.

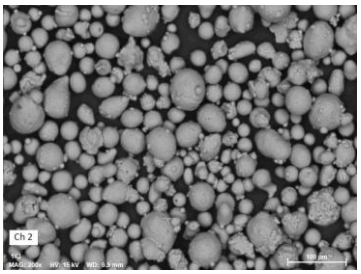

a) S1 Lot B

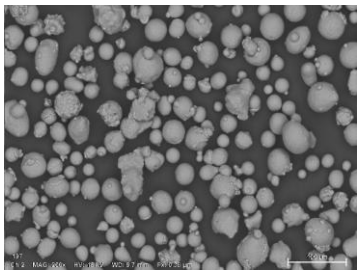

b) S1 Lot C

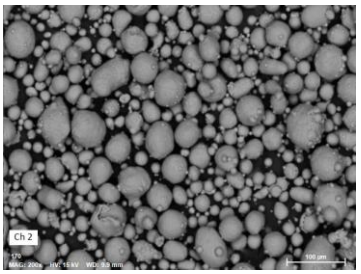

c) S2 Lot B

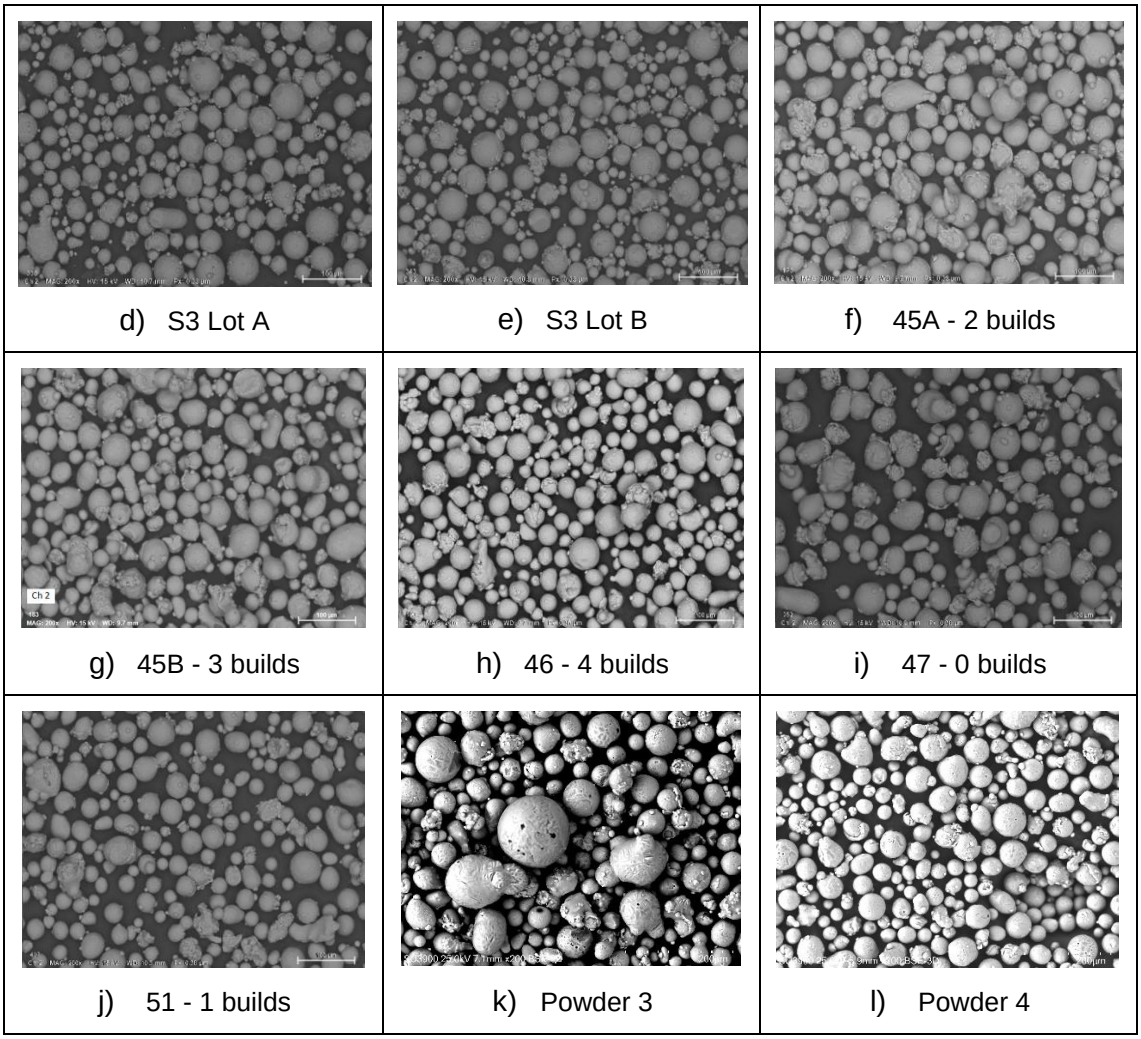

d) S3 Lot A | e) S3 Lot B | f) 45A - 2 builds

g) 45B - 3 builds | h) 46 - 4 builds | i) 47 - 0 builds

j) 51 - 1 builds | k) Powder 3 | l) Powder 4

Figure 4.10 – SEM images 200x magnification of AlSi10Mg powder 1: S1 Lot B, S1 Lot C, S2 Lot B, S3 Lot A, and S3 Lot B; powder 2: 45A, 45B, 46, 47,and 51, powder 3, and powder 4.

The SEM images of the various powders analysed and shown in Figure 4.10 reveal a largely similar morphology. Starting with a comparison of powder 1 images, a certain degree of uniformity can be observed among the samples analysed. For all suppliers, the particles are predominantly spheroidal, with some exhibiting splat caps, others elongated, many presenting satellites, and only a few showing irregular shapes. It is also evident that sample S2 Lot B displays a broader particle size distribution, characterized by a higher proportion of finer particles compared to suppliers 1 and 3, as well as a greater number of coarse particles.

When comparing powder 2 samples (45A, 45B, 46, 47, and 51), a similar morphology is observed across these samples, including elongated particles, particles with splat caps, and particles with satellites. Sample 51 additionally contains broken and agglomerated particles. Comparing powder 2 samples with S1 Lot C, since this lot was used in their production, reveals no significant morphological differences.

Regarding powder 3, a markedly higher number of particles with dimensions significantly

larger than those in any other sample is evident. This sample also exhibits numerous particles with porosity, satellites, and some fractured and agglomerated particles.

Finally, powder 4, which was externally sieved using a 63 µm sieve, shows a morphology more similar to that of powders 1 and 2, although some particles still display porosity.

4.1.4. Flowability

Concerning flowability, Figure 4.11 shows a comparison between samples from each of the suppliers studied.

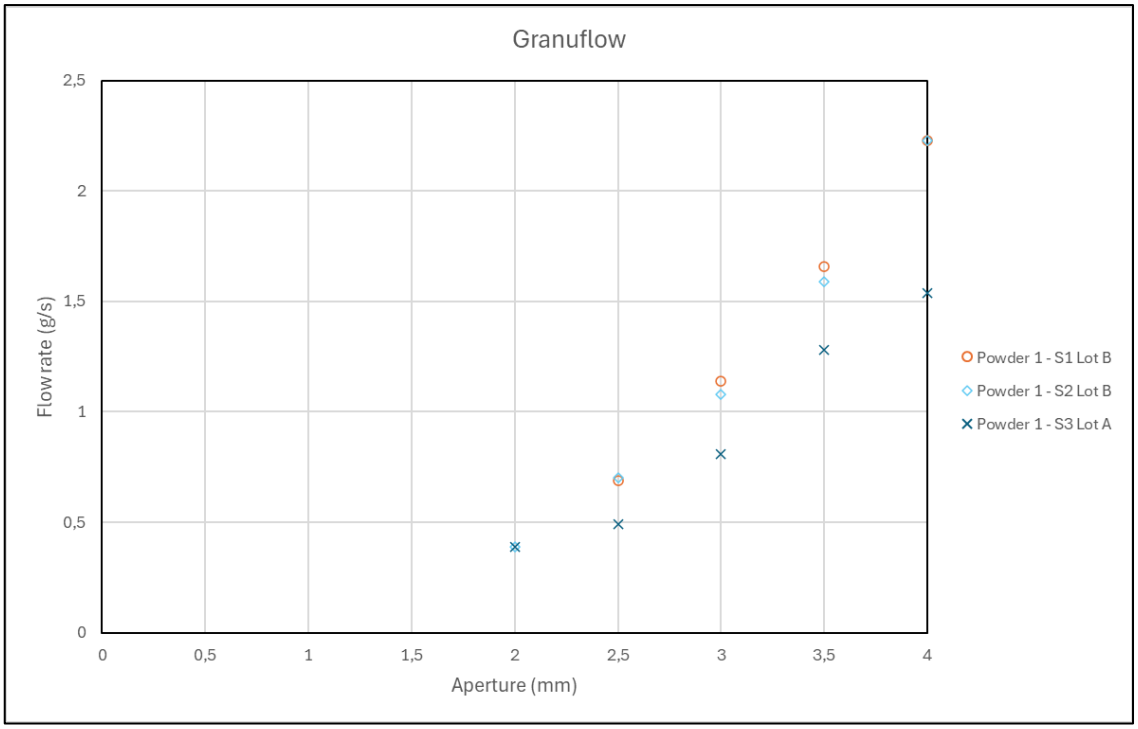

Figure 4.11 – Flowability from powder 1 samples.

Analysis of the results obtained in Figure 4.11 shows that the samples from suppliers 1 and 2 are very similar, while the sample from supplier 3 has lower flow rate values for the same opening than the other two samples.

A comparative analysis is presented below (Figure 4.12) between multiple powder 2 samples (45A, 45B, 46, 47, 48, 51 e 57) and a reference sample (S1 Lot B) obtained from the supplier.

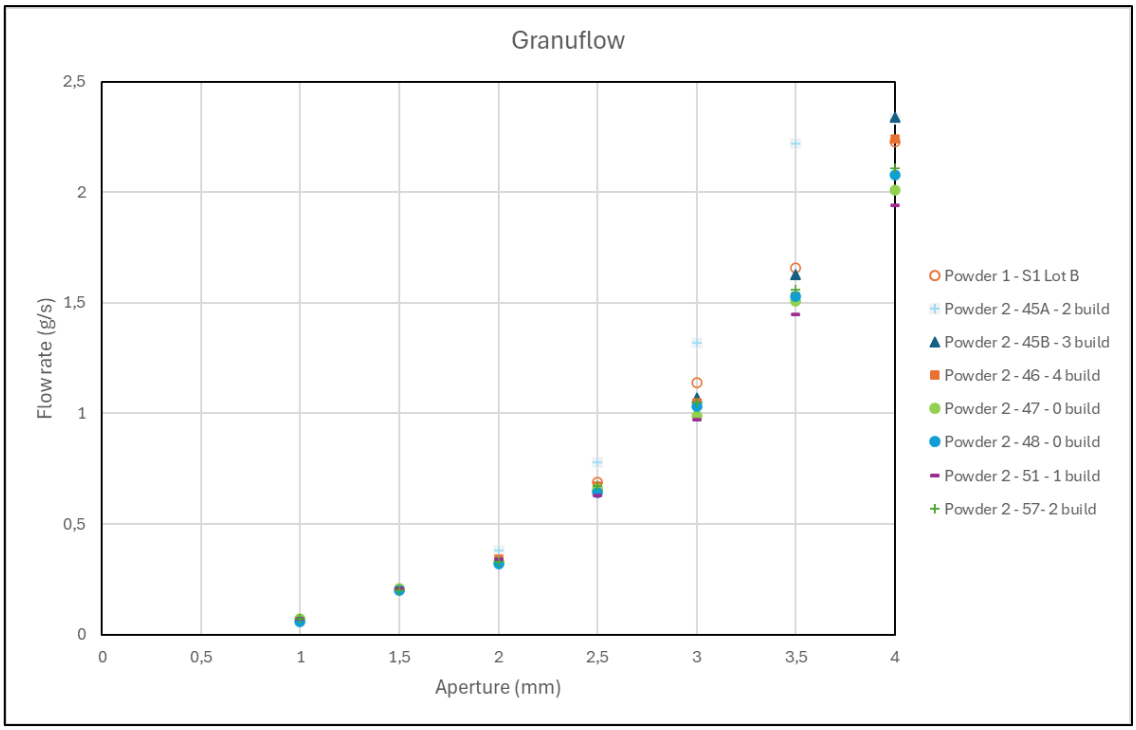

Figure 4.12 – Flow rate from powder 2 samples in comparison to a reference sample, powder 1 from supplier 1.

In this comparison (Figure 4.12), it can be seen that sample 45A stands out for having a higher flow rate than the other samples. It can also be seen that as the opening increases, the difference in flow rate between the samples also increases. For smaller diameter openings, such as 1 and 1,5 mm, there is no significant difference in the flow rate of the samples. However, from an opening of 2,5 mm onwards, the difference in flow rate between the samples becomes noticeable.

4.2. Specimens Characterisation

4.2.1. Relative Density

Due to the size of the samples, it was necessary to adapt the use of the density set-up, in order to the specimens were properly positioned, i.e., fully immersed and without touching the walls or bottom of the container. The relative density results of the specimens are shown in Table 4.7 in comparison with the standard value, which is 2,67 g/m^3. (Ghio & Cerri, 2022)

Table 4.7– Specimens Relative Density Values (%).

	Relative Density (%)								
Sample	**35**	**41**	**45**	**46**	**47C**	**47P**	**48C**	**48P**	**51**
AB	98.92	99.08	98.07	98.36	98.96	99.14	98.83	98.77	98.73
SR1	99.04	99.15	98.04	-	98.99	98.97	98.99	98.95	-
Sample	**57**	**58**	**68**	**78**	**80**	**81**	**82**	**90B**	**90T**
AB	97.72	98.78	98.36	99.02	98.55	98.64	98.60	98.73	98.52

4.2.2. Tensile Test

As an illustrative example, the figure presents a set of three tests corresponding to three builds: Tests 1 through 3 for builds 57, 58, and 80. These were the last specimens to be machined, and there was no opportunity for them to undergo heat treatment prior to the completion of this internship. Nevertheless, the study will continue afterwards.

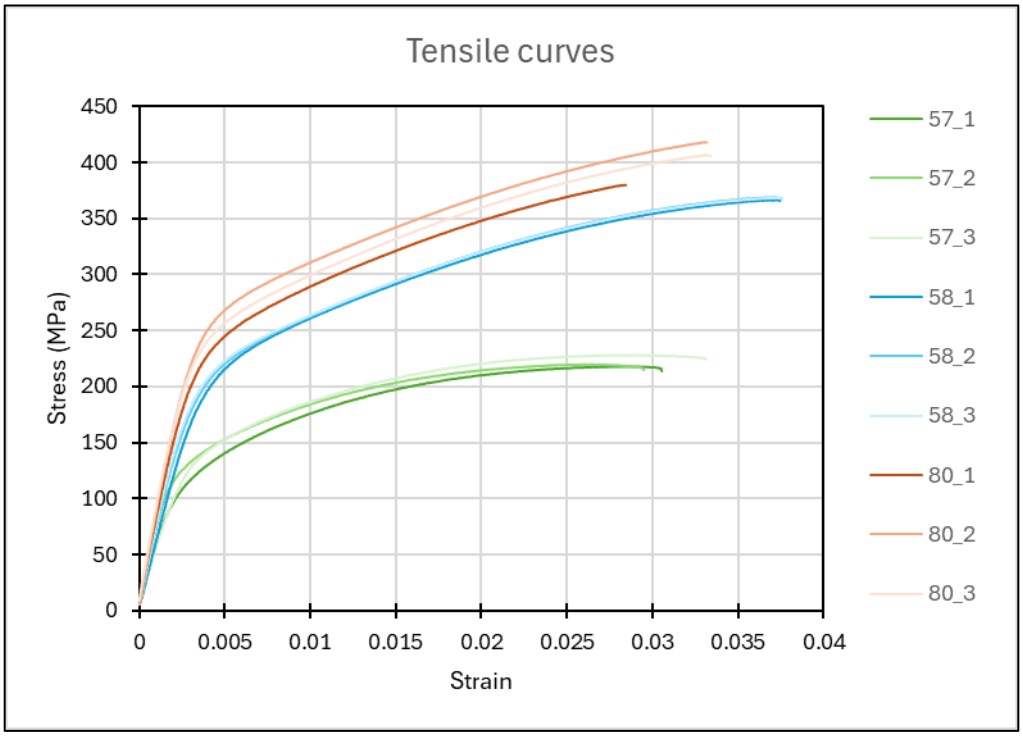

Figure 4.13 – Tensile curves for each sample of as-built 57, 58, and 80 builds.

As can be observed in Figure 4.13, the curves for each build are closely aligned within each test, with the exception of build 80, which exhibits greater dispersion among its curves (corresponding to a 16 MPa of standard deviation for the UTS values). After processing the results

for all samples analysed, the mean values for ultimate tensile strength (UTS) (Figure 4.14) and for yield strength (0.2 %) (Figure 4.15) are shown from non-heat treatment (NHT) and stress relief 1 (SR1) conditions in comparison with ASTM F3318 minimum values.

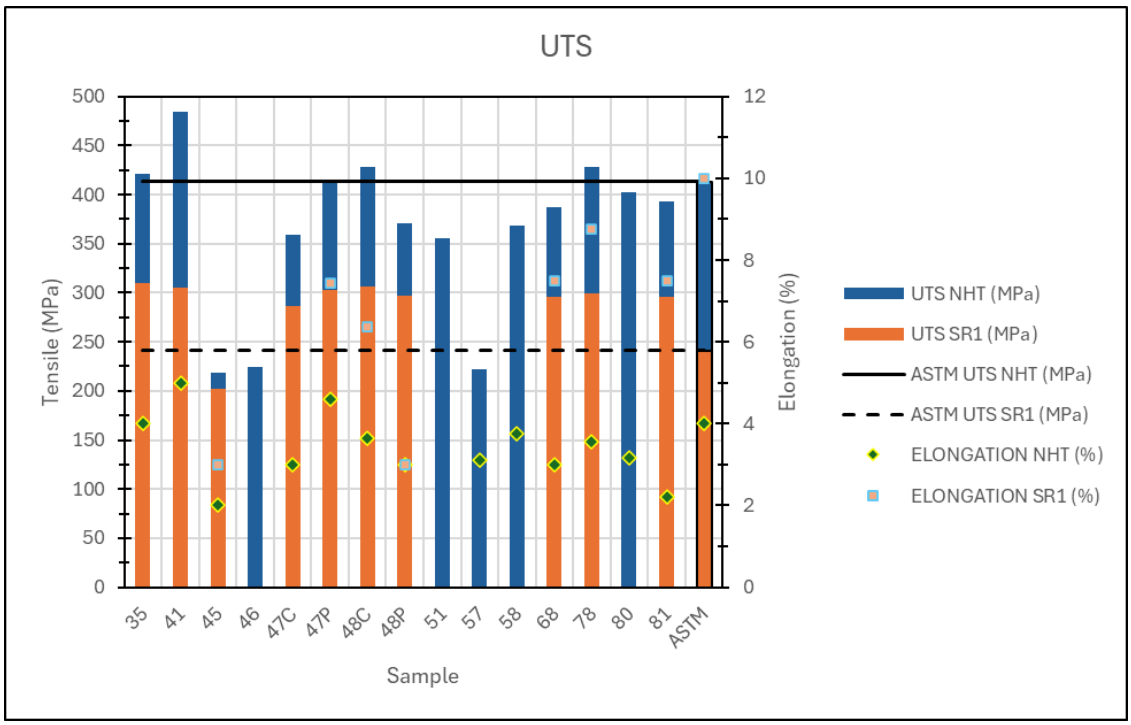

Figure 4.14 – UTS, and elongation results as-built (NHT) and after SR1 heat treatment for the studied specimens in comparison with ASTM 3318 values.

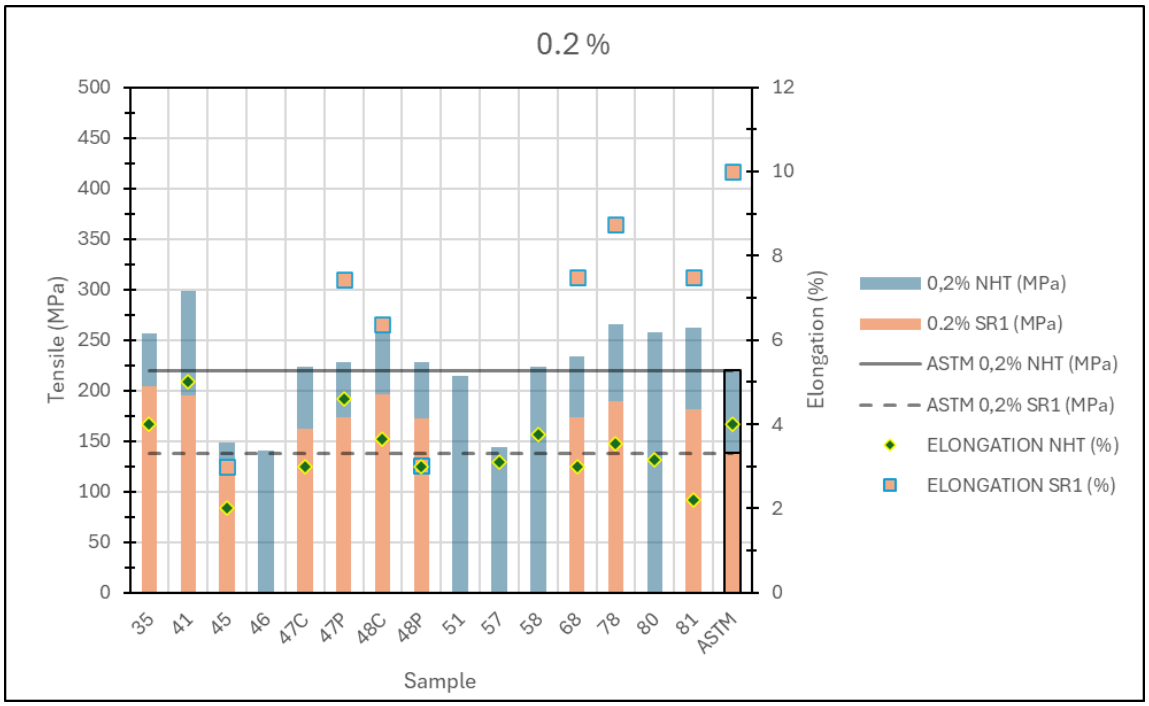

Figure 4.15 – Yield strength, and elongation results as-built (NHT) and after SR1 heat treatment for studied specimens in comparison with ASTM 3318 values.

Based on the results presented in Figure 4.14, it can be observed that only five of the samples comply with ASTM F3318 in the as-built condition. However, after heat treatment, nine out of the ten specimens subjected to thermal processing meet the ASTM F3318 requirement, achieving at least 241 MPa of ultimate tensile strength (UTS). A clear homogenization of UTS values is evident following heat treatment.

With regard to the yield strength values, samples 45, 46, 51, and 57 do not comply with ASTM F3318 in the as-built condition. Similarly to the UTS results, for yield strength, nine out of the ten samples comply with ASTM F3318 after heat treatment.

4.2.3. Hardness

In Figure 4.16 are presented the values of Vickers Hardness measurements along the specimens in the as-built conditions. It is observed a pronounced variation of hardness values along of the specimens.

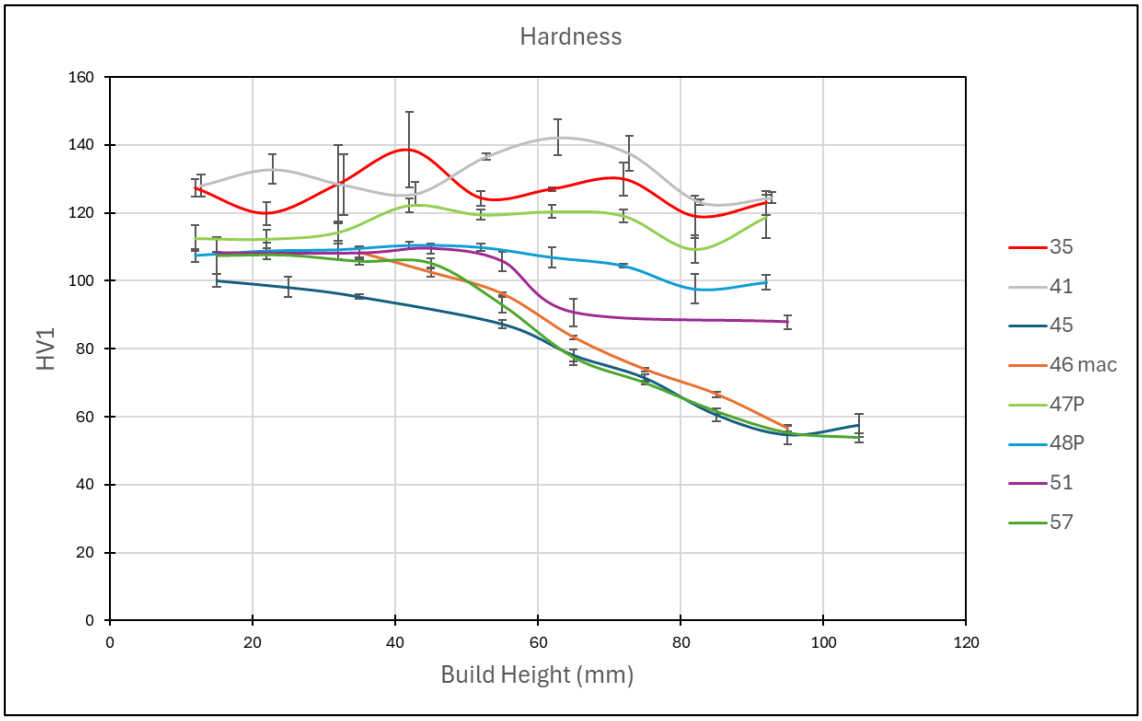

Figure 4.16 – HV1 results from bottom to top specimen. The error bars represent the standard deviation of the measured values.

The hardness of samples from builds 35 and 41 were analysed. Two specimens for build 35, one in the as-built condition and the other subjected to SR1 heat treatment, and one specimen for build 41, before and after heat treatment. Figure 4.17 shows the comparison in between these samples. It was observed that for both builds the hardness values decrease and became very similar along of the specimen heat-treated.

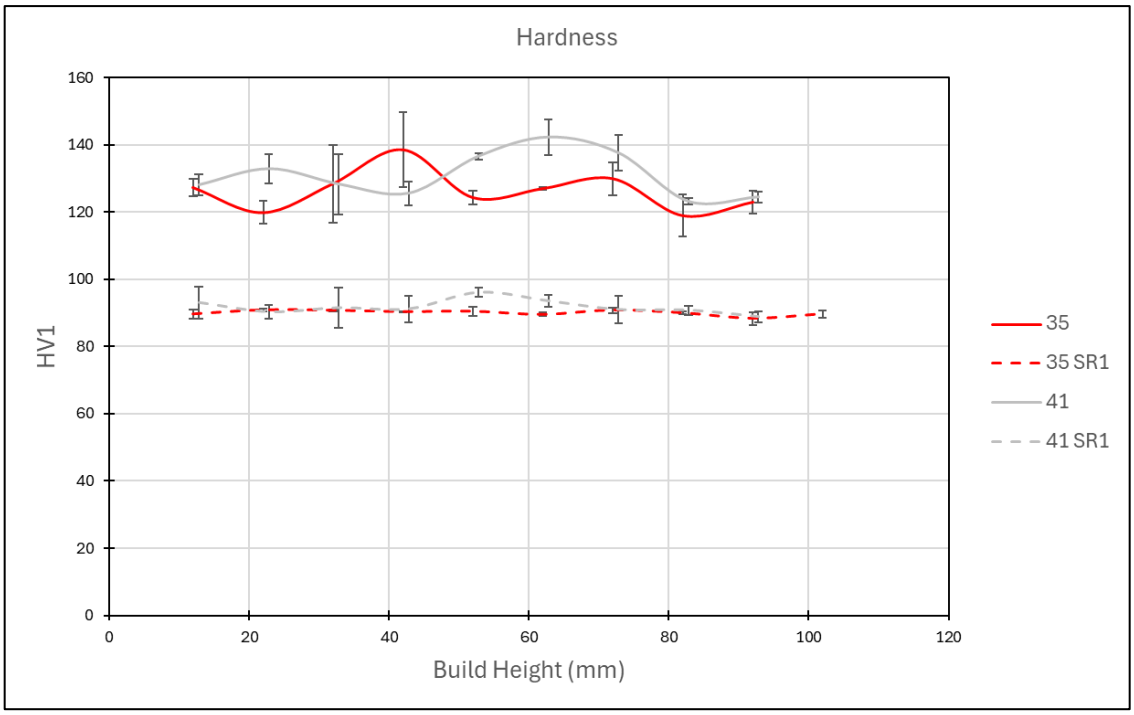

Figure 4.17 – Comparison between the hardness of samples 35 and 41, as-built and with heat treatment (SR1).

Figure 4.18 – HV1 dispersion per build.Figure 4.18 shows the dispersion of HV1 results per build for all builds studied. it was not possible to assess hardness along the entire specimen of build 68, because it rotates during cutting (sample preparation task).

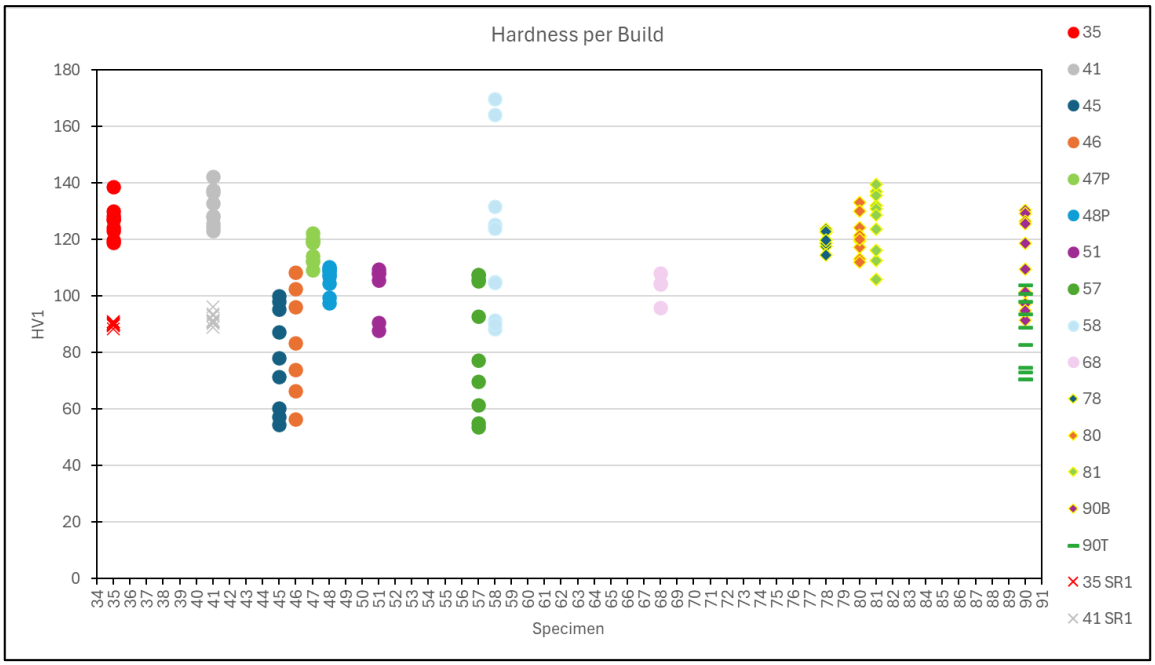

Figure 4.18 – HV1 dispersion per build.

4.2.4. Microstructure

Figure 4.19 presents optical microscope images at 50x magnification, (Leica Visoria|M) showing the top and bottom regions of selected specimens, in order to illustrate the defects observed and to identify the areas in which these defects are most prevalent.

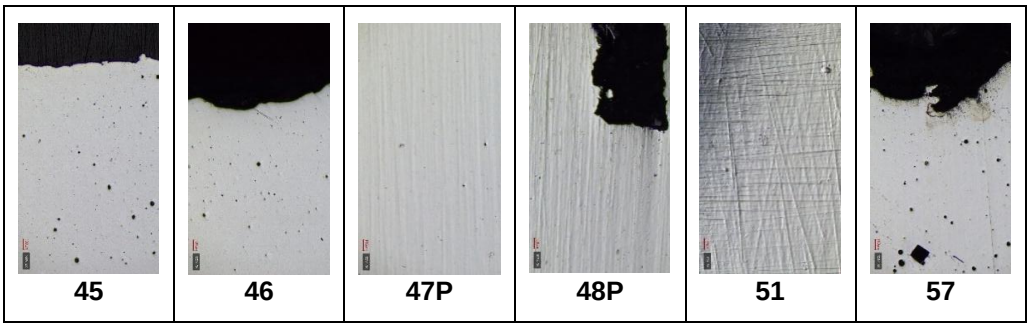

Figure 4.19 – Optical Microscopy images 50x magnification of top region from 45, 46, 47P, 48P, 51, and 57 specimens.

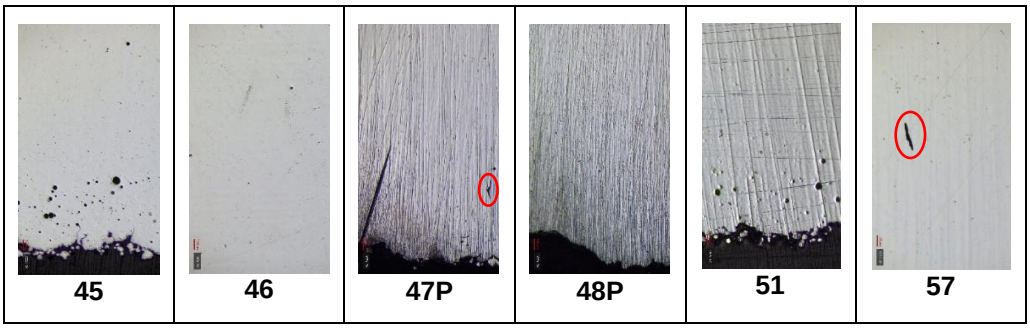

Figure 4.20 – Optical Microscopy images 50x magnification of bottom region from 45, 46, 47P, 48P, 51, and 57 specimens.

Analysis of Figure 4.19 and Figure 4.20 shows that samples 45 and 51 exhibit a high concentration of gas pores at the bottom of the specimen, whereas samples 45, 46, and 57 display some concentration of the same defect at the top of the specimen. Samples 47P, 48P, and 51 also present this type of defect; however, the number of pores is significantly lower compared with the previously mentioned samples. Although the surface quality of samples 47P, 48P, and 51, particularly in terms of polishing is not optimal at the bottom of the specimens, it is still possible to identify some gas pores at the bottom of sample 47P, as well as lack-of-fusion (LOF) defects at the bottom of samples 47P and 57, surrounded by a red outline. It should be noted that in Figure 4.19, the indentation mark from the previously performed hardness test can be observed on sample 57.

Following etching with Keller's reagent, the specimens were initially inspected using optical microscopy to verify contrast development (Figure 4.21) and then subjected to detailed characterisation by scanning electron microscopy (SEM).

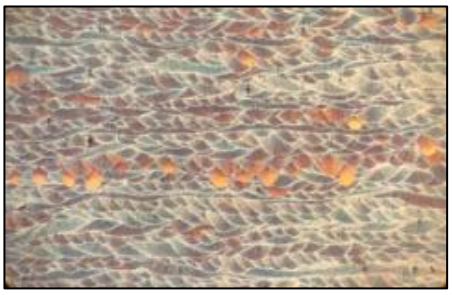

Figure 4.21 – Optical micrograph 50x magnification from a specimen etched with Keller's reagent for 30 seconds.

The melting pools become clearly discernible after etching with Keller's reagent, Figure 4.21. The heterogeneity of the melting pools is attributed to the 67° rotation angle of the laser path in each layer.

Two major questions are addressed through SEM analysis: one concerns the structural differences between as-built and heat-treated samples, and the other relates to the microstructure variations in samples exhibiting hardness variations along the specimen.

Sample 41 was examined in several regions (C, E, and H) before and after being subjected to heat treatment at 280 °C for 2 hours. Figure 4.22 presents the SEM micrographs corresponding to the as-built specimen.

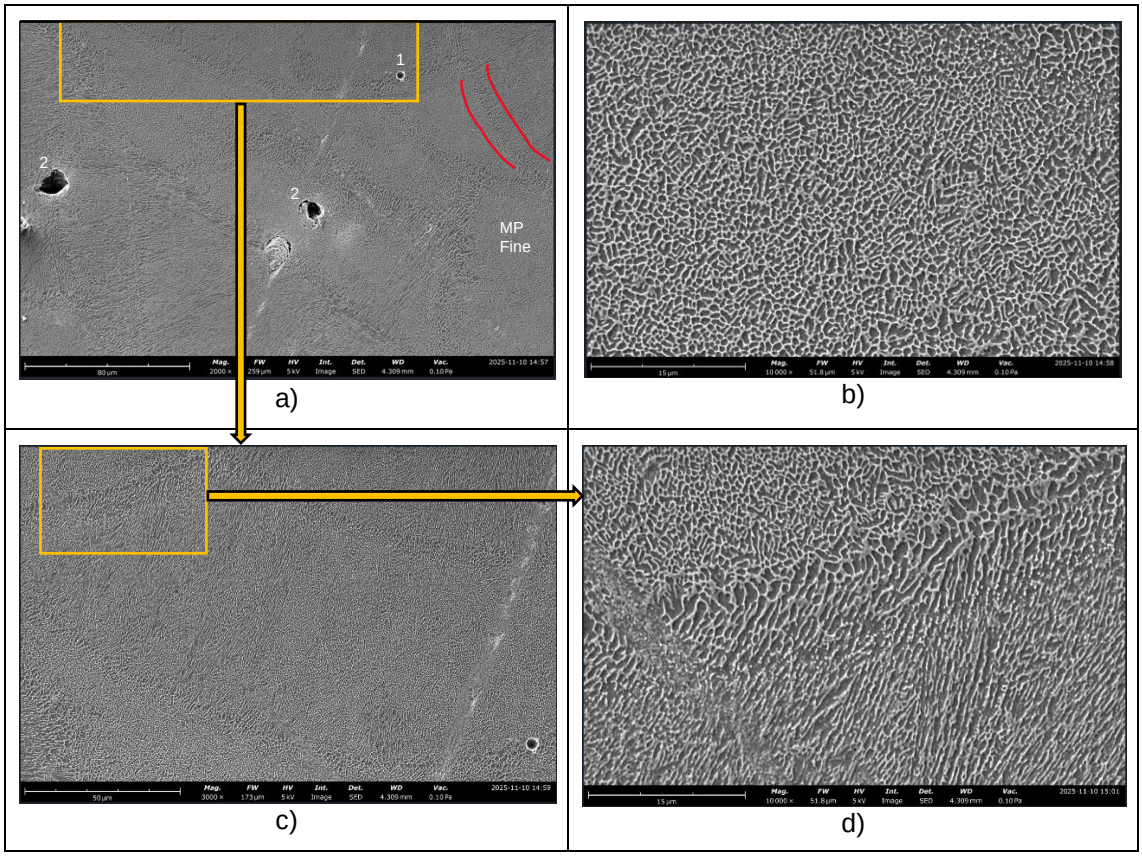

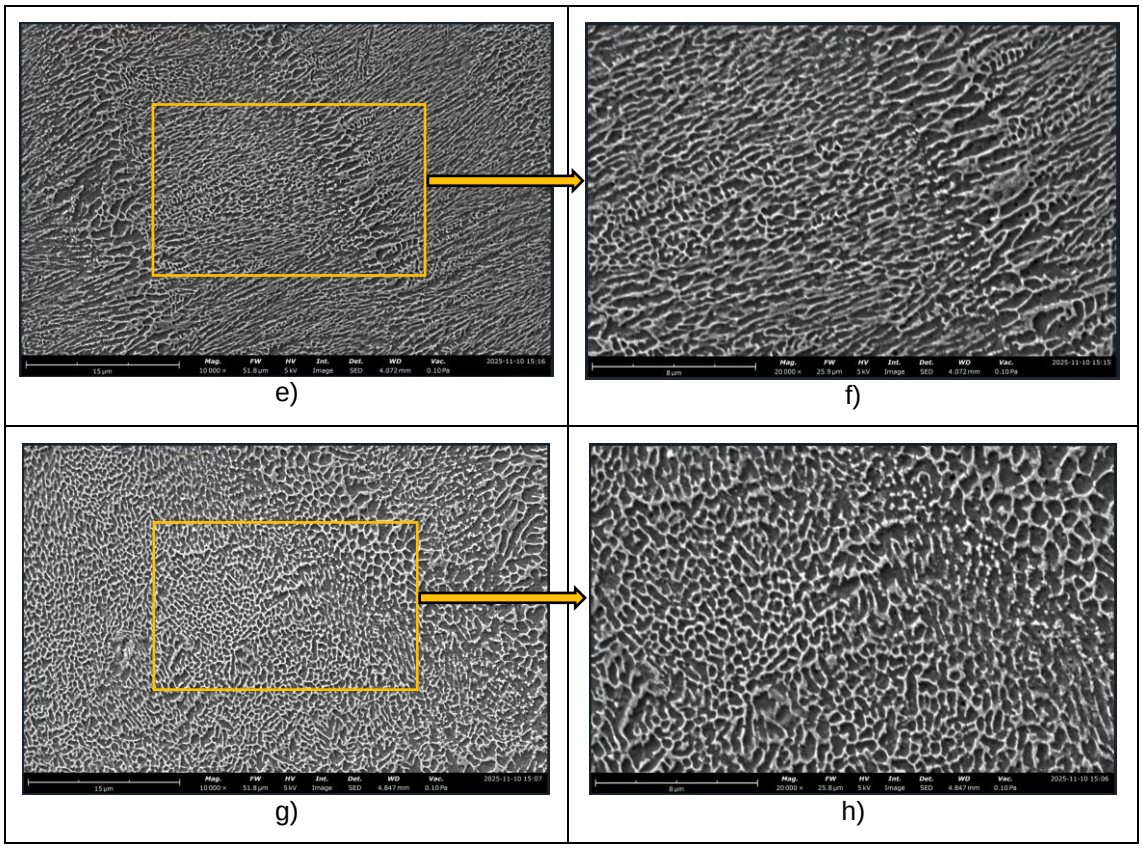

Figure 4.22 – SEM micrographs from sample 41 as-built: zone C a) 2000x, b) 10000x, c) 3000x, and d) 10000x; zone E e) 10000x and f) 20000x; zone H g) 10000x and h) 20000x.

In this specimen, a homogeneous structure is observed, as the microstructure recorded in the three analysed regions is highly consistent. Subsequently, Figure 4.23 displays the SEM images of the same specimen, taken from the same regions after undergoing the SR1 heat treatment.

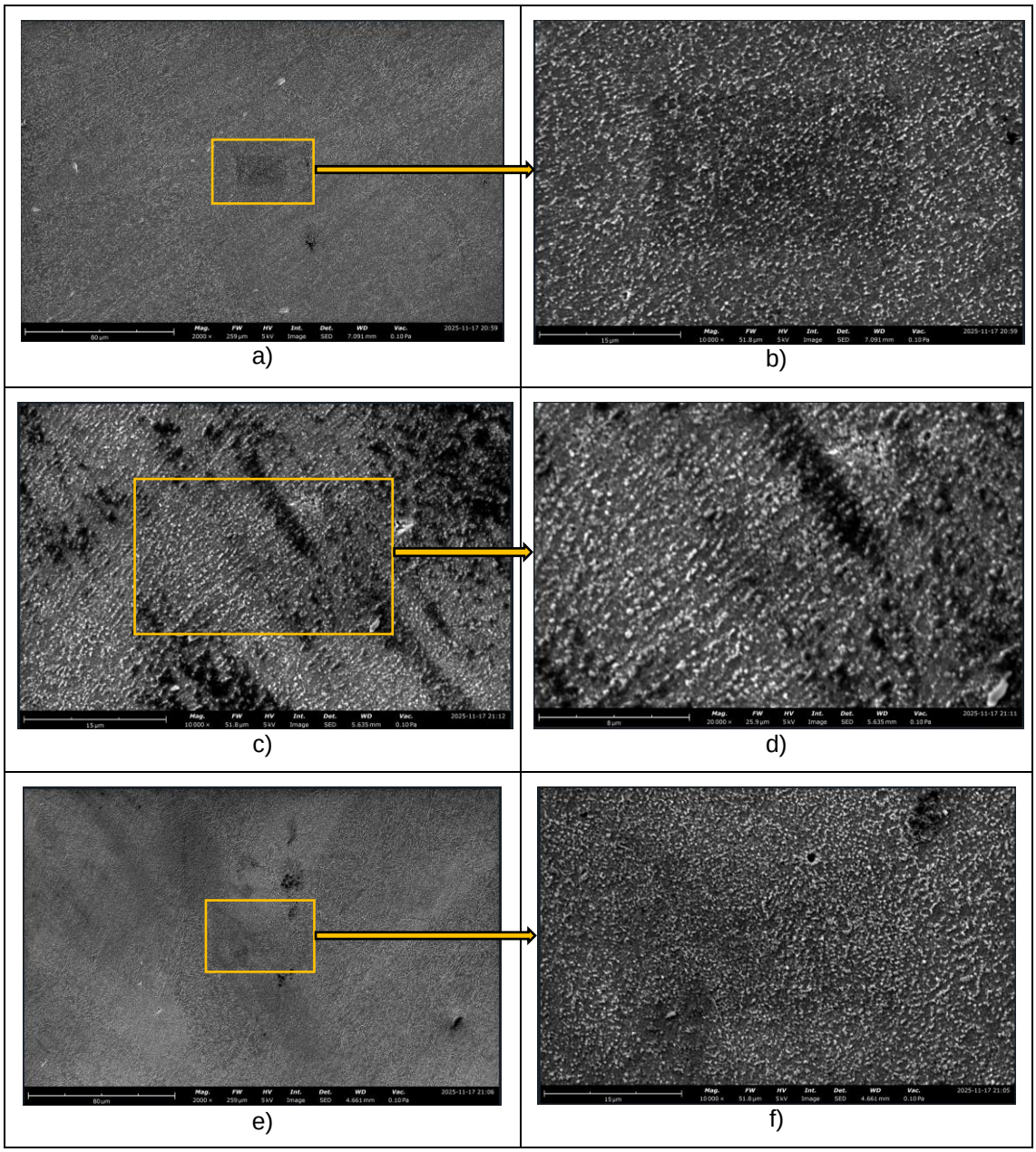

Figure 4.23 – SEM micrographs from sample 41 heat-treated: zone C - a) 2000x, b) 10000x; zone E - c) 10000x and d) 20000x; zone H - e) 2000x and f) 10000x.

As shown in Figure 4.22 a), the sample exhibits defects such as porosity (1) and lack of fusion (LOF) (2). The characteristic fish-scale pattern of the longitudinal section (along the zz-axis) is also visible. The red lines highlight a melt pool boundary. Figure 4.22 b) corresponds to a fine melt pool (MP Fine) at 10000× magnification, while Figure 4.22 c) partially represents the area marked in orange in image a), which includes the region shown in d) at 10000× magnification, corresponding to a melt pool boundary (MP Coarse) and the heat-affected zone (HAZ). Figure 4.22 e) and f) display the microstructure of region E at magnifications of 10000× and 20000×, closely resembling that of region C. Finally, Figure 4.22 g) and h) correspond to region H of the specimen also reveal the same microstructure, constituted by α-Al cells delineated

by the eutectic interdendritic Si, as reported by Phutela et al. (2023).

Concerning hardness variations along the specimen, sample 58 was observed into two regions, approximately at position C and H in the specimen referring to Figure 3.13. These regions were identified based on their hardness values, which were approximately 170 HV1 at position C and 90 HV1 at position H, indicating significant variation in material properties across the sample. Figure 4.24 a) illustrates the regions of the specimen where the images were captured, while Figures b) and c) present the corresponding SEM images of those regions.

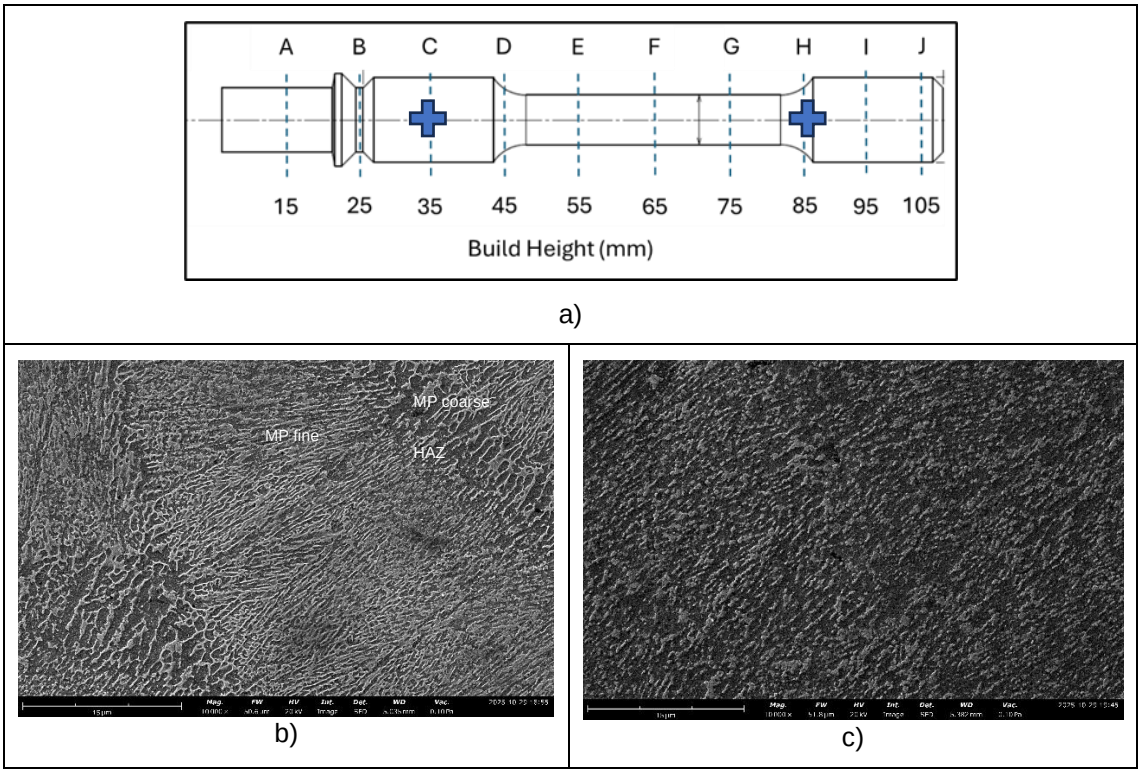

Figure 4.24 – a) Positioning of the analysed areas taking into account the hardness results. b) and c) SEM images from sample 58, 10000x magnification at positions C and H, respectively.

In Figure 4.24 b), as described by Syrlybayev et al., (2024) and Song et al. (2024), the melting pool (MP fine), the melting pool boundary (MP coarse), and the heat-affected zone (HAZ) can be observed. In this region of the sample, the microstructure exhibits a fine architecture, as reported by Bosio et al. (2023), whereas in Figure 4.24 c) a clear disruption of the Al columnar cells previously identified in Figure 4.24 b) can be noted.

Chapter 5

Discussion

This chapter presents a discussion of the results obtained in the previous chapter, establishing correlations among them and seeking to identify possible explanations for the observed outcomes and relationships.

One of the main objectives of the project, Pro Aero 3D, in which this internship is integrated is the qualification of the production process for aeronautical components through additive manufacturing. This internship contributes to that goal by compiling standards related to the production of AlSi10Mg parts using the L-PBF process. Additionally, the scope of this internship includes the assessment of feedstock quality for the production of these components, not only for supplier-provided powder (powder 1), but also for the powder recirculated within the machine (powder 2), the powder extracted by the cyclone (powder 3), and the cyclone powder externally sieved (powder 4), here referred to as recycled, to distinguish it from reused powder circulating in the machine. Furthermore, the evaluation of the quality of the manufactured parts is intended, based on their mechanical properties, excluding dimensional accuracy and surface finish quality.

Following existing standards governing this technology, its feedstock, and the final components, several samples were analysed considering the different powder types, focusing on particle size distribution, chemical composition, morphology, and flowability. The ultimate step in determining powder quality involved evaluating its influence on mechanical properties. To achieve this, tensile specimens were produced alongside the parts under manufacture and subsequently assessed for density, subjected to tensile testing, hardness measurements along their height, and microstructural analysis. This approach aimed to determine whether the powders employed possessed the requisite quality to produce components meeting the desired specifications.

Regarding powder characterization, multiple lots from three different suppliers were examined. Comparison of the particle size distribution for virgin powders (powder 1) revealed that supplier 2 exhibited a broader size dispersion, with a higher proportion of both finer and coarser particles than the other two. Furthermore, it was observed that when powder 2 circulates within the machine without the addition of virgin material, the proportion of larger particles decreases with the number of jobs, leading to a corresponding increase in finer particles (Figure 4.3). As explained by Santecchia et al. (2020), when laser radiation interacts with powder particles during a laser powder bed fusion process, several phenomena occur simultaneously, which can be classified as denudation and the generation of heat-affected powder (spatter and condensate).

Spatter particles typically exhibit a broad size distribution, which is strongly influenced by laser power. Lower laser power tends to generate smaller spatters, whereas higher power results in the formation of larger particles and an increased quantity of ejected material (Gunenthiram et al., 2017). Highly coarse particles, larger than 100 µm, may occur (Santecchia et al., 2020). These particles may either become fused to the part or remain loose within the powder bed. When the build is completed, if they become fused to the part, they will be removed together with it. If they remain in the powder bed, the coarse particles will be retained by the internal sieve (95 µm) if they exceed this diameter, thereby reducing the proportion of larger particles from the previous powder 2. Consequently, the lack of renewal of the hopper with new powder leads to a progressive decrease in the particle size distribution.

Concerning the chemical analysis of the powders, the available technique proved incapable of accurately quantifying elements with atomic numbers below ten, such as oxygen, despite being

a method referenced in ISO/ASTM 52907:2019 (2019). Nevertheless this standard is silent on the subject for this studied alloy, AlSi10Mg, for oxygen, nitrogen and carbon detection. Oxygen would be of particular importance, as it would allow assessment of oxide formation during the L-PBF process and, consequently, evaluation of the quality of the powder used. Considering the results obtained, and focusing solely on the mean values, copper, magnesium, and silicon tend to appear at levels above those specified in ASTM F3318-18. When comparing the chemical composition of samples from consecutive builds, no consistent trend of increase or decrease in any of the analysed elements is observed. Therefore, despite the limitations of the technique used, no changes in chemical composition appear to occur due to powder recirculation in the machine, as also noted by Ladewig et al. (2016).

The morphology of the analysed powders is largely similar across all samples, and the types of defects identified, such as satellites, agglomerates, elongated particles, open porosity, and splat caps are common to all of them. The same results were reported by Měsíček et al. (2022). The most notable difference is observed in powder 3 sample, which contains particles of larger dimensions, as expected, given that it had not yet undergone sieving. With respect to powder 3, it was found that the external sieving process was highly effective, enabling the recovery of approximately 85 to 88% of the cyclone powder and yielding powder 4, which exhibits a particle size distribution comparable to that of the new powder (powder 1).

Regarding the flowability of powder 1 samples, it was observed that the sample from supplier 3 exhibits lower flowability compared to those from the other suppliers. As referred by Martucci et al. (2023), lower flowability implies higher powder density, suggesting that components produced with this powder may achieve higher densities than those manufactured under identical conditions using powders from other suppliers.

When comparing the flowability of samples 45A, 45B, 46, and 47, these were ranked from highest to lowest flowability, which would correspond to an inverse relationship with powder density. However, during the internship period, it was not possible to access powder density measurements due to the unavailability of the technique. Attempting to correlate powder flowability with specimen density, sample 47, which exhibited the lowest flowability and thus would be expected to have the highest powder density, also showed the highest specimen density. This observation appears consistent with expectations. Nevertheless, in the case of samples 45B and 46, sample 45B demonstrated higher flowability, which would suggest lower powder density and consequently lower specimen density, a trend that was not observed. This discrepancy may be explained by the influence of additional factors contributing to defects such as porosity, which are related to process parameters, including temperature and layer time, and which may override the effect of powder density.

Initially, the specimens manufactured during the build were intended solely to assess the quality of the powders employed. Consequently, regardless of the build parameters, all specimens were produced under identical processing conditions, ensuring that the only variable was the powder utilized. Table 5.1 provides a summary of the parameters and properties

investigated.

Table 5.1 – Parameters and Properties for each studied build.

		Build						
Nr.		**35**	**41**	**45**	**46**	**47**	**48**	**51**
Picture		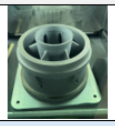		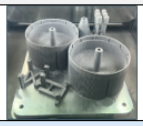		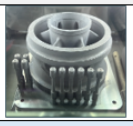		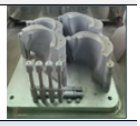
Parameters								
Laser Strategy		Meander	S&C	Stripe	Stripe	Stripe	Stripe	Stripe
Thickness (µm)		60	30/60	60	60	Sp:60 B:30	60	60
Layer Time (min)	Max	0.507	0.500	0.500	0.615	1.086	0.472	0.649
	Min	0.200	0.176	0.131	0.130	0.400	0.215	0.196
Build T (hh:mm)		20:29	15:54	07:26	07:16	20:00	08:53	12:47
Temp. (°C)	Max	170	n.a.	170	172	170	178	n.a.
	Min	170	80 set up	170	170	170	170	170 set up
Height (mm)		146.37	146.37	106.98	106.98	146.37	146.37	108.00
Powder addition	kg	8 before	4 during	0	0	4 b + 4 d	4 during	0
	Nr.	0	0	3	4	0	0	1
Properties								
UTS (MPa)	NHT	421	484	219 ± 6	226 ± 3	415 ± 2	371 ± 3	355 ± 4
	SR1	310	305	202	-	303	297	-
HV1	Max	138.51	142.24	100.07	108.26	122.25	110.33	109.50
	Min	118.89	123.12	54.56	56.48	109.29	97.63	74.49
Density (%)		98.92	99.08	98.07	98.36	99.14	98.77	98.73

		Build						
Nr.		**57**	**58**	**68**	**78**	**80**	**81**	**90**
Picture								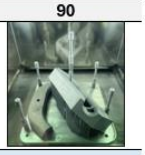
Parameters								
Laser Strategy		Stripe	Stripe	Stripe	Stripe	Stripe	Stripe	Stripe
Thickness (µm)		Sp:60 B:30	30	60	60	60	60	60
Layer Time (min)	Max	2.180	0.384	0.550	0.209	0.830	0.374	0.528
	Min	0.126	0.153	0.200	0.156	0.373	0.195	0.116
Build T (hh:mm)		27:14	12:08	10:30	10:03	21:57	17:04	09:29
Temp. (°C)	Max	170	170	170	95	176	134	144
	Min	170	170	170	95	95	95	95
Height (mm)		106.98	178.83	117.54	109.98	267.78	283.62	222.00
Powder addition	kg	0	12 before	0	0	24 during	8 during	8 before
	Nr.	2	0	1*	4	0	0	0
Properties								
UTS (MPa)	NHT	222 ± 4	368 ± 1	387 ± 2	428 ± 27	402 ± 16	394 ± 7	-
	SR1	-	-	296 ± 0	299 ± 1	-	296 ± 1	-
HV1	Max	107.58	169.56	108.20	123.65	133.05	139.46	**B**:130.15;**T**:103.65
	Min	53.75	88.48	n.a.	114.57	112.01	105.77	**B**:91.40;**T**:70.40
Density (%)		97.72	98.78	98.36	99.02	98.55	98.64	**B**:98.73;**T**:98.52

Sp – Specimen; B – Build; Build T – Build Time; Temp. – Build-platform Temperature; n.a. – not available; b – before; d – during; Nr. – Number of consecutive builds without adding new powder; * – Recycled powder added in builds 65, 67, 70, 72 and 73; **B** – Bottom; **T** – Top.

To evaluate the effect of production parameters on the relative density of the specimens, the experimental data were organized in descending order of density, as shown in Figure 3.2. No consistent trend was observed between relative density and the number of builds produced without the addition of fresh powder. However, the builds exhibiting the lowest relative density correspond to cases where the specimen size exceeded the build dimensions, with the exception of build 68, which, despite having a smaller specimen, was manufactured using recycled powder.

Table 5 2 – Build Ranking by Relative Density.

Relative Density (%)	Build	Nr. of builds without adding new powder	Tallest	Set-up Temperature (ºC)	Laser strategy and Thickness (µm)
99.14	47P	0	Build	170	Stripe 60
99.08	41	0	Build	80	S&C 30/60
99.02	78	4	Control	95	Stripe 60
98.92	35	0	Build	170	Meander 60
98.78	58	0	Build	170	Stripe 30
98.77	48P	0	Build	170	Stripe 60
98.73	51	1	Build	170	Stripe 60
98.73	90B	0	Build	95	Stripe 60
98.64	81	0	Build	95	Stripe 60
98.55	80	0	Build	95	Stripe 60
98.52	90T	0	Specimen	95	Stripe 60
98.36	68*	1	Build	170	Stripe 60
98.36	46	4	Specimen	170	Stripe 60
98.07	45	3	Specimen	170	Stripe 60
97.72	57	2	Specimen	170	Stripe 60

In Table 5.3, the as-built UTS values were arranged in descending order to assess whether production parameters influence this property. Examination of Table 5.3 reveals a similar trend, builds with heights exceeding their corresponding specimen dimensions appear first, reflecting superior results. Once again, no correlation was observed between the number of builds produced without the addition of fresh powder and the property under investigation, in this case, UTS. However, the lowest values were obtained when the specimen size exceeded the respective build dimensions. Furthermore, a tendency related to the build platform set-up temperature was identified, with the highest UTS value recorded at a temperature of 80 °C.

Table 5.3 – Build Ranking by UTS (NHT).

UTS (MPa)	Build	Nr. of builds without adding new powder	Tallest	Set-up Temperature (ºC)	Laser strategy and Thickness (µm)
484	41	0	Build	80	S&C 30/60
428	78	4	Control	95	Stripe 60
421	35	0	Build	170	Meander 60
415	47P	0	Build	170	Stripe 60
402	80	0	Build	95	Stripe 60
394	81	0	Build	95	Stripe 60
387	68*	1	Build	170	Stripe 60
371	48P	0	Build	170	Stripe 60
368	58	0	Build	170	Stripe 30
355	51	1	Build	170	Stripe 60
226	46	4	Specimen	170	Stripe 60
222	57	2	Specimen	170	Stripe 60
219	45	3	Specimen	170	Stripe 60

Arranging the data by decreasing hardness mean values yields the sequence shown in Table 5.4.

Once again, no correlation was identified between the number of builds produced without the addition of new powder and the property under investigation, in this case, hardness. The previously observed trend is confirmed, indicating that superior results are associated with builds whose height exceeds that of their respective specimens.

Based on the comparison presented in Table 5 2, Table 5.3, and Table 5.4, conclude that there is no relationship between the number of builds without addition of new powder and the studied properties. For instance, build 78, which was manufactured without powder renewal over four consecutive builds, exhibited properties comparable to those obtained with fresh powder. Similarly, build 68, produced using recycled powder, demonstrated performance consistent with the other studied builds. Ifeanyi Iwediba et al. (2023), conclude that reused powders can still be used in additive manufacturing when it has undergone sieving. On the other hand, Měsíček et al. (2022) suggests that recycled powder after 30 printing cycles can be utilized for SLM component preparation to achieve cost-effectiveness. However, comparison of products with the use of virgin and recycled powders showed that the use of recycled powder affects the submicron characteristics (precipitate size increase), density and the resulting mechanical properties.

Table 5.4 – Build Ranking by HV1 mean values.

HV1	Build	Nr. of builds without adding new powder	Tallest	Set-up Temperature (ºC)	Laser strategy and Thickness (µm)
130.97	41	0	Build	80	S&C 30/60
126.33	35	0	Build	170	Meander 60
126.10	81	0	Build	95	Stripe 60
121.13	80	0	Build	95	Stripe 60
119.92	78	4	Control	95	Stripe 60
119.40	58	0	Build	170	Stripe 30
116.50	47P	0	Build	170	Stripe 60
112.40	90B	0	Build	95	Stripe 60
105.99	48p	0	Build	170	Stripe 60
103.20	68*	1	Build	170	Stripe 60
101.67	51	1	Build	170	Stripe 60
85.49	90T	0	Specimen	95	Stripe 60
83.85	46	4	Specimen	170	Stripe 60
83.67	57	2	Specimen	170	Stripe 60
78.08	45	3	Specimen	170	Stripe 60

It is noteworthy that the laser scanning strategy meander with a 60 µm layer thickness yielded excellent results even at a set-up temperature of 170 °C.

Most as-built UTS values were below the minimum ASTM F3318 requirements, likely due to microstructural heterogeneity. Significant hardness variations were observed along the specimens, reflecting microstructural inconsistencies. Subsequent heat treatments promoted microstructural homogenization, as confirmed by hardness measurements and SEM observations, resulting in UTS values that met ASTM F3318 standards for the majority of the builds. Additionally, an increase in elongation was observed. These findings align with those reported by Hwang et al. (2023) who documented similar behaviours in their study on the effect of stress relief heat treatment on AlSi7Mg and AlSi10Mg alloys on mechanical and electrical properties according to silicon precipitation.

The hardness results measured along the specimens with larger dimensions than the other produced parts, (Figure 4.16) show a pronounced decrease in hardness along the build height for builds 45, 46, and 57, respectively, 45.5%, 47.8%, and 50.0% of reduction in hardness. Further analysis of the layer exposure time for these builds indicates that lower hardness values tend to occur in layers with shorter exposure durations. The observed reduction in hardness may have

been caused by excessive heat during fabrication, resulting from the application of the same energy input while the layer time simultaneously decreased, due to a reduction in the area processed per layer from a certain height onward. Table 5.5 is intended to illustrate this dependence of layer time on the area processed per layer for build 51.

Table 5.5 – Printed Area per Layer and Layer Time for build 51.

Layer Nr.								
250	417	583	750	917	1083	1417	1583	1750
Printed Area per Layer								
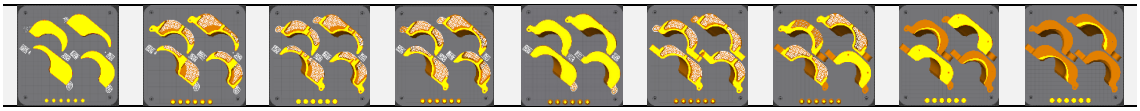								
Layer Time (min)								
0.649	0.471	0.458	0.461	0.600	0.561	0.498	0.425	0.196

The images presented in Table 5.5 correspond to a top view of the build platform. The yellow-highlighted areas indicate the regions to be printed in the represented layer. The orange regions correspond to areas that have already been printed. The information presented in Table 5.5 clearly demonstrates that the layer time is dependent on the amount of surface area that needs to be processed.

It is also evident that lower properties are achieved when the specimens are higher than the parts, as a result of experiencing markedly different processing conditions during fabrication. Comparing a build in which the specimens are shorter than the part, such as build 47, with build 57, where the specimens are considerably taller than the parts (Figure 5.1), it becomes clear that build 57 is strongly influenced by layer time, whereas this relationship is not observed in build 47.

Figure 5.1 clearly illustrates the dependence of hardness along the specimen on layer exposure time, as well as the influence of the build area per layer. As shown in Table 5.1, build 57 exhibits a relatively large build area per layer up to a certain height, after which only the specimens are constructed. This transition results in a sharp reduction in layer time, which in turn leads to a gradual decrease in hardness along the height of the specimen. This observation suggests that the build area per layer significantly influences the mechanical properties of the manufactured parts. It also highlights that specimen properties are affected by their surrounding context and may not always be representative of the actual components produced. For instance, in build 57, assuming that both the parts and the portion of the specimens built alongside them are subjected to similar influencing factors, their mechanical properties should be comparable. However, once the specimens become the only elements being constructed, the layer time decreases, which in turn affects their properties, potentially resulting in lower UTS values than would be expected if the specimens had been built under consistent process conditions. This

suggests that the specimen height should correspond to the height of the components being produced, in order to ensure better consistency of the construction parameters between the specimens and the actual build.

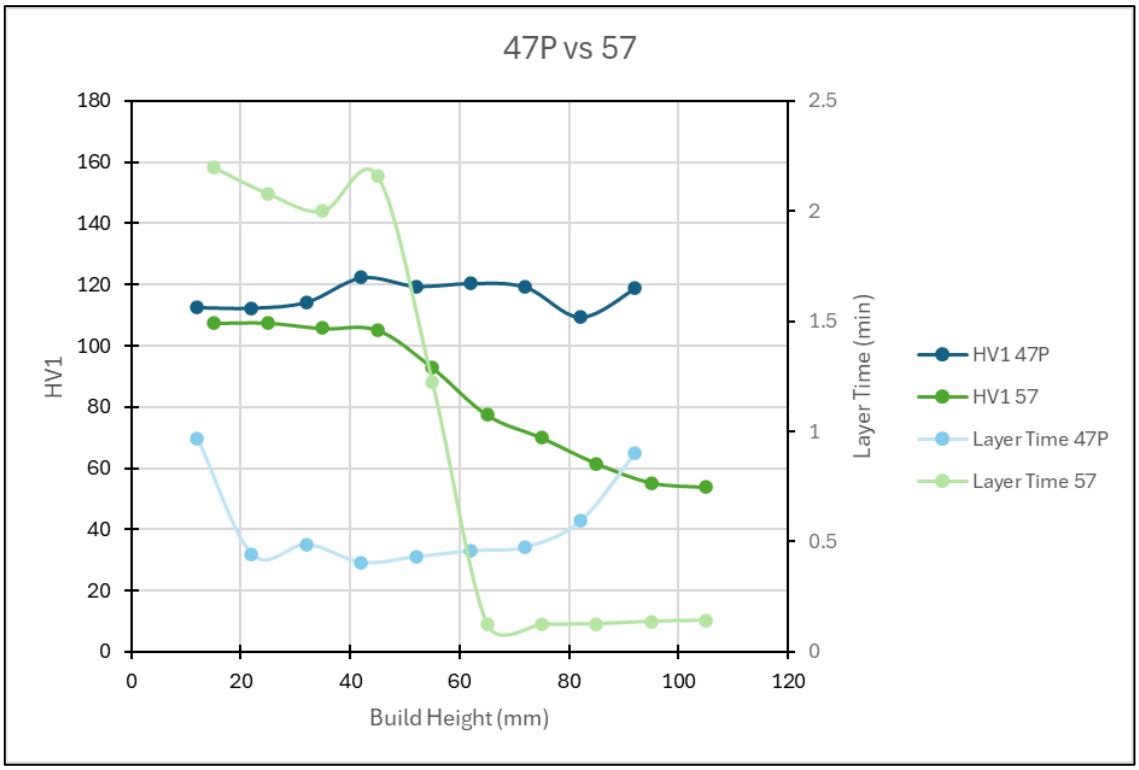

Figure 5.1 – Hardness and Layer Time relations with Build Height.

For each build, a potential relationship between hardness and layer time was investigated, and it was concluded that, for builds with a height lower than the specimen, a correlation exists, with coefficients of determination (R^2) of 0.93, 0.88, and 0.90 for builds 45, 46, and 57, respectively, as shown in Figure 5.2.

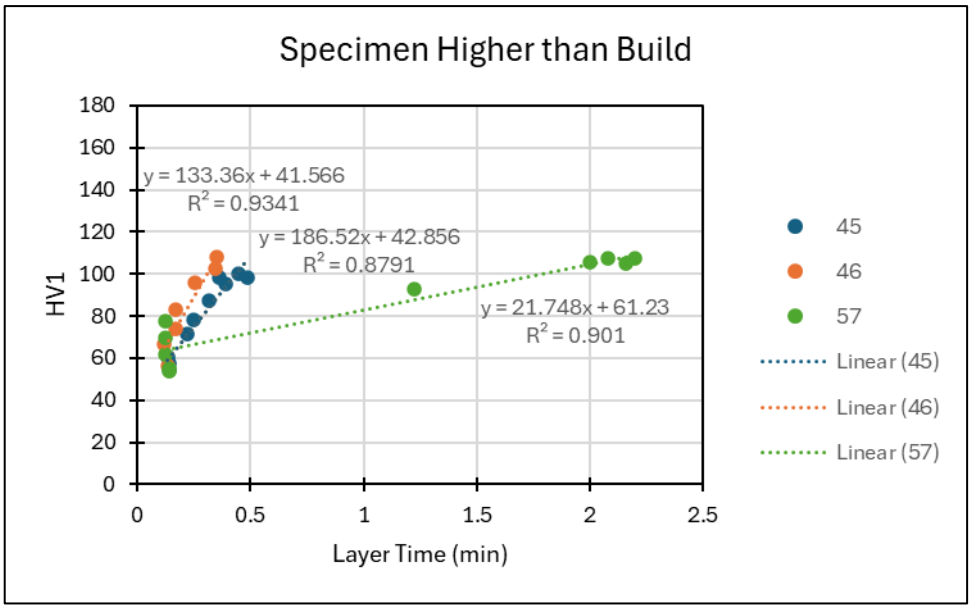

Figure 5.2 – HV1 vs Layer Time Correlation for builds with a height lower than the specimen.

For the other type of builds which are higher than the specimen, there are no correlation in between hardness and layer time, as it is shown in Figure 5.3.

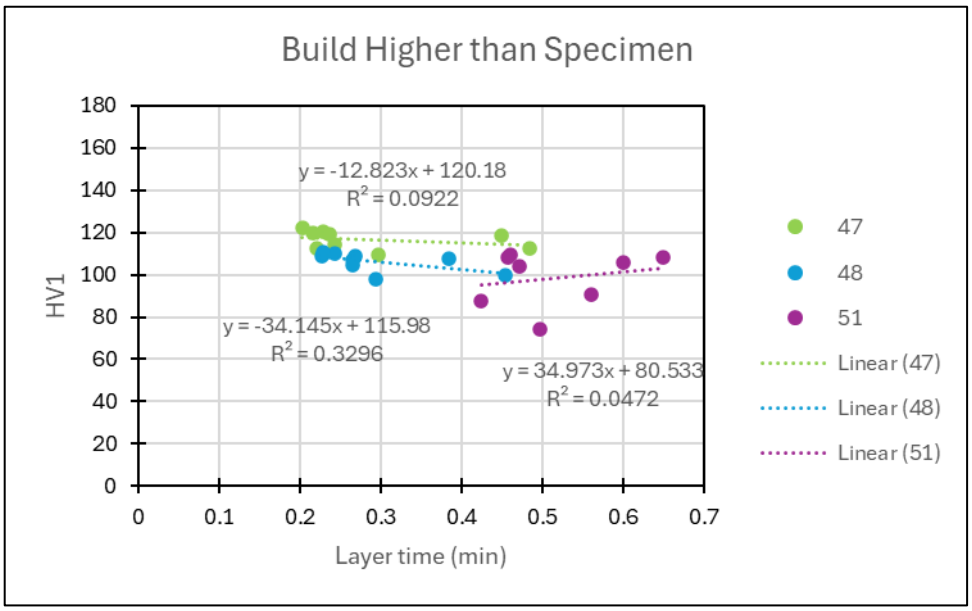

Figure 5.3 – HV1 vs Layer Time Correlation for build higher than specimen.

When the specimens are smaller than the components, the process parameters remain more stable, exhibiting lower variability. This results in more consistent material properties, specifically hardness values that are more uniform throughout the entire specimen. Consequently, any potential correlation observed in builds smaller than the specimen is lost.

The fact that the specimens from shorter builds exhibit poorer results does not necessarily indicate that the powder used in those builds was of inferior quality. However, once the specimens become the only elements being constructed, the layer time decreases, leading to a thermal accumulation and to a slow cooling rate. Meanwhile eutectic Si decomposes, creating fine Si-agglomerates in α-Al matrix (Syrlybayev et al., 2024). Indeed, the microstructure observed in the regions of the specimens exhibiting lower hardness (90 HV1) closely resembles that of the heat-treated specimens (circa 90 HV1) (Figure 5.4). Phutela et al., (2023) reported an average hardness values decreased by nearly 52% on increasing the bed temperature.

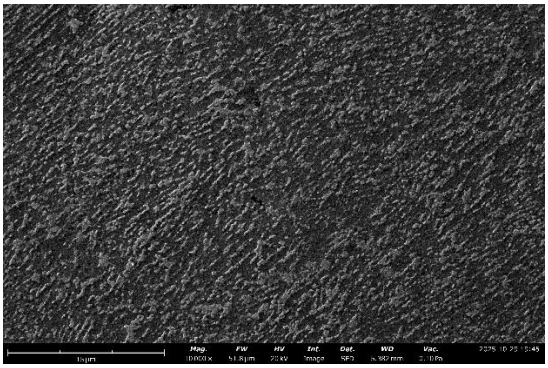

a)

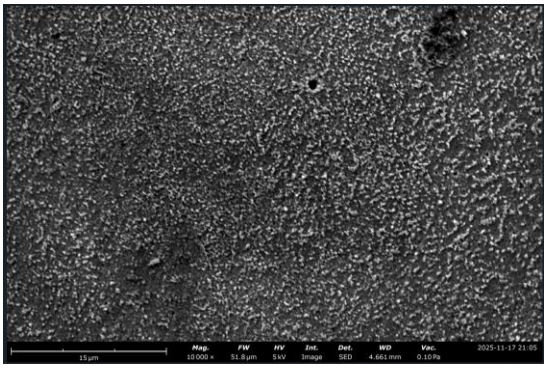

b)

Figure 5.4 – SEM micrographs from sample a) 58 as-built in zone H: low HV1; and b) 41 after SR1 heat-treatment.

It was further observed that heat treatment affects both, hardness and microstructure. As shown in Figure 4.17, the hardness of samples 35 after heat treatment shows a reduction of approximately 36 HV1, decreasing from 126 HV1 in the as-built state to 90 HV1 after SR1 heat treatment. A clear disruption of the previously identified Al columnar cells (Figure 4.23 b)) can be observed following heat treatment. Hwang et al. (2023) also reported that the Vickers hardness of each specimen decreased after the heat treatment.

The geometry of the specimens also impedes heat dissipation when layer time decreases. Since the top of the specimen is wider than the region under it, heat dissipation becomes less effective. Saunders, (2019) explains that as each new layer is added, heat is conduced down into the previous build layers below. Where there is a good thermal connection to the substrate below, heat will dissipate effectively. By contrast, if the part geometry involves thinner walls, or if there is a bulky region immediately above a much thinner section, then heat will not be able to flow down so easily, resulting in more heat being retained near the top of the part. For this reason, it is recommended that the specimens be manufactured as fully cylindrical geometries rather than having a shape similar to the final.

Regarding the processing parameters and comparing only the builds produced with the same part, the crankcase (builds 35, 41, 47, and 48) the best results were obtained for build 41,

which used a build-platform temperature of 80 °C and a Shell and Core scanning strategy with shell/core thicknesses of 30/60 µm, respectively. Build 35 produced the second-best results, using a meander strategy with a 60 µm layer thickness at a build-platform temperature of 170 °C. In third place was the crankcase from build 47, produced with a stripe scanning strategy and a 30 µm layer thickness at 170 °C, and finally build 48, which used the same stripe strategy with a 60 µm layer thickness at the same temperature.

It can therefore be concluded that, at a build-platform temperature of 170 °C (builds 35, 47, ans 48) and with a stripe scanning strategy, a 30 µm layer thickness leads to superior results than 60 µm, which is in accordance with Renishaw results (); conversely, at the same temperature and with a 60 µm layer thickness, the meander strategy yields better performance. Table 5.6 provides a clearer schematic summary of the various parameter combinations, the corresponding builds, and their ranking.

Table 5.6 – Comparison in between parameters for crankcase builds. Green highlights the better result for each property, light-yellow the second best result, orange the third best, and the red the worst result.

Ranking	Build	Relative Density (%)	UTS (MPa)	HV1	Set-up temperature (ºC)	Laser strategy and thickness (µm)	Build Time (hh:mm)
1st	41	99.08	**484**	**130.97**	80	S&C 30/60	15:54
2nd	35	98.92	421	126.33	170	Meander 60	20:29
3rd	47	**99.14**	415	116.50	170	Stripe 60	20:00
4th	48	**98.77**	**371**	**105.99**	170	Stripe 60	08:53

Nevertheless, builds 35 and 47 require long fabrication times, each taking approximately 20 hours, while build 41 requires around 16 hours. In terms of time efficiency, build 48 would be the most favourable option; however, it would only be viable if the customer intends to receive the part after heat treatment, since otherwise its UTS values would fall below the ASTM F3318-18 acceptable limit.

Considering only the laser stripe strategy with a 60 µm layer thickness, as it represents the fastest processing combination, and disregarding specimens taller than the corresponding builds, since these are not representative of the builds themselves, (only the builds 48, 51, 68, 78, 80, 81, and 90B remain) ordering the results in descending order of performance yields Table 5.7. This table reveals a tendency for the highest values of two key properties (UTS and hardness) to occur in builds produced with a setup temperature of 95 °C. However, excluding the control (build 78), none of the builds exceed the thresholds defined by ASTM F3318; therefore, if the customer does not intend to apply heat treatment, none of the builds would be compliant. This analysis highlights the need to investigate lower build platform temperatures and alternative laser strategies in order to achieve parts that meet ASTM F3318 requirements without the necessity

for post-processing heat treatment.

Table 5.7 – Comparison in between ranking properties of relative density, UTS, and HV1 for eligible builds at faster production conditions, regarding set up temperature (set up T).

Ranking by Relative Density			**Ranking by UTS**			**Ranking by HV1**		
Relative Density (%)	Build	set up T (ºC)	UTS (MPa)	Build	set up T (ºC)	HV1 mean	Build	set up T (ºC)
99.02	78	95	428	78	95	126.10	81	95
98.77	48	170	402	80	95	121.13	80	95
98.73	51	170	394	81	95	119.92	78	95
98.73	90B	95	387	68	170	112.40	90B	95
98.64	81	95	371	48	170	105.99	48	170
98.55	80	95	355	51	170	103.23	68	170
98.36	68	170				101.67	51	170

The defects identified in the analysed builds must also be taken into consideration. For example, the specimen from build 57 (170 °C) exhibited a considerable number of pores at the top of the specimen, whereas the specimen from build 41 (80 °C) showed more lack-of-fusion (LOF) defects than any other build. Mitigating or eliminating these defects generally requires reducing the layer thickness, as reported by (Ghio & Cerri, 2022). These authors also note that gas pores are less critical for crack propagation than LOF defects.

It may therefore be stated that no perfect solution exists for the various possible combinations of parameters; there will always be a compromise between those that lead to the best mechanical performance and those that enable shorter build times. The SR1 heat treatment may serve as a means of bringing the produced parts into compliance with ASTM F3318-18, provided the customer is willing to accept the application of such treatment. Dimensional control and surface treatment, although beyond the scope of this study, would also be valuable to investigate in the near future so that they may be incorporated into the optimization of processing parameters.

Chapter 6

Conclusions and Future Developments

This chapter presents the main conclusions of the study and offers suggestions for future research.

Despite standard review aiming qualification process, this study has two primary objectives. The first was to evaluate the quality of the four different types of powder: (1) new powder; (2) hopper; (3) cyclone not sieved, and (4) cyclone after sieving. Powder samples were analysed, by particle size distribution, chemical composition, morphology, and flowability. In order to study the powder quality, specimens were built as the same time as parts, without changing parameters, since the powder itself should be variable in study. However, the second objective is to identify the parameters that lead to the production of parts with superior quality. To achieve this, parameters such as: built platform temperature, layer thickness, and laser scanning strategy were studied.

Regarding the quality of the powders analysed, it can be stated that the three suppliers provide powders with slight differences in particle size distribution, with supplier 2 exhibiting a greater dispersion in particle size compared to the other two suppliers. It is not possible to accurately assess the chemical composition of the powders used, as the available technique does not allow proper quantification of elements with an atomic number lower than ten, such as oxygen, which would be highly relevant for investigating oxide formation in the powder. The selection of analytical methods should be aligned with the intended objective. For instance, in the case of chemical analysis of the powder, atomic absorption spectrometry should be employed, as it is also recommended by ISO/ASTM 52907.

With respect to the reuse of powders in builds without the addition of virgin material, the maximum studied was four consecutive builds under these conditions. Although the sample size is limited, based on the results from build 78, it can be stated that, at least up to this number of cycles, the quality of the parts is ensured with respect to powder integrity.

Regarding the recycling of powders, it can be concluded that the particle size distribution of the powder after sieving (powder 4) is very similar to the particle size distribution of the new powder (powder 1), as it can be seen in Figure 4.6 and Figure 4.7. It was also noticed that the sieving process in the Powder Recovery System (PRS) is very effective, since powder 3 is converted in powder 4, which is very similar to powder 1. This recovery is in the range of 85 % to 88 % (w/w), which means a significant cost saving and reduction of waste.

In terms of powder morphology, it is largely consistent across all studied powders, with the exception of powder 3, which contains particles significantly larger than those in the other samples. These oversized particles are formed during the L-PBF process through spatter accumulation. When directed to the cyclone, they are removed from powder 2, resulting in a decrease in the proportion of larger particles and, consequently, an increase in the proportion of smaller ones. The powder particles observed across the different samples are essentially similar with regard to defects.

A slight trend was observed with respect to flowability: powders exhibiting higher flowability values tend to produce parts with inferior mechanical properties. However, other factors, such as processing temperature and layer time, are likely to have a more significant influence on part quality. Further studies are required to confirm this tendency.

Depending on the intended application of the manufactured parts, heat treatment may be required, and therefore this decision should ultimately be made by the client. The stress relief heat treatment (SR1) applied to some of the specimens revealed, on the one hand, a reduction in tensile strength values and, on the other, a homogenization of UTS SR1 values in between builds, placing them, in most cases, within the SR1 ranges recommended by ASTM F3318. A similar trend was observed in hardness along the specimen; that is, with the SR1 heat treatment, hardness values decreased and became more uniform throughout the specimen (Figure 4.17). This occurs due to the fact that, during heat treatment, a modification in the microstructure of the specimens takes place, eutectic Si decomposes, creating fine Si-agglomerates in α-Al matrix.

Hardness analysis along the specimens revealed that those exceeding the height of their respective builds experience a reduction in layer time once the parts are completed, leading to thermal accumulation and a slower cooling rate. This condition alters the microstructure in a manner similar to an SR1 heat treatment, resulting in decreased hardness and tensile strength, with the specimen entering the plastic domain at lower stress levels. It can be concluded that the quality of the specimens is influenced by their surrounding conditions. For instance, the geometry and orientation of the components affect the cross-sectional area to be printed per layer, resulting in variations in layer processing time.

The specimen geometry, when close to the final part shape, further impedes heat dissipation, exacerbating thermal retention. It is therefore recommended to use cylindrical specimens with a constant cross-sectional diameter to improve heat dissipation and prevent thermal accumulation, thereby avoiding degradation of mechanical properties. Under the current approach, acceptable parts may be rejected due to non-representative specimens. In this context, a revision of ASTM E8/E8M is suggested, as the standard does not explicitly state that specimens produced by additive manufacturing should not exceed the build height, although it allows for alternative specimen dimensions.

In this study, only three setup temperatures were investigated: 170, 95, and 80 °C. It was observed that the specimens produced exhibited superior properties at a build platform temperature of 80 °C, followed by those manufactured at 95 °C. Higher temperatures were found to induce an aging process in the parts during fabrication, thereby reducing their mechanical properties, such as tensile strength and hardness. The dissipation of heat generated by laser utilization during additive manufacturing occurs primarily through the part itself. Since it is not possible to cool the build platform, but only to heat it, a setup temperature around 80 °C, or potentially even lower values, depending on the build volume, may be employed. This would allow for improved heat dissipation as well as a reduction in the heating time of the plate, consequently decreasing the overall setup time. Although temperatures below 80 °C could be explored, it should be noted that the lower the temperature, the higher the risk of defects arising from lack of fusion.

To prevent the deterioration of mechanical properties during the build process, it would be advisable to collaborate with the machine supplier’s development team to enable adjustments to laser power according to the area of each layer being constructed. This approach would help

avoid overheating of the layers or allow the establishment of a minimum layer time, thereby facilitating improved heat dissipation and more efficient cooling during the build, ultimately enhancing the mechanical properties of the components.

To assess the quality of the parts, in a quick and easy way, hardness tests could be performed alongside density determination using the liquid displacement method, since the rapidity at which results are obtained with these techniques is considerably higher than with tensile testing. Tensile specimen should be done, in order to perform tensile tests, but this require specimen machining, which increases considerably the time to have results, and the use of a tensile testing machine, which is a bulky and costly piece of equipment, thereby creating dependence on specialized laboratories or academic institutions. After initial validation with hardness and density tests, the parts could be sent to the customer, and when possible, tensile tests would be performed.

The specimens for hardness testing should be parallelepiped-shaped and match the build height, as this would greatly facilitate the experimental work, reduce the time spent, and minimize resource consumption. Even if these specimens exceeded 100 mm in dimension, they could subsequently be cut and analysed. Depending on the geometry and size of the parts, such tests could even be conducted directly on the manufactured components, with the costumer approval, since they are non-destructive.

In summary, it can be concluded that recycled powders exhibit properties comparable to those of virgin powders. However, chemical composition analysis should be performed using a more accurate technique for low atomic number elements, such as oxygen. Regarding the builds themselves, among the studied temperatures, 80 °C and 95 °C produced specimens with the best results, while the meander scanning strategy demonstrated excellent performance even at 170 °C. Specimens should be manufactured with dimensions equal to or smaller than the build height, according to the heights specified by ASTM E8/E8M, since specimens exceeding the build height experience a sharp reduction in layer time, resulting in inefficient heat dissipation. Heat accumulation during the build process leads to microstructural alterations, which reduce the mechanical properties of the specimens, making them unrepresentative of the build. Post-build heat treatment resulted in a decrease in both UTS and hardness, as well as homogenization of values across different builds. After the heat treatment, nearly all samples comply with the UTS SR1 values specified by ASTM F3318.

References

ASTM International E8/E8M. (2022). *Standard Test Methods for Tension Testing of Metallic Materials*. ASTM International.

ASTM International F2971. (2013). *Standard Practice for Reporting Data for Test Specimens Prepared by Additive Manufacturing*.

ASTM International F3318-18. (2018). *Additive Manufacturing - Finished Part Properties - Specification for AlSi10Mg with Powder Bed Fusion - Laser Beam*.

Bogdanova, M., Chernyshikhin, S., Zakirov, A., Zotov, B., Fedorenko, L., Belousov, S., Perepelkina, A., Korneev, B., Lyange, M., Pelevin, I., Iskandarova, I., Dzidziguri, E., Potapkin, B., & Gromov, A. (2024). Mesoscale Simulation of Laser Powder Bed Fusion with an Increased Layer Thickness for AlSi10Mg Alloy. *Journal of Manufacturing and Materials Processing*, *8*(1). https://doi.org/10.3390/jmmp8010007

Bosio, F., Phutela, C., Ghisi, N., Alhammadi, A., & Aboulkhair, N. T. (2023). Tuning the microstructure and mechanical properties of AlSi10Mg alloy via in-situ heat-treatments in laser powder bed fusion. *Materials Science and Engineering: A*, *879*. https://doi.org/10.1016/j.msea.2023.145268

De Seabra, A. V. (1995). *Metalurgia Geral - Metalografia: Vol. III* (2ª). Laboratório Nacional de Engenharia Civil.

EN 6018. (2017). Aerospace series - Test methods for metallic materials - Determination of density acording displacement. In *European Commite for Standardization*.

Froes, F., & Boyer, R. (Eds.). (2019). *Additive Manufacturing for the Aerospace Industry*. Elsevier. https://doi.org/10.1016/C2017-0-00712-7

Ghio, E., & Cerri, E. (2022). Additive Manufacturing of AlSi10Mg and Ti6Al4V Lightweight Alloys via Laser Powder Bed Fusion: A Review of Heat Treatments Effects. In *Materials* (Vol. 15, Issue 6). MDPI. https://doi.org/10.3390/ma15062047

Gunenthiram, V., Peyre, P., Schneider, M., Dal, M., Coste, F., & Fabbro, R. (2017). Analysis of laser–melt pool–powder bed interaction during the selective laser melting of a stainless steel. *Journal of Laser Applications*, *29*(2). https://doi.org/10.2351/1.4983259

Huck-Jones, D., & Langley, C. (2017). Beyond particle size: Exploring the influence of particle shape on metal powder performance. *Metal Additive Manufacturing* , *3*(4), 99–103.

Hwang, W. J., Bang, G. B., & Choa, S. H. (2023). Effect of a Stress Relief Heat Treatment of AlSi7Mg and AlSi10Mg Alloys on Mechanical and Electrical Properties According to Silicon Precipitation. *Metals and Materials International*, *29*(5), 1311–1322. https://doi.org/10.1007/s12540-022-01304-7

Ifeanyi Iwediba, I., Ali Murtaza, H., Yankin, A., Perveen, A., & Talamona, D. (2023). Comparative analysis and characterization of used and unused Alsi10mg powders. *Materials Today:*

Proceedings. https://doi.org/10.1016/j.matpr.2023.07.070

Ion, J. C. . (2005). *Laser processing of engineering materials : principles, procedure and industrial application*. Boston : Elsevier/Butterworth-Heinemann.

ISO/ASTM 52901:2016. (2016). *Standard Guide for Additive Manufacturing - General Principles - Requirements for Purchased AM Parts*.

ISO/ASTM 52904:2019. (2019). *Additive Manufacturing - Process Characteristics and Performance: Practise foe Metal Powder Bed Fusion Process to Meet Critical Applications*.

ISO/ASTM 52907:2019. (2019). *Additive manufacturing - Feedstock materials - Methods to characterize metalic powders*.

ISO/ASTM 52921:2013. (2013). *Standard Terminology for Additive Manufacturing - Coordinate Systems and Test Methodologies*.

ISO/ASTM 52930. (2021). *Additive manufacturing - Qualification principles - Installation, operation and performance (IQ/OQ/PQ) of PBF-LB equipment*. ISO/ASTM52930.

Kumar, M. S., Yang, C.-H., Ross, N. S., Romanovski, V., & Salah, B. (2026). Data-driven machine learning optimization of DLMS parameters for sustainable AlSi10Mg powder reuse and superior part performance. *Powder Technology*, *468*, 121628. https://doi.org/10.1016/j.powtec.2025.121628

Ladewig, A., Schlick, G., Fisser, M., Schulze, V., & Glatzel, U. (2016). Influence of the shielding gas flow on the removal of process by-products in the selective laser melting process. *Additive Manufacturing*, *10*, 1–9. https://doi.org/10.1016/j.addma.2016.01.004

Limbasiya, N., Jain, A., Soni, H., Wankhede, V., Krolczyk, G., & Sahlot, P. (2022). A comprehensive review on the effect of process parameters and post-process treatments on microstructure and mechanical properties of selective laser melting of AlSi10Mg. In *Journal of Materials Research and Technology* (Vol. 21, pp. 1141–1176). Elsevier Editora Ltda. https://doi.org/10.1016/j.jmrt.2022.09.092

Martucci, A., Aversa, A., & Lombardi, M. (2023). Ongoing Challenges of Laser-Based Powder Bed Fusion Processing of Al Alloys and Potential Solutions from the Literature—A Review. In *Materials* (Vol. 16, Issue 3). MDPI. https://doi.org/10.3390/ma16031084

Merino, J., Ruvalcaba, B., Varela, J., Arrieta, E., Murr, L. E., Wicker, R. B., Benedict, M., & Medina, F. (2021). Multiple, comparative heat treatment and aging schedules for controlling the microstructures and mechanical properties of laser powder bed fusion fabricated AlSi10Mg alloy. *Journal of Materials Research and Technology*, *13*, 669–685. https://doi.org/10.1016/j.jmrt.2021.04.062

Mertens, A., Delahaye, J., Dedry, O., Vertruyen, B., Tchuindjang, J. T., & Habraken, A. M. (2020). Microstructure and properties of SLM AlSi10Mg: Understanding the influence of the local thermal history. *Procedia Manufacturing*, *47*, 1089–1095. https://doi.org/10.1016/j.promfg.2020.04.121

Měsíček, J., Čegan, T., Ma, Q. P., Halama, R., Skotnicová, K., Hajnyš, J., Juřica, J., Krpec, P., & Pagáč, M. (2022). Effect of artificial aging on the strength, hardness, and residual stress of SLM AlSi10Mg parts prepared from the recycled powder. *Materials Science and*

Engineering: A, *855*. https://doi.org/10.1016/j.msea.2022.143900

Müller, S., & Westkämper, E. (2018). Modelling of Production Processes: A Theoretical Approach to Additive Manufacturing. *Procedia CIRP*, *72*, 1524–1529. https://doi.org/10.1016/j.procir.2018.03.010

O'Brien, M. J. (2019). Development and qualification of additively manufactured parts for space. *Optical Engineering*, *58*(01), 1. https://doi.org/10.1117/1.oe.58.1.010801

Pavlinskii, G. V., & Vladimirova, L. I. (2009). Determination of low atomic number elements by X-ray fluorescence fundamental parameter method. *Journal of Analytical Chemistry*, *64*(3), 253–258. https://doi.org/10.1134/S1061934809030083

Phutela, C., Bosio, F., Li, P., & Aboulkhair, N. T. (2023). Correlating the microstructure and hardness of AlSi10Mg powder with additively-manufactured parts upon in-situ heat-treatments in laser beam powder bed fusion. *Additive Manufacturing Letters*, *7*. https://doi.org/10.1016/j.addlet.2023.100168

Renishaw. (2024). *RenAM 500 series additive manufacturing system - User guide*. www.renishaw.com

Santecchia, E., Spigarelli, S., & Cabibbo, M. (2020). Material reuse in laser powder bed fusion: Side effects of the laser—metal powder interaction. In *Metals* (Vol. 10, Issue 3). MDPI AG. https://doi.org/10.3390/met10030341

Saracyakupoglu, T. (2019). The Qualification of the Additively Manufactured Parts in the Aviation Industry. *American Journal of Aerospace Engineering*, *6*(1), 1. https://doi.org/10.11648/j.ajae.20190601.11

Saunders, M. (2019). *X marks the spot - find the ideal process parameters for your metal AM parts*. www.renishaw.com

Sefat, Farshid., Farzi, G. Ali., & Mozafari, Masoud. (2023). *Principles of biomaterials encapsulation. Volume 1*. Woodhead Publishing.

Smith, W. F. ., Hashemi, Javad., & Presuel-Moreno, Francisco. (2019). *Foundations of materials science and engineering*. McGraw-Hill Education.

Song, L., Zhao, L., Ding, L., Zhu, Y., Liang, S., Huang, M., Simar, A., & Li, Z. (2024). How heterogeneous microstruture determines mechanical behavior of laser powder bed fusion AlSi10Mg. *Materials Science & Engineering A*.

Srivastava, M., Rathee, S., Maheshwari, S., & Kundra, T. K. (2020). *Additive Manufacturing; Fundamentals and Advancements* (1st Edition). CRC Press. https://doi.org/https://doi.org/10.1201/9781351049382

Syrlybayev, D., Perveen, A., & Talamona, D. (2024). Controlling mechanical properties and energy absorption in AlSi10Mg lattice structures through solution and aging heat treatments. *Materials Science and Engineering: A*, *889*. https://doi.org/10.1016/j.msea.2023.145843

Tang, M., Pistorius, P. C., & Beuth, J. L. (2017). Prediction of lack-of-fusion porosity for powder bed fusion. *Additive Manufacturing*, *14*, 39–48. https://doi.org/10.1016/j.addma.2016.12.001

Wang, F., Chen, B., Chen, Z., Tong, M., Ren, S., Wang, Z., Xia, P., Zhu, J., & Li, R. (2025). Effect of Direct Ageing and Stress Relief Annealing on the Microstructure and Properties of Laser

Selective Melting AlSi10Mg. *Metals and Materials International*. https://doi.org/10.1007/s12540-025-01940-9

Wischeropp, T. M., Emmelmann, C., Brandt, M., & Pateras, A. (2019). Measurement of actual powder layer height and packing density in a single layer in selective laser melting. In *Additive Manufacturing* (Vol. 28, pp. 176–183). Elsevier B.V. https://doi.org/10.1016/j.addma.2019.04.019

Yadroitsev, I., Gusarov, A., Yadroitsava, I., & Smurov, I. (2010). Single track formation in selective laser melting of metal powders. *Journal of Materials Processing Technology*, *210*(12), 1624–1631. https://doi.org/10.1016/j.jmatprotec.2010.05.010

Yi, F., Zhou, Q., Wang, C., Yan, Z., & Liu, B. (2021). Effect of powder reuse on powder characteristics and properties of Inconel 718 parts produced by selective laser melting. *Journal of Materials Research and Technology*, *13*, 524–533. https://doi.org/10.1016/j.jmrt.2021.04.091

Yusuf, S. M., Cutler, S., & Gao, N. (2019). Review: The impact of metal additive manufacturing on the aerospace industry. In *Metals* (Vol. 9, Issue 12). MDPI AG. https://doi.org/10.3390/met9121286

Appendices

Appendix 1 – Purchase Order

The purchase order should have the information that fallows on Table A1.1, A1.2 and A1.3.

Table A1.1 – Part ordering information.

Information	Relevant subclause of ISO/ASTM 52901	Content
Reference identification of the document – ISO/ASTM 52901	4.2 (e)	ISO/ASTM 52901
Customer organization and contact information	4.2 (a)	Customer organization: Contact for Ordering: Contact for Payment: Contact for Delivery:
Customer part order identification	4.2 (f)	Requisition Number: Requisition Date:
Designation or description of the part(s) desired	4.2 (g)	Part Number: Revision Index:
Quantity of parts desired	4.2 (h)	Quantity of parts desired:
Required delivery date (if single order)	4.2 (i)	Required delivery date:
Required delivery quantity. frequency. and time duration of the order if multiple orders (if ongoing or multiple orders)	4.2 (j)	Quantity: Frequency: Time duration of the order:
Required marking or tagging of the parts	4.2 (k)	Labels: Serial number: Lot number: Feedstock type: Part provider's reference: Inspection identifier: Traceability reference:
Part packaging requirements for delivery to the customer	4.2 (l)	Part packaging requirements for delivery to the customer:
Customer shipping address	4.2 (m)	Customer shipping address:

Table A1.2 – Definition of the part to be manufactured.

Information	Relevant subclause of ISO/ASTM 52901	Content
Engineering drawing reference	4.3.2 (a)	Number: Index: Version:
Digital file reference	4.3.2 (b)	Name: Format: Version:
Geometry description	4.3.2 (c)	By an engineering drawing that fully defines the part: ☐ By a digital file containing 3D model: ☐
Tolerances	4.3.3	Note: See ISO 2768-1 and ISO 2768-2
Surface texture	4.3.4	Standard: Maximum roughness:
Build orientation of the part	4.3.5	Manufacturing process: Post processing steps: Build orientation: See ISO/ASTM 52921
Feedstock for the part to be manufactured	4.3.6	Chemical composition: Frequency: Time duration of the order:
Repair methods	4.3.7	The authorized repair methods and corresponding repair conditions shall be specified if needed and shall be approved by customer. Repair methods: Repair conditions:
Acceptance imperfection(s) or non-conformance	4.3.8	Cracks: Defects: Discontinuities: Foreign material: Inclusions: Acceptable imperfections: Acceptable deviations: Discoloration: Porosity:
Process control information	4.3.9	Requirements for manufacturing process repeatability: Requirements for documenting process control information during manufacturing:

Table A1.3 – Part characteristics. functionality and performance.

Characteristic	Relevant subclause of ISO/ASTM 52901	Content: Reference to standard to be used. frequency and number of tests – requirements to be fulfilled
Dimensional accuracy	4.4.1 and 4.4.2	
Defects	4.4.1 and 4.4.2	
Mechanical properties	4.4.1 and 4.4.2	
Residual stress	4.4.1 and 4.4.2	
Chemical composition	4.4.1 and 4.4.2	
Functionality	4.4.3	
Inspection	4.4.4	
Post-processing	4.4.5	
Other requirements	4.4.6	

Table A1.4 – Acceptance.

Type of acceptance	**Qualification part:** ❑ **First production part:** ❑ **Reference part:** ❑

Appendix 2 – Powder Sampling from Hopper

In order to collect powder from hopper two different ways were used. The first one is very

- place a spatula and an open sample vial inside the chamber with both openings facing upwards (vial and lid),

- purge the chamber with argon,

- lower the build platform about 90 mm from the chamber,

- in an inert environment, place the sample vial in one of the back corners of the build platform,

- dose a quantity of powder into the chamber,

- drag the powder into the sample vial with the spatula,

- repeat the last two steps until full fill the vial,

- close the sample vial.

- place the spatula and the sample vial in such a way that it does not jam during printing. Near the door before the sieve is a good place.

Appendix 3 – Methods used for particle size analysis

Table A3.1 – Methods used for particle size analysis according to ISO/ASTM 52907:2019.

Method	Typical range	Expression of results	Advantages	Limitations
Laser diffraction (ISO 13320)	0.1 mm to 3 mm	Cumulative volume percentages on a plot, with calculated values D_X at which X % of the total volumes is below this value	Ease of use. Large sample sizes. High accuracy and repeatability.	Measurements shall be made on isolated particles (not touching). Liquid suspension can be necessary. Assumes spherical particles when calculating volumes.
Light scattering (ISO 22412, ASTM B822)	1 nm to 0.1 mm			
Image analysis (static: ISO 13322-1)	≥ 5 mm	Either the number or volume of particles in the size intervale	Accounts for non-spherical particles. Capable of reporting shape factors.	Measurements shall be made on isolated particles (not touching). Liquid suspension can be used. Result accuracy depends on number of pixels. Set up procedures to be determined by the operator to chieve optimum results for that specific powder.
Image analysis (dynamic: ISO 13322-2)	≥ 5 mm	Either the number or volume of particles in the size intervale and shape distribution	Accounts for non-spherical particles. Capable of reporting shape factors. Large amount of particles can be measured in each sample, which provides a large dataset for statistical analysis.	Measurements shall be made on isolated particles (not touching). Liquid suspension can be necessary. Result accuracy depends on number of pixels. Set up procedures to be determined by the operator to chieve optimum results for that specific powder.
Sieving (ISO 2591-1, ISO 4497, ASTM B214)	≥ 45 mm	The amounts of particles present in specified particle size intervals, expressed as s percentage of the total particles.	Equipment required is cheaper overall than equipment required for other particle size distribution testing methods.	Appropriate sieves sizes required. Results obtained assume near spherical particles that pass through the sieve openings when the particle diameter is smaller than the size openings. This does not take into account long particles or particles with agglomerations. Carefully controlled cleaning of sieves between test required. Results obtained are discrete intervales. Not suitable for particles sized wholly or mostly under 45 mm.